13 July 2026

Fundamentals of Electrochemical Energy Storage: Theory and Practice

Mohsen Sotoudeh[1,2], Axel Groß[1,3]

1. Electrochemical Energy Storage
2. Karlsruhe Institute of Technology (KIT
3. Institute of Theoretical Chemistry, Ulm University

Abstract

The rechargeable alkali-ion battery has emerged as a transformative technology, revolutionizing portable energy storage in a wide range of applications, from small electronic devices to large electric vehicles. In this review, we combine modern theoretical and computational methods with an examination of electrochemical properties for lithium and post lithium-ion batteries. From fundamental thermodynamics and kinetics to computational techniques for materials design, we examine frameworks for deriving relationships for key battery properties such as voltage and capacity. We also explore the complexities of ion migration processes, including hopping mechanisms between lattice sites, and extend our focus to the broader field of electrochemical properties, including conductivity, redox potentials and interfacial properties. Finally, we outline perspectives on the outstanding challenges and promising opportunities in the theory and computation of rechargeable battery materials, paving the way for future advances in energy storage technology.

Fundamentals of Electrochemical Energy Storage: Theory and Practice

Mohsen Sotoudeh[*,†,‡] and Axel Groß[*,¶,†]

†*Helmholtz Institute Ulm (HIU), Electrochemical Energy Storage, 89081 Ulm, Germany*

‡*Karlsruhe Institute of Technology (KIT), P.O. Box 3640, D-76021 Karlsruhe, Germany*

¶*Institute of Theoretical Chemistry, Ulm University, 89081 Ulm, Germany*

E-mail: mohsen.sotoudeh@kit.edu; axel.gross@uni-ulm.de

Abstract

The rechargeable alkali-ion battery has emerged as a transformative technology, revolutionizing portable energy storage in a wide range of applications, from small electronic devices to large electric vehicles. In this review, we combine modern theoretical and computational methods with an examination of electrochemical properties for lithium and post lithium-ion batteries. From fundamental thermodynamics and kinetics to computational techniques for materials design, we examine frameworks for deriving relationships for key battery properties such as voltage and capacity. We also explore the complexities of ion migration processes, including hopping mechanisms between lattice sites, and extend our focus to the broader field of electrochemical properties, including conductivity, redox potentials and interfacial properties. Finally, we outline perspectives on the outstanding challenges and promising opportunities in the theory and computation of rechargeable battery materials, paving the way for future advances in energy storage technology.

Contents

1 Introduction

The global trend to reduce carbon emissions has spurred significant interest in battery materials research, particularly as a key technology for electrifying transport and storing solar and wind energy. At the same time, lithium-ion batteries have become widely used and are driving the development of portable electronics.[1,2] However, expanding the use of electrochemical energy storage for larger scale applications such as electric vehicles and grid storage depends on meeting stringent performance, safety, energy density and cost requirements that current technology may not fully meet.[3,4]

Research efforts have focused on two main avenues:[5] refining existing lithium-ion technology (advanced Li-ion) and exploring radical changes to its core components (post-Li-ion).[6] The latter includes research into alternative mobile ions (e.g. Na-ions[7–9] or Mg-ions[10–15]), the use of metallic anodes and the implementation of solid electrolytes to develop solid-state batteries.[16,17] These post-Li-ion strategies are not mutually exclusive and can be combined to tailor battery characteristics for specific applications. For example, combining a solid-state battery with a metal anode shows promise for improving safety, cycle life, energy and power densities.[16,18]

Inorganic solid-state materials, which enable fast ion conduction, are key to the design of post-Li-ion batteries.[19] The aim of this review is to explore the current understanding of the material properties of inorganic solid electrode and electrolytes relevant to their integration into rechargeable batteries. In particular, we focus on recent advances to highlight current trends, directions and challenges in the field.

2 History of the battery

Over the past two centuries, scientific efforts have been devoted to understanding and manipulating chemical processes to improve energy storage capabilities, a milestone characterized by the pioneering work of Alessandro Volta on the battery in 1799.[20] In the first century

following Volta's breakthrough, the focus was primarily on exploring the redox chemistry of transition metals in aqueous electrolytic environments, exemplified by the use of lead-acid batteries or Ni-metal hybrid configurations in various transportation systems. This era was characterized by constraints imposed by the stability window of water, which limited operating voltages to within 1.23 V. However, the advent of lithium-ion battery technology heralded a transformative change, facilitated by the adoption of non-aqueous electrolytes.[21] Freed from the limitations of the water stability window, lithium-ion batteries have enabled significant improvements in both power and energy density within our energy storage infrastructure as shown in Figure 1.

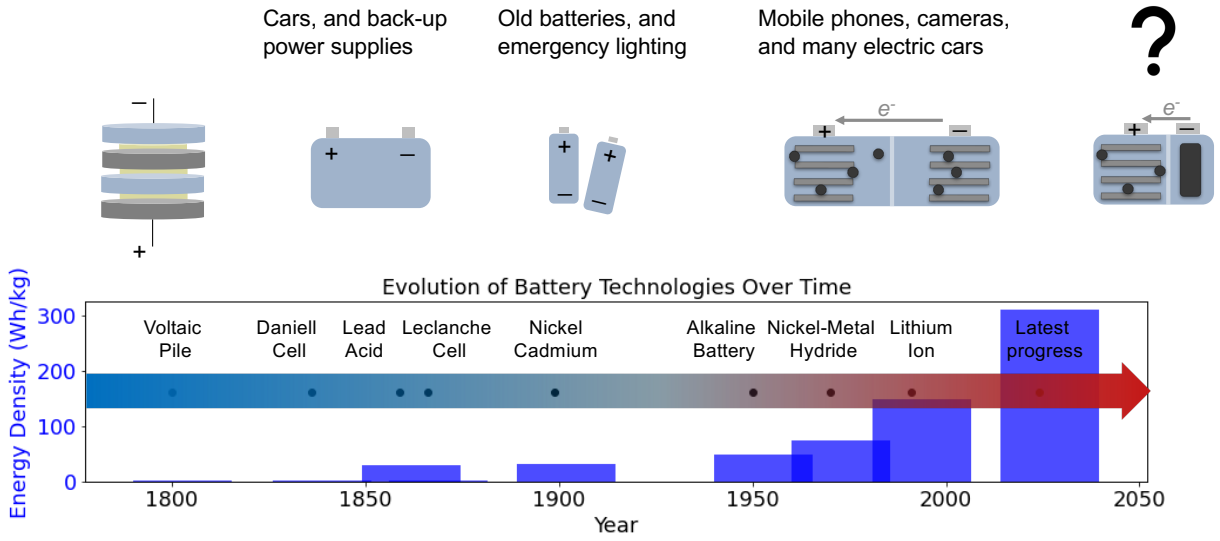

Figure 1: Milestones in the evolution of battery technology.

Figure 1 shows other key milestones in the evolution of batteries. Many of the battery technologies highlighted here have had a long life in the marketplace and have endured over the years or are still in use today. These include the lead-acid starter battery, the primary zinc-carbon battery (e.g. cylindrical batteries used in flashlights), the alkaline manganese round cell (used in cameras and remote controls) and the nickel-metal hydride battery (used in razors and telephones).

Lithium-based technology, on the other hand, is a relatively recent development. Mass production of primary lithium batteries began in the mid-1960s. Throughout the 1970s,

luminaries in the field, including Michel Armand, Robert Huggins and Stanley Whittingham, worked on intercalation electrodes using lithium ions. Whittingham[22] has proposed to combine lithium with titanium sulphide (TiS_2) for the intercalation electrode epitomized pioneering research, where intercalation refers to the incorporation of ions or small molecules into layer or channel configurations.

In 1990, efforts to introduce rechargeable lithium metal batteries were hampered by safety concerns.[23] A year later, however, Sony introduced the lithium-ion cell using the intercalation principle. The nomenclature "lithium-ion" was deliberately chosen to emphasize the absence of metallic lithium in the anode. This breakthrough technology was based on John Goodenough[24,25] cathode patent and Sony expertise in carbon electrodes. The lithium-ion cell used lithium cobalt oxide ($LiCoO_2$)[26] for the cathode and amorphous carbon for the anode, primarily targeting consumer electronics applications such as video cameras. Structurally, the cell adopted a cylindrical design encased in robust materials.

2.1 Rechargeable Battery Operation

The presence of complex oxide phases[27] with high ionic conductivity, coupled with the ability to change the oxidation state of a *d*-metal ion, has facilitated the creation of materials suitable for use as cathodes in rechargeable batteries. Examples include $LiCoO_2$,[26] which has a layered structure of interconnected CoO_6 octahedra separated by Li^+ ions (Figure 2), and various lithium-manganese spinels such as $LiMn_2O_4$.[28] In these compounds, the battery is charged by extracting mobile Li^+ ions from the complex metal oxide as follows:

$$LiCoO_2 \rightarrow CoO_2 + Li^+ + e^- \tag{1}$$

The battery is discharged by an inverse electrochemical process. Lithium cobalt oxide, commonly used in commercial lithium-ion batteries, has several essential characteristics for such applications. The specific energy of $LiCoO_2$ (140 Wh kg^{-1})[29] is optimized by incor-

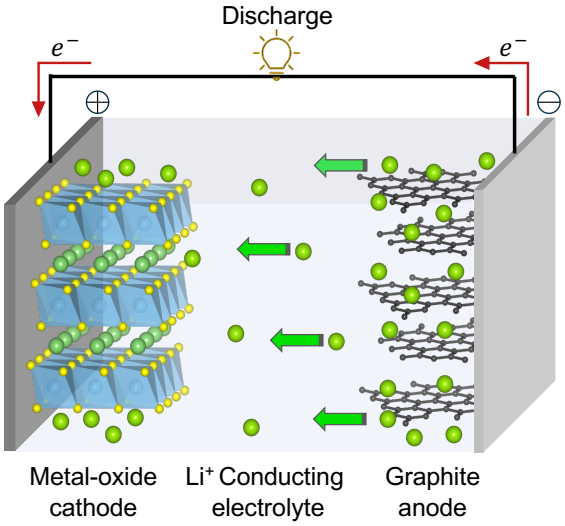

Figure 2: Schematic representation of a Li-ion rocking chair battery cell. The main components are a graphite anode, a metal oxide cathode and a Li-ion conducting electrolyte. During the discharge process, Li ions are de-intercalated at the anode and intercalated at the cathode, while the electrolyte is responsible for moving the ions between the electrodes.

porating light elements such as Li and Co. The $3d$ metals are typically favored in these applications due to their low density and variable oxidation states. The small ionic radius of lithium ions and the layered structure of $LiCoO_2$ facilitate high mobility and reversible electrochemical charging and discharging, allowing lithium ions to be extracted without significant structural disruption. The high lithium content of $LiCoO_2$ enables high capacity, with around 500 discharge/charge cycles achievable. In addition, the battery delivers current at a constant and high potential difference (between 3.5 and 4 V), due in part to the high oxidation states of cobalt (Co^{3+} and Co^{4+}).

Due to the chemical instability with a tendency to lose oxygen and toxicity associated with cobalt,[29,30] research is ongoing to discover oxide materials superior to $LiCoO_2$. These new materials must exhibit comparable levels of reversibility to lithium cobaltate. Considerable effort is being devoted to exploring doped variants of $LiCoO_2$ and $LiMn_2O_4$ spinels.[28,31] There is also considerable interest in $LiFePO_4$[32,33] due to its favorable cathodic properties and the use of inexpensive and non-toxic iron.

In a rechargeable lithium-ion battery, the counter electrode to the cathode can simply be

lithium metal, which facilitates the overall cell reaction by undergoing the $\mathrm{Li}(s) \rightarrow \mathrm{Li}^+ + e^-$ process. Lithium ions then move to the cathode via an electrolyte, typically an anhydrous lithium salt[24] such as $LiPF_4$ or $LiC(SO_2CF_3)_3$ dissolved in a polymer such as poly (propene carbonate). However, the use of lithium metal poses several challenges due to its reactivity and the volume fluctuations that occur within the cell.[23] Consequently, an alternative anode material often used in rechargeable batteries is graphitic carbon (see Figure 2), which is capable of electrochemically intercalating significant amounts of lithium to form LiC_6. During discharge, lithium transfers between the carbon layers at the anode and intercalates into the metal oxide at the cathode (and vice versa during charging):

$$\mathrm{Li}_y\mathrm{C}_6 + \mathrm{Li}_{1-x}\mathrm{CoO}_2 \rightleftarrows \mathrm{C}_6 + \mathrm{Li}_{1-x+y}\mathrm{CoO}_2 \tag{2}$$

This chemical reaction is expressed in terms of the neutral form of the charge carrier, such as Li. In the absence of an open external circuit, there is no driving force for this reaction. The maximum voltage of a battery, V, is determined by its open circuit voltage, V_{OC}, according to the following equation:

$$V_{\mathrm{OC}} = -\frac{\Delta G}{zF} \tag{3}$$

where ΔG is the free energy change of the combined anode/cathode reaction, F represents the Faraday constant and z corresponds to the charge transferred during the chemical reaction. In order to ascertain the open circuit voltage (V_{OC}), it is necessary to consider the specific chemical reactions that occur at the anode and cathode. Alternatively, the open circuit voltage can be determined by the difference in lithium chemical potentials,[1,34] between cathode ($\mu_{\mathrm{Li}}^{cathode}$) and anode ($\mu_{\mathrm{Li}}^{anode}$) as follows:

$$V_{\mathrm{OC}} = -\frac{\mu_{\mathrm{Li}}^{cathode} - \mu_{\mathrm{Li}}^{anode}}{zF}. \tag{4}$$

The operational voltage of a battery cell is typically lower than the open circuit voltage, V_{OC}, due to internal resistance and other losses. During charging, this process is reversed by applying an external voltage, which must exceed to compensate for losses. In rechargeable batteries, the chemical reactions occurring during both charging and discharging must be reversible. While battery operation may appear straightforward, numerous challenges are associated with it. In addition to ion shuffling during charge and discharge, the insertion and de-insertion of ions into electrodes often result in volume changes. This poses a significant issue for silicon-based anodes, which exhibit high specific capacity but undergo considerable volume changes, up to a factor of three during cycling, resulting in mechanical stress.[35]

2.2 Cathode Chemistry

The enhancement of cell voltage and the development of cathodes necessitate the stabilization of higher oxidation states within a lower energy band in the cathode and the stabilization of lower oxidation states within a higher energy band in the anode. The primary challenge is to access the lower energy band of a metal ion with higher oxidation states within a material in order to increase the cell voltage.

From 1950 to 1980, the characteristics of transition metal oxides[27] that the S-3p band sits at a higher energy level than the O-2p band enabled researchers to devise oxide cathodes (see Figure 3). Consequently, the ability to access lower energy bands containing higher oxidation states, such as Co^{3+}/Co^{4+}, and thus attain elevated cell voltages, is constrained by the summit of the S-3p band. Attempts to reduce the redox energy of the cathode by exploiting higher oxidation states within a sulfide would result in the oxidation of S^{2-} ions to molecular disulfide ions (S_2^{2-}).[36] Conversely, within an oxide, the redox energy of the cathode can be substantially curtailed by accessing lower energy bands, such as Co^{3+}/Co^{4+}, thereby enabling the elevation of the cell voltage. The voltage is approximately 4 V, as the O-2p band is at a lower energy level than the S-3p band.

The basic concept outlined here led to the identification of three distinct categories of

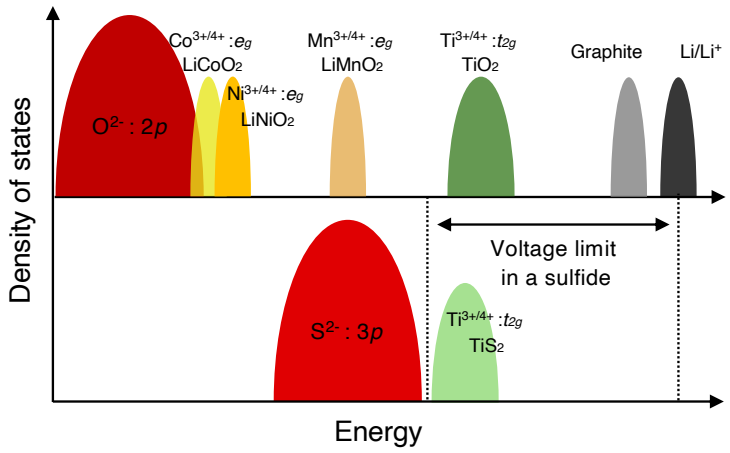

Figure 3: Positions of the redox energies relative to the top of the anion: p bands. The top of the S^{2-}:3p band lying at a higher energy restricts the cell voltage to $< 2.5\,V$ with a sulfide cathode. In contrast, the top of the O^{2-}:2p band lying at a lower energy enables access to lower-lying energy bands with higher oxidation states and increases the cell voltage substantially to $\approx 4\,V$.

oxide cathodes in the 1980s. This effort who focused on layered oxide, spinel oxide, and polyanion cathodes[36] (see Figure 4). In particular, these classes remain the primary practical options for lithium-ion batteries, with the layered and polyanionic variants also serving as fundamental elements for sodium-ion battery cathodes.[37]

It should be noted that the suitability of cathode materials for different applications is dependent upon their unique properties. Nevertheless, the selection of a specific cathode material is not solely determined by electrochemical metrics (see Table 1). In addition, other factors such as cost, durability and safety characteristics (illustrated in Figure 5) also play an important role in the decision-making process.

Layered oxides offer a distinct advantage in applications where high energy density is a priority. Their high operating voltages and consequent energy densities are due to the redox properties of nickel, cobalt and manganese ions. However, these metals are notably scarce in the lithosphere, leading to their high market prices, in contrast to the widespread abundance and low cost of iron. As a result, lithium iron phosphate (LFP) emerges as the most economical choice for producing of cathode material, although its advantage is

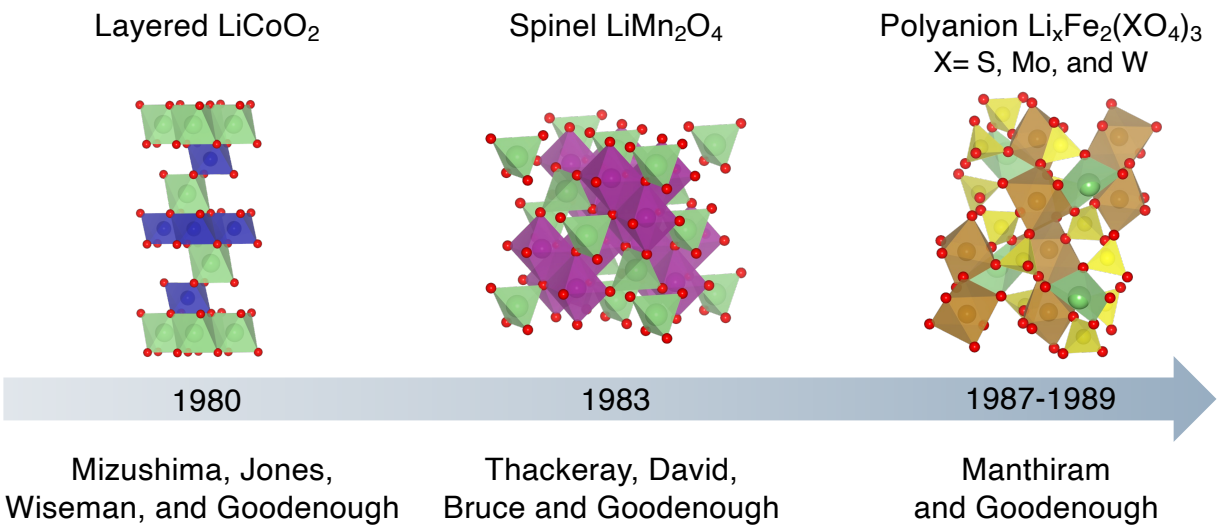

Figure 4: The discovery of three distinct categories of oxide cathodes. Firstly, layered $LiCoO_2$, featuring octahedral-site lithium ions, exhibited a notable enhancement in cell voltage compared to TiS_2, rising from below 2.5 V to approximately 4 V. Secondly, spinel $LiMn_2O_4$, housing tetrahedral-site lithium ions, demonstrated an increase in cell voltage from 3 V, characteristic of octahedral-site lithium ions with the Mn^{3+}/Mn^{4+} couple, to around 4 V, accompanied by a reduction in costs. Lastly, polyanion oxide $Li_xFe_2(SO_4)_3$ presented an alternative approach to augment cell voltage via an inductive effect, elevating it from below 2.5 V in a basic oxide like Fe_2O_3 to 3.6 V, while concurrently decreasing costs and enhancing thermal stability and safety.

diminished due to its lower energy density compared to nickel cobalt manganese (NCM) and lithium nickel cobalt aluminium oxide (NCA).

Despite their advantageous properties, oxides raise safety concerns as they can induce oxygen evolution,[29] potentially leading to cell ignition or even explosion. LFP, however, does not present this risk due to its inherent properties and does not exhibit thermal effects up to 300°C, unlike other oxide-based cathode materials which exhibit significant exothermic effects.[39] In addition, LFP and lithium iron manganese phosphate (LFMP) are environmentally friendly and non-toxic, unlike heavy metal oxide compounds.

It should be noted that LFP is the sole cathode material that permits rapid charging and discharging, despite only allowing lithium diffusion in one direction. In contrast, other materials offer two-dimensional or even three-dimensional lithium diffusion pathways. Although it has not yet achieved the high energy and power densities characteristic of oxide cathode

Table 1: Comparison of Capacity, Working Voltage, and Energy Density of Cathode Materials. Data are taken from Ref.[38]

Material	Capacity (Ah kg^{-1})	Working voltage (V)	Energy density (Wh kg^{-1})
NCA ($LiCo_{0.85}Al_{0.15})_2$	200	3.7	740
LCO ($LiCoO_2$)	160	3.9	624
NCM ($LiNi_{0.33}Mn_{0.33}Co_{0.33}O_2$)	160	3.7	592
LMO ($LiMn_2O_4$)	100	4.1	410
LFP ($LiFePO_4$)	160	3.4	544
LFMP ($LiFe_{0.15}Mn_{0.85}PO_4$)	150	4.0/3.4	590

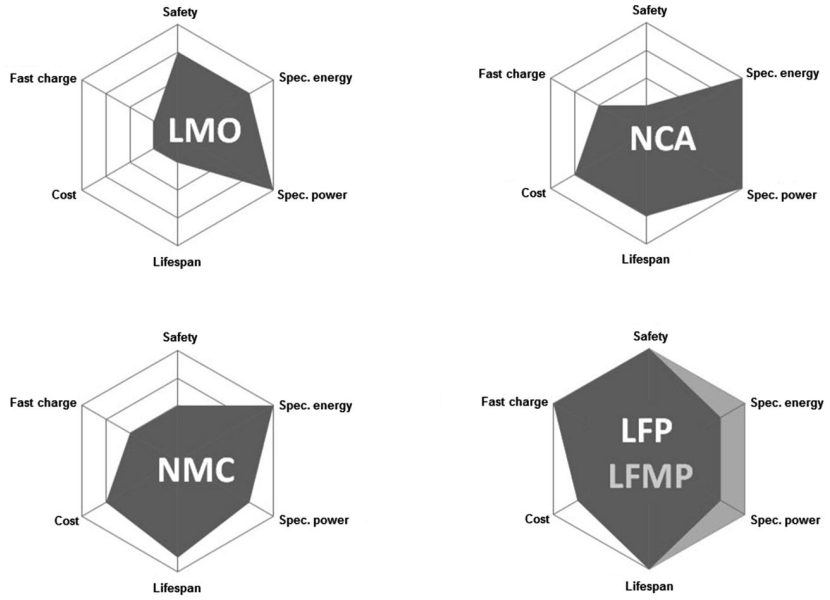

Figure 5: Key performance parameters of four current battery chemistries (LFP, LMO, NCA, and NMC). The inside and outside represent a low and high value, respectively. Reprinted from Ref.,[38] with permission from Springer Nature.

materials, incorporating manganese into LFP (LFMP)[40,41] can increase these values by up to 20%. The development of phosphate-based cathode materials, while promising, is still in its infancy. By substituting iron for manganese, cobalt or nickel, higher operating voltages and energy densities can be achieved, making phosphate-based compounds very promising for future high-voltage applications.

2.3 Anode Chemistry

Metallic lithium foil as the anode or negative electrode has a remarkably high specific capacity of 3860 mAh/g[42] and exhibits a highly negative potential, resulting in a significantly higher cell voltage. However, the effectiveness of cycling is reduced because lithium is continuously dissolved during discharging and redeposited during charging. As a result, an excess of lithium is required, often two to three times the normal amount. In addition, lithium deposition can take the form of foam or dendrites,[23,43] the latter potentially penetrating the separator. These dendrites pose a risk of localized short circuits leading to complete self-discharge of the cell or, in extreme cases, triggering an internal thermal chain reaction leading to fire or explosion.

In order to create cells that are both safe and efficient in cycling, lithium metal is replaced with a material known as lithium intercalation. Typically, this intercalation process is reversible, as in carbon, and does not involve any loss, thus preventing lithium plating. Graphite anodes[44] are standard in the lithium-ion cells commonly used in consumer electronics (such as smartphones). However, there is growing interest in using amorphous carbons, such as hard and soft carbons,[45,46] in newer applications that offer higher power and energy density, as well as improved safety features. These carbons often exhibit superior current capabilities and are more stable when combined with innovative electrolytes and cathode materials.

Lithium titanate and titanium oxide[47] are emerging as potential alternatives for anode active materials, offering improved cycling stability and meeting stringent safety and performance requirements. However, their specific capacity is significantly low and they have a high potential versus lithium. Figure 6 illustrates the specific capacity and potential of the main anode materials. Despite significant research and development efforts, metal-based systems have not yet reached mass production, indicating the need for further research. Although the addition of carbon, such as C/Si or C/Sn composites,[48] shows promise for improvement, cycling stability remains a concern.

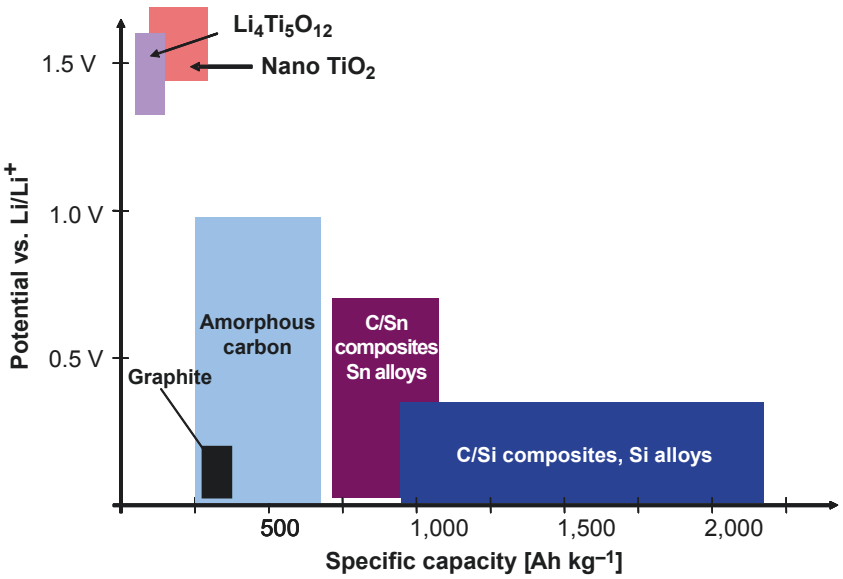

Figure 6: Specific capacity and potential vs. Li/Li^+ of the anode materials. Reprinted from Ref.,[38] with permission from Springer Nature.

2.4 Electrolyte Components

The ideal electrolyte must meet several criteria, including high conductivity over a wide temperature range (–40°C to +80°C), stability over many cycles, and compatibility with electrodes and other materials.[49] Safety, environmental impact and cost effectiveness are also important considerations.[50] Meeting these requirements presents a number of challenges that require innovative solutions. It is important to note that a single perfect electrolyte has not yet been developed.

The electrolyte for lithium-ion batteries consists of three classes of materials: conducting salt, organic aprotic solvents (or, in some cases, polymers) and additives. The interaction between these elements largely determines the physical, chemical and electrochemical properties of the electrolyte and plays a crucial role in achieving the stated objectives.

A suitable lithium salt should exhibit maximum solubility and complete dissociation in aprotic solvents, in order to ensure efficient lithium-ion mobility. Moreover, the lithium salt must demonstrate high electrochemical stability against oxidation, in addition to robust chemical stability towards the solvent and compatibility with all components of the cell, in

particular the current collector and separator. From a chemical perspective, these requirements favor complex anions where the negative charge is widely distributed, resulting in a reduced charge density. The reduced density of the anion reduces the attraction between the anion and the lithium cation, thereby promoting free cation movement and ensuring high mobility. The presence of electron-withdrawing groups, such as fluorine, highly fluorinated organic radicals, carboxyl or sulphonyl groups, serves to minimize the interactions between the anion and the lithium cation.

Lithium hexafluorophosphate ($LiPF_6$) holds a unique position among potential compounds, particularly in the field of lithium-ion batteries. With a conductivity of 8 to 12 mS/cm at room temperature and a concentration of 1 mol/l, $LiPF_6$, when mixed with organic carbonates which are blends of ethylene carbonate (EC) and dimethyl carbonate (DMC), propylene carbonate (PC), diethyl carbonate (DEC), and/or ethyl methyl carbonate (EMC), facilitates the production of highly conductive electrolytes.[49,51] These electrolytes exhibit electrochemical stability up to almost 5 V compared to the standard lithium electrode.[52] In particular, $LiPF_6$ stands out among conductive salts for its ability to effectively prevent corrosion of aluminium current collectors within the positive electrode, particularly at potentials above 3 V against the standard lithium.

A high-voltage electrolyte is of significant importance for the development of lithium-ion batteries.[53,54] Organic fluoro-compounds have emerged as promising electrolyte solvents for high voltage scenarios due to the heightened oxidation potentials conferred by fluorinated molecules, which result from the electron-withdrawing effect of fluorine atoms.[53] Zhang et al.[55] investigated the stability of different fluorinated electrolytes under high voltage conditions, demonstrating that E5 electrolytes (1.2 M $LiPF_6$ in F-AEC/F-EMC/F-EPE, 2/6/2 ratio) exhibited superior electrochemical stability compared to EC/EMC-based electrolytes. Moreover, the substitution of EMC with F-EMC and EC with F-AEC led to a notable enhancement in the voltage limits of the electrolyte. Table 2 presents a comprehensive overview of the physicochemical properties of these common solvents.

Table 2: Physico-chemical characteristics of selected battery solvents. The values are taken from Ref.[38]

Characteristics	Carbonate					Ester		Ether	
	EC	PC	DMC	DEC	EMC	EA	MP	DME	THF
Melting point (°C)	36	-48	2-4	-43	-55	-83	-84	-58	-108
Boiling point (°C)	247-249	242	90	125-129	108	77	102	84	65-66
Viscosity (25°C) (cP)	1.9 (40°C)	2.53	0.59	0.75	0.65	0.45	0.60	0.46	0.46
Permittivity (25°C)	90 (40°C)	65	3.1	2.8	3.0	6.0	5.6	7.2	7.4
Flash point (°C)	160	135	15	33	23	-4	11	0	-17

In recent years, there has been a surge in the introduction of new formulations to replace lithium hexafluorophosphate due to its susceptibility to hydrolysis. Among these, compounds based on sulfonylimides such as lithium bis(trifluoromethylsulfonyl)imide (LiTFSI) and lithium bis(fluorosulfonyl)imide (LiFSI) have emerged as promising alternatives. These novel conductive salts offer conductivity levels comparable to $LiPF_6$, thus meeting the demands of high load current requirements. LiFSI has a remarkable conductivity of 12 mS/cm[56] (0.85 M, 25 °C, EC/DMC), exceeding that of $LiPF_6$ and making it particularly suitable for high current applications. While LiTFSI has a slightly lower conductivity than $LiPF_6$, its dissociation in commonly used carbonates plays a crucial role. High dissociation levels ensure sufficient conductivity and battery performance even at low temperatures.

The solvent should effectively dissolve lithium salts at high concentrations, which requires a high dielectric constant to ensure ion solvation. At the same time, it should have a low viscosity to facilitate unhindered ion transport, which is particularly important at low temperatures and in high-voltage scenarios where rapid migration of lithium ions is essential. The solvent must remain inert to all other components within the battery system under various operating conditions, particularly the charged electrode materials and the current collector, due to the increasing charging potentials of lithium-ion batteries. A wide liquid range is desirable, so the solvent should have a low melting point and a high boiling point. Safety, toxicity, flash point and economic factors are also important considerations.

In lithium-ion batteries, the negative electrode typically uses highly reducing materials

such as lithiated carbon or graphite, while the positive electrode uses highly oxidizing materials such as lithium metal oxides or metal phosphates. Therefore, solvents with active acidic protons, which could lead to hydrogen evolution, are unsuitable. Water is also excluded for the same reason.

Among the organic solvents suitable for Li-ion batteries, ethers and esters, including organic carbonates, are recognized. While alternatives such as nitrile, functionalized silanes, sulfones and sulfites are being discussed in academic contexts, ethers have lost favour due to limited electrochemical stability with the introduction of 4 V transition metal oxides as positive electrode materials. Esters, particularly organic diesters of carboxylic acids (carbonates), are now commonly used. Mixtures of cyclic carbonates (e.g. ethylene carbonate [EC] and to some extent propylene carbonate [PC]) are preferred because of their high dipole moment and moderate viscosity. Open-chain carbonates (dimethyl carbonate [DMC], diethyl carbonate [DEC] and ethyl methyl carbonate [EMC]) with moderate dipole moments and low viscosity are also used.

In some cases, open-chain esters such as ethyl acetate (EA) or methyl butyrate (MB) are added as co-solvents to further enhance the performance of the electrolyte, particularly at low temperatures.

In addition to facilitating the movement of lithium ions, electrolytes must perform additional functions to enhance both safety and performance. The evolving demands of emerging applications such as electric vehicles and stationary energy storage require higher standards. Essential to meeting these standards are additives that play a key role in optimizing the Solid Electrolyte Interface (SEI), the interface between the negative electrode and the electrolyte, which has a profound effect on the longevity and efficiency of lithium-ion cells.

A prominent example of such additives is vinylene carbonate,[57] which is widely used in commercial lithium-ion cells because it significantly improves cycling stability. Its effectiveness is particularly evident during initial charge and discharge cycles, where it forms a thin polymer-like film on the electrode surface just above the intercalation of lithium ions into

the carbon, typically at potentials of around 1.0 – 1.1 V vs. Li/Li^+.[58] Several alternatives to vinylene carbonate exist, including functionalized organic carbonates such as fluoroethylene carbonate (FEC) and vinyl ethylene carbonate (VEC), and SEI-forming conductive salts such as lithium bis(oxalato)borate (LiBOB). However, these developments are still at an early stage.

The use of LiBOB as an additive is an example of deliberate modification of the SEI structure.[59] Different solvents lead to different SEI structures due to different reactivities on the electrode surface. In ethylene carbonate (EC)-based electrolytes, the SEI consists mainly of EC degradation products due to their higher reactivity and denser structure. Even with the incorporation of LiBOB, the interface remains predominantly EC. In contrast, EC-free solutions result in SEI layers containing both components, with film formation controllable by the forming protocol.[38]

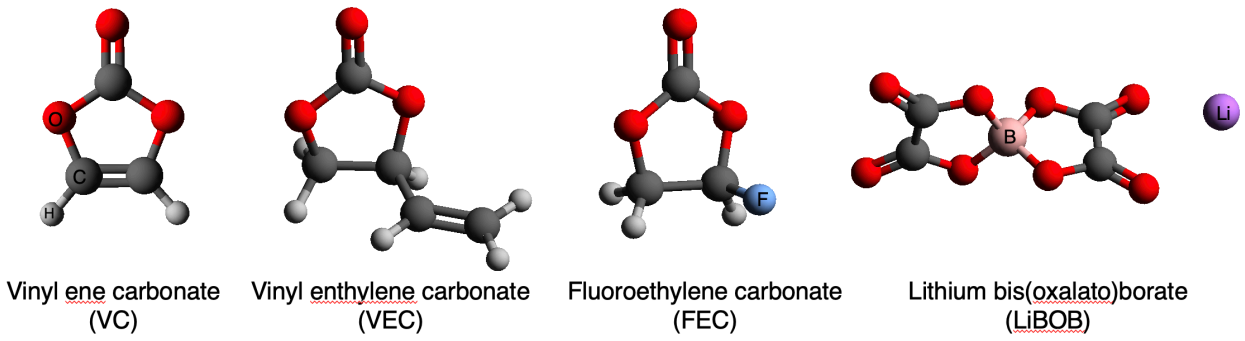

Figure 7: Selection of additives that form SEI films.

3 Post-Li-ion batteries

Post-Li-ion batteries offer several distinct advantages over traditional lithium-ion counterparts, making them compelling candidates for next-generation energy storage solutions. The primary advantage of post-Li-ion batteries lies in utilization of a wider range of mobile cations, including the substitution of Li for other alkali metals, Na and K, as well as

multivalent-ion batteries (MVIBs) based on Mg, Ca, Al, or Zn[60] (Figure 8). The enhanced compatibility with diverse materials offers the potential for the utilization of abundant and cost-effective elements in battery manufacturing, thereby reducing the reliance on scarce lithium resources and potentially reducing the overall cost of batteries[61] as illustrated in Figure 8. In addition, alternative cationic chemistries can exhibit unique electrochemical properties, offering opportunities to enhance battery performance and tailor properties to specific applications.

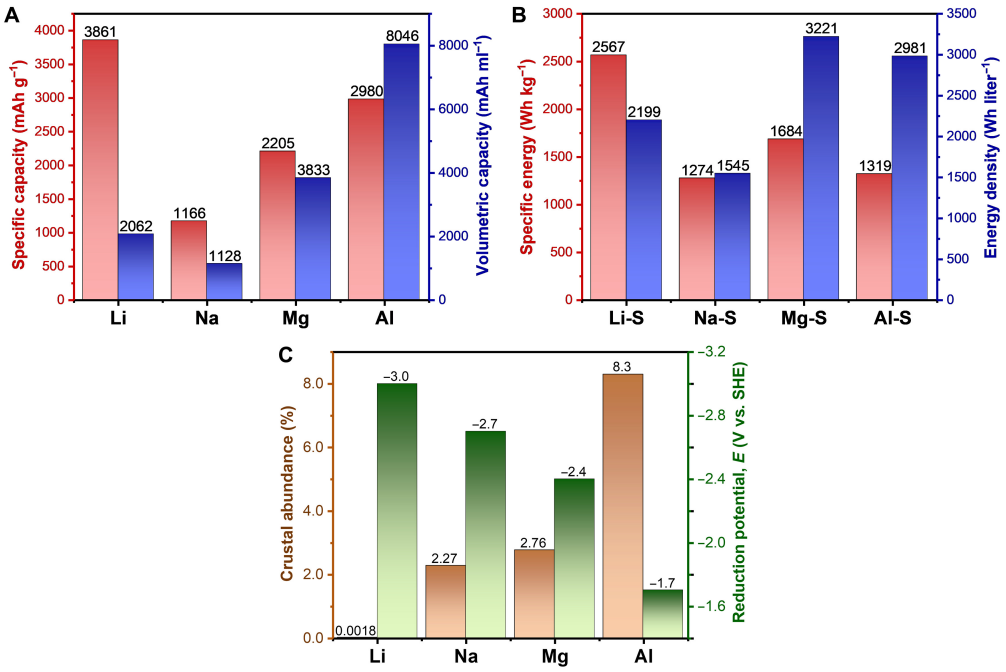

Figure 8: Summary of energy storage parameters for different battery chemistries. (A) Specific and volumetric capacities of lithium, sodium, magnesium and aluminium metal anodes. (B) Outlines theoretical specific energies and energy densities of metal sulphur batteries. The energy values tabulated are derived from the conversion of elemental sulphur, S_8, to discharge products: Li_2S, Na_2S, MgS and Al_2S_3 respectively. (C) Elemental abundances in the Earth's crust and reduction potentials of metal anodes compared to the standard hydrogen electrode (SHE). Reprinted from Ref.,[62] published under a CC BY-NC license.

Furthermore, post-Li-ion battery chemistries have the potential to achieve higher energy densities compared to conventional lithium-ion systems[63,64] as shown in Figure 8. By exploring alternative electrode materials with higher specific capacities and utilizing novel electrolyte formulations, post-Li-ion batteries can store more energy per unit volume or

weight.[65] This increased energy density enables the development of battery systems with longer driving ranges for electric vehicles and higher energy storage capacities for stationary applications, ultimately contributing to greater efficiency and sustainability in energy usage.

Post-lithium-ion batteries could also improve stability and longevity over multiple charge-discharge cycles by addressing degradation mechanisms such as lithium dendrite formation.[66] One promising avenue is the stabilization of next-generation electrodes, particularly metallic anodes such as sodium (Na) and magnesium (Mg), which are known for their high capacities and operating voltages. In addition, high-voltage cathodes can increase the energy output per ion transfer,[16] but can trigger oxidation of traditional liquid electrolytes. Although the integration of metallic anodes and high-voltage cathodes with solid electrolytes has shown promise in solid-state microbatteries,[67] their adaptation to large-scale systems requires further verification.

By adopting alternative chemistries, such as solid-state electrolytes and non-flammable electrode materials, post-Li-ion batteries can mitigate the safety concerns and offer increased resistance to thermal abuse.[68] Inorganic solid electrolytes could enable battery operation over a wide temperature range (e.g. –50 to 200°C or higher) where conventional liquid electrolytes would freeze, boil or decompose. The inherently slower reactivity of solids compared to liquids also suggests longer device lifetimes for solid-state batteries. Solid-state microbatteries[67] have demonstrated this by operating for over 10,000 cycles, but the scalability of this property remains unproven.

It is important to note that the gas generation previously attributed solely to liquid electrolyte-based cells is also observable in solid-state batteries.[69] It is therefore anticipated that this phenomenon of gas evolution will occur across a wide range of relevant cathode materials in post-Li-ion cells, which may lead to safety and ageing concerns. It is of significant importance to conduct a thorough investigation into the phenomenon of polarization at the solid electrolyte/electrode interfaces.

3.1 Challenges facing post-Li-ion batteries

Given the promising advantages of post-Li-ion batteries, significant efforts have been directed towards their further development. In this context, four main challenges related to electrodes and electrolytes have been identified for post-Li-ion battery devices.

While the transition from traditional Li-ion to post-Li-ion chemistries promises improved energy density and safety, it also introduces complexities in ion transport. The main challenges for Mg-ion batteries and Al-ion batteries lie in identifying electrolytes with improved electrochemical oxidation stability and in creating cathode materials with high charge-storage capacity under high potentials.[70] Multiple factors contribute to this challenge, including limited compatibility with electrodes in terms of both chemical and electrochemical properties, which is evident in the form of a narrow electrochemical stability window. Additionally, the absence of reversible metal plating and stripping, instability concerning current collectors, sluggish ion mobility (e.g., Mg ions), resulting in low Coulombic efficiency (CE) further complicate the development of versatile electrolytes. While solid electrolytes offer improved stability and safety over liquid counterparts, they often have limited ionic conductivity, which impedes ion mobility.

The second issue is related to the strong interaction between charge carriers and solvent molecules, which results in desolvation at the electrolyte-cathode interface. This ultimately impedes the insertion of ions into the cathode.[71,72] The composition and structure of interfaces between electrolytes and electrode materials often differ significantly from those of the bulk materials. The formation of degradation products that interfere with ionic conductivity or electron transport has hampered the performance of post-Li-ion devices. A variety of experimental and computational methods are required to study the formation and behavior of such interfaces. A deeper understanding of the nature of interfaces will facilitate the rational selection of materials for the next generation of post-Li-ion cells.

The utilization of metal anodes in liquid-based cells presents a significant challenge due to the uneven deposition of sodium or magnesium in filamentous formations, commonly

referred to as dendrites.[73,74] It was previously assumed that solid electrolytes would prevent dendrite-induced failures due to their mechanical stiffness. However, recent findings have demonstrated that metallic lithium can indeed infiltrate solid materials, as evidenced by reference.[75] A significant disadvantage of solid-state systems is their dependence on contact between solid particles for ionic diffusion. These point contacts are particularly susceptible to stresses that arise in the electrode materials during electrochemical cycling, which can lead to cracking,[76] interface delamination and other problems.[77] It is therefore of great importance to develop effective strategies to address the issue of physical contact in order to facilitate the development of post-Li-ion batteries.

Another challenge lies in the fact that battery designs in academia tend to prioritize proof-of-concept testing, with the result that considerations such as cost and the mass/volume of inactive components within the battery are often overlooked.[70] However, these factors are critical for commercial viability. The lack of technological maturity in these alternative battery systems makes it challenging to predict which type will emerge as a commercial product. Furthermore, none of the current post-Li-ion battery technologies can rival Li-ion batteries in terms of energy density, a distinction that is unlikely to change in the future.

The resolution of these challenges depends on a comprehensive understanding of the fundamental properties of solid electrode and electrolyte materials. In this review, we examine the current state of knowledge on inorganic materials, focusing on multiscale ion transport, electrochemical stability, mechanics and their dependence on available processing methods.

4 Multivalent batteries

Although the concept of a rechargeable magnesium battery was first proposed in 1990,[78] the first functional demonstration of a prototype magnesium full cell battery was achieved in 2000 by Aurbach et al. ,[11] utilized a magnesium metal anode, an electrolyte comprising magnesium organo-halo-aluminate salts dissolved in tetrahydrofuran (THF), and a Chevrel cathode

composed of $Mg_xMo_6S_8$ (where $0 < x_{Mg} \leq 2$). These advancements in electrolyte and cathode design have enabled the researchers to attain favorable kinetics and cycle longevity, with the battery operating at approximately 1.1 V compared to magnesium metal and surpassing 2000 cycles. The battery exhibited an approximate specific capacity of 70 mAh/g (with a theoretical capacity of 128.8 mAh/g),[11] corresponding to an energy content of around 77 Wh/kg and 400 Wh/l, based on Chevrel's density of approximately 5.2 g/cm^3.[79] This pivotal achievement served to reinforce the credibility of magnesium battery technology and established a clear benchmark for the assessment of future cathode materials for magnesium batteries. Figure 9 presents a visual illustration of several promising candidate cathodes.

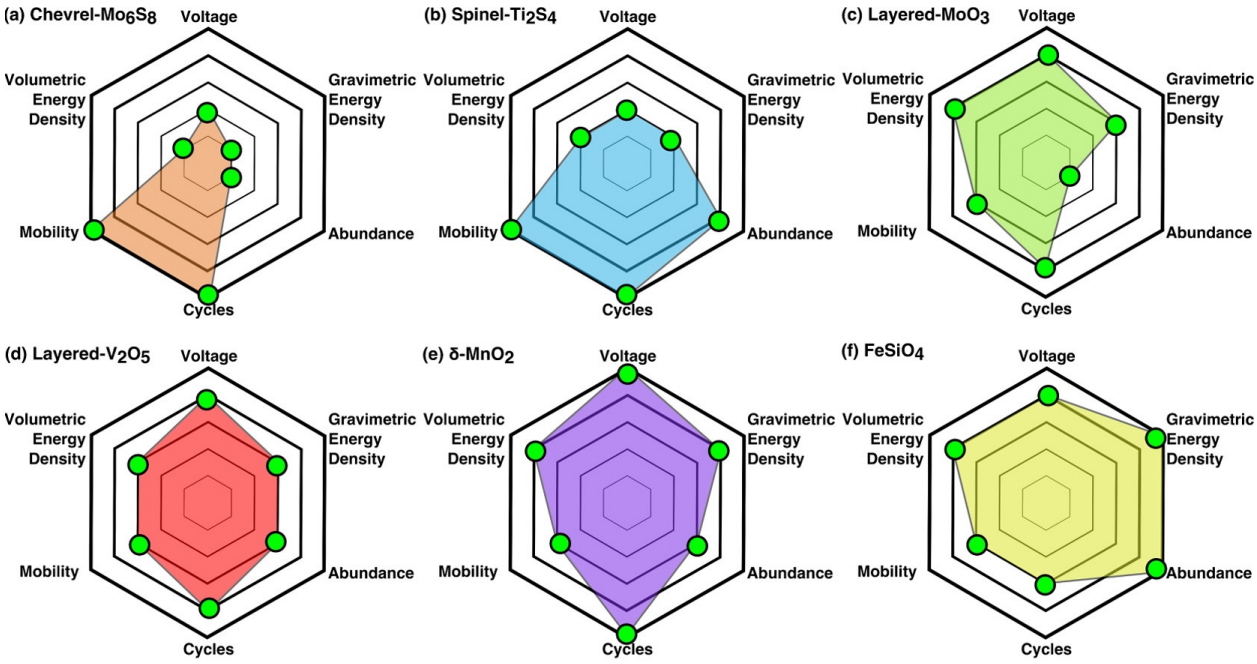

Figure 9: The parameters for assessing the potential of cathode materials, encompassing intercalation voltage (V), practical gravimetric (Wh/kg) and volumetric (Wh/l) energy densities, barrier for bulk Mg mobility (eV), cycling behavior (number of cycles), and abundance of the transition metal utilized in the cathode, measured in parts per million (ppm) by mass in the Earth's crust. These parameters are synthesized across various frameworks within the chemical spaces of chalcogenides (e.g., Chevrel and Ti_2S_4), oxides (e.g., MoO_3, V_2O_5, and MnO_2), and polyanions (e.g., $FeSiO_4$). Reprinted from Ref. ,[80] copyright (2017) American Chemical Society.

4.1 Chalcogenides

Chalcogenides have emerged as promising candidates for magnesium (Mg) cathodes, exhibiting superior electrochemical performance. A pivotal advancement by Aurbach and colleagues[11] demonstrated the reversible intercalation of magnesium in Chevrel-Mo_6S_8 and other cluster compounds, achieving cycle lives comparable to those of present-day lithium-ion compounds, albeit at lower energy densities. Consequently, a number of chalcogenide hosts, including sulfides (e.g., TiS_2,[81,82] MoS_2[83]) and selenides (e.g., $TiSe_2$,[84] WSe_2[85]), have been investigated, with the results being somewhat inconclusive. Despite the anticipated sluggish migration of Mg in layered TiS_2,[86] recent demonstrations of high-capacity reversible Mg intercalation in spinel Ti_2S_4[81] at moderate rates indicate its potential. It is noteworthy that Ti_2S_4 cycled at approximately 1.2 V exhibits a capacity of approximately 190 mAh/g, which represents a significant enhancement in energy density compared to the Chevrel phase. The performance of sulfide spinels aligns with recent *ab initio* calculations,[87] which underscore the significance of sulfur cathode chemistries in facilitating highly reversible Mg intercalation. Although MoS_2[83,88] garners attention due to its two-dimensional nature, its low capacity and higher cost present challenges in surpassing other sulfide cathodes such as Mo_6S_8 and Ti_2S_4. Alternatives such as $TiSe_2$[84] and WSe_2[85] present the potential for enhanced Mg mobility at comparable voltages and gravimetric capacities. Nevertheless, the reliability of Mg intercalation experiments in selenides necessitates the rigorous characterization of discharged products, which emphasizes the need for the establishment of baseline experimental data in these systems.

4.2 Oxides

Transition metal oxide hosts have attracted attention as potential cathode materials for multivalent batteries due to their high theoretical voltages and capacities.[89,90] Nevertheless, the widespread adoption of these materials is hindered by a number of challenges. The majority of oxide hosts are constrained by a number of limitations, including poor ion mobility

within their bulk structure,[89,91] the potential occurrence of oxide conversion reactions in the cathode,[92] contributions of pseudocapacitance from nanosized frameworks,[93] and electrolyte incompatibility with high-voltage cathodes.[94] These factors collectively make it challenging to observe and validate reversible multivalent intercalation at reasonable rates.

Nevertheless, certain types of oxide hosts, particularly layered-oxide hosts such as MoO_3,[95] $Mo_{2.48}VO_{9.93}$,[96] V_2O_5,[97] and δ-MnO_2,[98] have attracted considerable experimental and theoretical attention as cathodes for multivalent batteries. The reversible intercalation at comparable voltages has been demonstrated in these hosts with varying degrees of success. While oxide spinel hosts often exhibit high barriers for multivalent migration,[89] recent theoretical estimations suggesting high ionic mobility in high-pressure postspinel phases[99] offer promise for the development of a new class of cathode materials. Furthermore, in layered oxides the modification of the nanoconfining interlayer distance by synthetic pillaring approaches has been proposed as a promising strategy.[100,101]

A strategy of water (or solvent) cointercalation[102,103] has been proposed as a means of enhancing ion mobility in oxide hosts, with the potential to enable higher voltages and better mobilities. Although water cointercalated hosts, such as xerogel-V_2O_5[104] and certain MnO_2 polymorphs,[98] have demonstrated promising electrochemical performance, further investigation is necessary to elucidate potential side reactions, such as proton cycling, which could contribute to enhanced performance. Nevertheless, the presence of water in the electrolyte may present challenges for the practical implementation of multivalent batteries utilizing a magnesium metal anode. It may be necessary to explore the use of alternative solvents that can reversibly cointercalate and are compatible with the magnesium anode, should it be demonstrated that solvent cointercalation is an effective mechanism for enhancing multivalent mobility in oxide hosts.

The fundamental question of whether solvent cointercalation improves mobility in the bulk and the exact mechanism behind such improvement remains unanswered. If solvent cointercalation does enhance ion mobility in the bulk, preintercalating the solvent in lay-

ered cathode materials may be a viable strategy. Despite these challenges, oxides remain an exciting class of potential multivalent cathode materials due to their high potential energy density. The battery community has learned from nearly two decades of research on multivalent electrochemistry that divalent ions exhibit a diverse range of behaviors, including different diffusivities and distinct electrochemical properties. While multivalent ion mobility is typically lower than that of monovalent intercalants such as Li^+,[89] careful matching of structure and intercalant holds promise for achieving reasonable mobility for ions such as Mg^{2+}, Ca^{2+}, or Zn^{2+}, as demonstrated by high-rate reversible Zn^{2+} insertion in V_2O_5.[101,105]

4.3 Polyanions

The performance of cathodes based on polyanions exhibits a diverse range of characteristics, comparable to those observed in oxides. For example, the potential of magnesium (Mg) intercalation within iron silicate ($FeSiO_4$)[106] has been demonstrated to be promising, yet the occurrence of potential side reactions in other polyanion frameworks, such as manganese (Mn)[107] and cobalt (Co)[108] silicates, has clouded the assessment of whether reversible intercalation processes can indeed occur. Moreover, while NASICON frameworks exhibit notable mobility with lithium (Li) and sodium (Na) ions, they appear less favorable for magnesium (Mg) intercalation due to high theoretical migration barriers and observed sluggish Mg movement in experiments.[109–111] While theoretical investigations on specific fluoro-polyanions[112] demonstrate potential, corresponding experimental studies[113] on structures like $FePO_4F$ encounter challenges such as poor Coulombic efficiencies and low capacities.

Although borates[114] exhibit intriguing diffusion mechanisms with potential cross-framework applications, their attained capacities remain suboptimal even at elevated temperatures. Prussian blue analogues[115–119] are distinguished by their capacity to intercalate a range of multivalent species, including relatively unexplored ions such as strontium (Sr) and barium (Ba), yet their energy densities are limited.[120] Although their immediate utility in batteries is limited, the stability and reversibility of Prussian blue structures render them valuable for

research purposes as counter and reference electrodes.

Certain polyanion materials, notably silicates such as $FeSiO_4$ and fluoro-polyanions such as $FeSO_4F$, appear to have potential for use in multivalent battery applications, subject to comprehensive experimental and theoretical validation of Mg intercalation and any associated constraints. While multivalent batteries offer considerable potential beyond conventional lithium-ion counterparts, practical challenges hinder their technological advancement. A significant knowledge gap exists regarding the intricate reactions among electrolytes, electrodes, and current collectors. These reactions often lead to uncharacterized corrosion phenomena that obscure the behavior of multivalent ions during intercalation. In contrast to more established lithium and sodium chemistries, the characterization of multivalent cathodes presents a significant challenge, particularly in distinguishing reversible intercalation from other electrochemical processes.

4.4 Remarks

In order to validate multivalent insertion at different charge states, it is essential to employ rigorous characterization techniques such as X-ray diffraction (XRD), X-ray absorption near-edge structure (XANES), and transmission electron microscopy (TEM). Theoretical data can be employed to complement experimental findings and identify any discrepancies. *Ab initio* theory has been demonstrated to be effective in predicting electrochemical voltages within a narrow window.

The observed variability in electrochemical data across multivalent cathode studies highlights the influence of electrolyte composition. This necessitates the use of specialized setups for testing high-voltage cathodes due to the narrow stability window of most multivalent electrolytes. It is imperative that standardized protocols, analogous to those employed in the lithium and sodium battery communities, be established to ensure consistent evaluation of multivalent cathode materials and electrolyte stability. Furthermore, the impact of electrolyte quantity on cell performance must be given greater consideration, as

laboratory-scale experiments frequently employ excess electrolyte, in contrast to commercial cells, which are designed to achieve optimal energy density, safety, and cost-effectiveness. It is of paramount importance to validate multivalent electrolyte/cathode combinations under limited electrolyte conditions in order to facilitate their practical deployment.

4.5 Anode and Electrolytes

The use of metallic anodes in multivalent chemistry represents a promising avenue for enhancing volumetric energy density. This is particularly the case when materials such as magnesium (Mg) are utilized, which offer a theoretical volumetric energy density of approximately 3833 mAh/cm^3, in comparison to around 2046 mAh/cm^3 for lithium (Li) metal. The feasibility of this approach is supported by initial indications that the metallic form of common multivalent intercalation ions, such as magnesium (Mg) and calcium (Ca), exhibit more uniform deposition compared to metallic lithium (Li) during electrochemical cycling.[121,122] Conversely, the surface area of lithium metal anodes increases significantly upon cycling, resulting in heightened surface reactions with the electrolyte. The instability of the surface layer, particularly under elevated temperatures, accelerates the onset of thermal runaway, which may culminate in fire incidents.[123]

Despite their frequent use in laboratory-made Li-cell prototypes, the practical utilization of Li metal anodes in commercial batteries has been impeded by concerns over cycle life and safety. Consequently, existing Li-ion batteries employ graphite anodes with a lower volumetric energy density, approximately 800 mAh/cm^3. A number of attempts have been made to develop and commercialize full electrochemical cells with lithium metal anodes and liquid electrolytes, but these have often ended in failure.[124]

While multivalent cells hold promise for achieving high-energy densities utilizing metallic anodes, the quest for electrolytes capable of facilitating reversible multivalent metal plating/stripping at the anode and supporting reversible intercalation against high-voltage cathodes poses a substantial scientific challenge. The advancement of versatile multivalent

electrolytes is hindered by various factors, including limited chemical and electrochemical compatibility with electrodes. This manifests as a narrow electrochemical stability window, absence of reversible multivalent metal stripping and plating, susceptibility to instability against current collectors, low mobility of multivalent ions (e.g., Mg) resulting in the formation of ionic couples (with low multivalent transference number),[125] and low Coulombic Efficiency (CE) as highlighted in Figure 10.

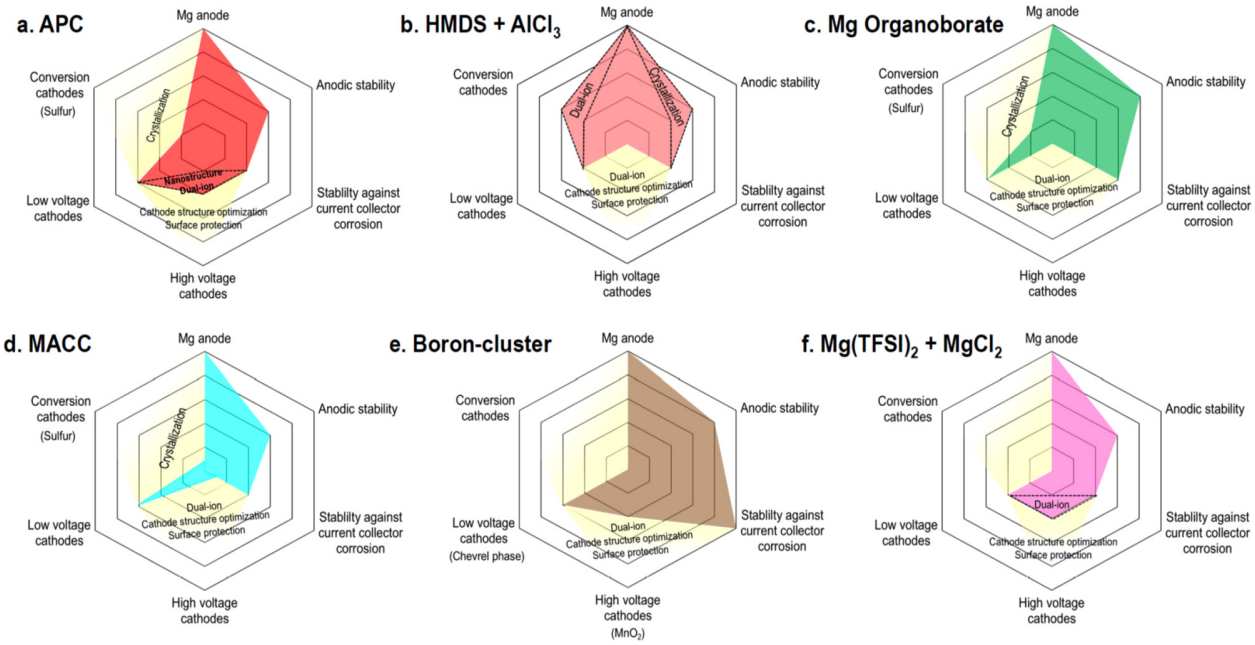

Figure 10: Radar plots illustrating the key metrics that can be used to assess the suitability of Mg electrolytes for full-cell Mg-ion batteries. The plots include: (a) All phenyl complex (APC), (b) HMDS, (c) Mg organoborate, (d) MACC, (e) Boron-cluster, and (f) $Mg(TFSI)_2$. Reprinted from Ref. ,[126] copyright (2016) American Chemical Society.

The distinctive electrochemical properties of magnesium present considerable challenges in the design of electrolytes, particularly in achieving compatibility with high-voltage cathode materials while ensuring reversible magnesium deposition at the metal anode. Conventional magnesium electrolytes, analogous to those employed in lithium-ion batteries (e.g., $LiPF_6$ in PC/DMC solutions), frequently undergo irreversible decomposition at the magnesium metal, resulting in the formation of insulating layers that impede magnesium-ion conduction.[127,128] However, recent research by Keyzer et al.[129] has demonstrated the reversible

stripping and deposition of magnesium at the metal anode using a solution composed of $Mg(PF_6)_2 \cdot (CH_3CN)_6$ in CH_3CN and CH_3CN/tetrahydrofuran (THF) mixtures. The electrolytes in question exhibit high conductivities of up to 28 mS cm^{-1} and anodic stabilities of approximately 4 V vs. magnesium on aluminium electrodes.

The ethereal solutions, which contain organic magnesium aluminium chloride salts, are also known as organo-magnesium-chloride complexes.[130] These comprise the dichloro complex (DCC)[130] and the all phenyl complex (APC).[130,131] These complexes, initially investigated by Doe[132] and collaborators, exhibit notable electrochemical properties. They subsequently extended this research to the magnesium aluminium chloride complex (MACC), derived from $AlCl_3$ and $MgCl_2$ in ethereal solvents. MACC exhibits comparable anodic stability to DCC and APC, in addition to efficient reversible magnesium deposition and stripping. Concurrently, Kim et al.[133] at Toyota R&D introduced a non-nucleophilic electrolyte, HMDSMgCl and $AlCl_3$, specifically designed for high-energy density Mg-S batteries.

Nevertheless, despite their utility in advanced Mg-battery prototypes, DCC, APC, and MACC electrolytes are susceptible to corrosion, including stainless steels and common current collectors. This limitation prompted the investigation of alternative electrolyte chemistries. For example, Shao et al.[134] demonstrated reversible magnesium deposition using a diglyme solution of $LiBH_4$ and $Mg(BH_4)_2$, although with lower anodic stability. Meanwhile, researchers[135–137] at Toyota R&D discovered halogen-free electrolytes, such as Mg boron clusters and carboranes, which exhibited reduced corrosiveness and the highest reported anodic stability windows.

Furthermore, the growing interest in multivalent chemistries has prompted investigations into electrolytes capable of reversible Ca-stripping and deposition.[122] Despite significant advancements in Mg electrolyte development over the past two decades, the range of electrolytes compatible with high-voltage Mg-cathodes remains limited (Figure 10). Typically, researchers resort to conventional Mg salts dissolved in various solvents, necessitating complex electrode setups for experiments on high-voltage cathodes. Furthermore, recent study[125]

has highlighted the influence of electrode nature on reported anodic stability, emphasizing the need for meticulous experimental design and reporting standards. Additionally, the literature on passivation mechanisms of multivalent cathodes remains sparse,[138] underscoring the necessity for systematic studies elucidating cathode-electrolyte interfacial processes.

5 Important Practical Parameters

In order to gain an understanding of the diverse applications of electrochemical energy storage systems, it is necessary to consider their distinctive characteristics. Specific energy and specific power, denoting energy and power per unit weight, respectively, are of great importance in applications such as vehicle propulsion. Conversely, energy density, which represents the stored energy per unit volume, is of critical importance for portable electronic devices such as smartphones and laptops. Despite the theoretical values being determinable through the material properties within the electrodes, the maximum theoretical values are rarely achieved in practical applications. A significant contributing factor to this discrepancy is the presence of passive components within practical battery systems that do not actively participate in the fundamental chemical processes underlying energy storage. These passive elements include the electrolyte, a separator that provides physical isolation of the electrodes, current connectors that facilitate the flow of current to and from the interior of the cell, and the container itself. Furthermore, the efficient utilization of active components in the chemical reactions is often suboptimal. It is possible to electronically isolate or shield electrode reactant materials from the electrolyte, thus preventing their participation in electrochemical reactions and rendering them inactive.

Table 3 presents approximate practical energy density and specific energy values for various rechargeable battery systems. It is important to note that these values are not definitive, as they are subject to several operational variables and may vary between manufacturers' designs. Nevertheless, the data presented does illustrate the considerable range of these

parameters that are commercially available using different technologies.

Table 3: Practical energy characteristics of common rechargeable battery systems. The values are taken from Ref.[139]

Characteristic	Pb/PbO_2	Cd/Ni	Hydride/Ni	Li-ion
Specific energy (Wh/kg)	40	60	80	135
Energy density (Wh/liter)	90	130	215	320

A further crucial aspect of the practical application of batteries is their capacity to deliver power, which is typically referred to as specific power. This indicates the power output per unit weight. This metric is significantly influenced by the intricacies of the cell design and the characteristics of its reactive components, resulting in considerable variation between different battery types. Battery characteristics are frequently presented in the form of Ragone plots, in which specific power is plotted against specific energy. This visual representation technique was devised by D.V. Ragone, who chaired a government committee responsible for a comprehensive report on the comparative properties of various battery systems. Figure 11 illustrates a plot of this nature, displaying approximate data for a range of electrical energy-storage technologies.

5.1 The Operating Voltage

In addition to energy capacity, a critical aspect of a battery system is its operating voltage during discharge, when it is providing electrical energy and power, and during the recharging process.

The open circuit or equilibrium cell voltage is primarily influenced by the thermodynamics of the chemical reaction occurring within the electrodes. This reaction drives the transport of ions through the electrolyte and the flow of electrons in the external circuit. In practice, however, the operating voltage deviates from the theoretical values due to various kinetic factors. The utility of high-voltage energy is typically superior to that of low-voltage energy due to its superior quality. This relationship is evident in basic resistance scenarios, where

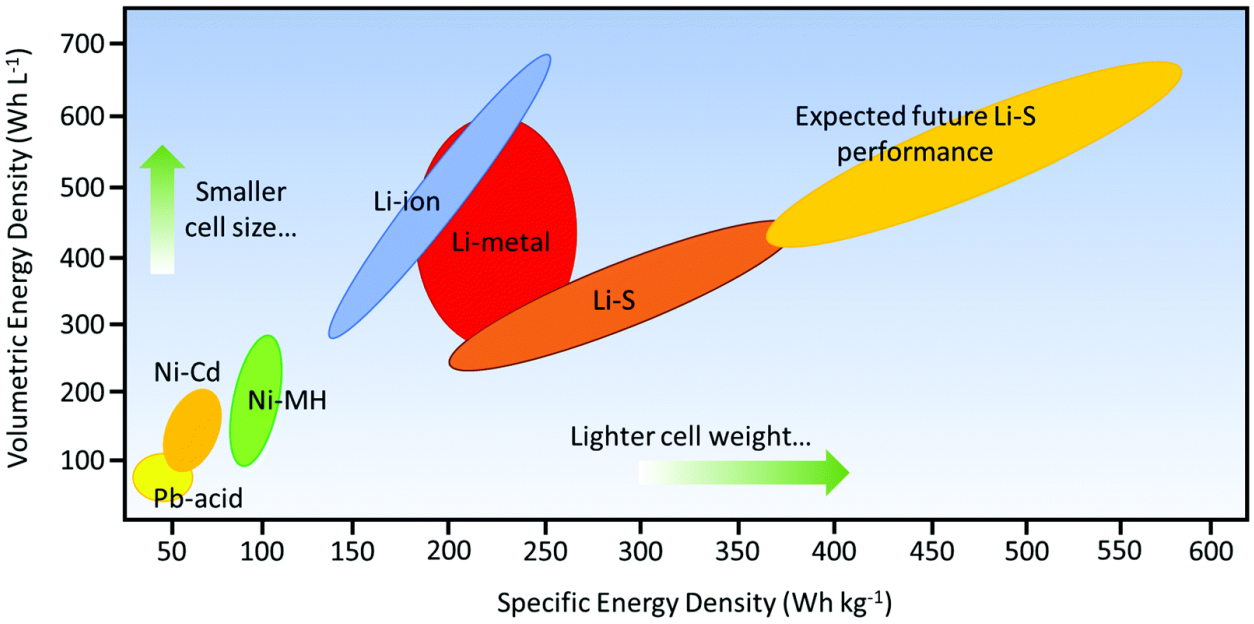

Figure 11: A Ragone diagram illustrating the range of specific energy and volumetric energy densities achievable for various electrical energy-storage technologies. It is important to recognize that the specific energy and power of the assembled battery pack is likely to be lower than that of the individual cells. Reprinted from Ref.,[140] with permission of the Royal Society of Chemistry.

the electrical power (P) is determined by the practical voltage (V) and resistance (R). This emphasises the importance of voltage in determining energy effectiveness, as:

$$P = V^2/R. \tag{5}$$

The efficacy of an electrochemical cell in providing energy to illuminate a light source or to operate an electric motor is significantly influenced by voltage. Based on their output voltages, electrochemical cells can be broadly classified according to their energy quality, as outlined in Table 4.

Table 4: Electrochemical cell energy quality rankings. The values are taken from Ref.[139]

Quality	Voltage Range (V)
High	3.5–5.5
Medium	1.5–3.5
Low	0.0–1.5

It should be noted that in electrochemical energy storage systems, the voltage characteristics must be aligned with the specific requirements of the application, with a focus on achieving the optimal balance between energy efficiency. While achieving the highest cell voltage may appear to be a beneficial strategy, this is not always the case, particularly in battery-powered semiconductor circuits where excessive voltage can lead to heat generation, which is a critical factor in the design of compact devices such as laptops.

Theoretically, cathodes with an average voltage of 2–4 V exhibit a high maximum theoretical specific energy (MTSE), which is defined as the energy per unit weight. This is given by the following equation:

$$\text{MTSE} = (xV/W_t)F \tag{6}$$

where W_t is the sum of the molecular weights of the reactants engaged in the intercalating reaction with a charge carrier concentration x, and V stands for the average voltage of this reaction. F is the Faraday constant.

5.2 The Charge Capacity

The total energy stored in an electrochemical system is the result of integrating the voltage over the charge capacity, which is the amount of charge available in the system. In other words,

$$Energy = \int V dq. \tag{7}$$

where, the output voltage (V) varies according to both the state of charge and the kinetic parameters of the battery, while q refers to the amount of electronic charge available to the external circuit. Understanding the maximum capacity, i.e. the theoretical amount of charge a battery can hold, is crucial. Similar to voltage, maximum charge capacity is a thermodynamic property, albeit of a different nature. Unlike voltage, which is independent

of the amount of material and considered an intensive property, charge capacity is extensive and dependent on the amount of material present in the electrode. Capacity is typically expressed in Coulombs per mole of material, per gram of electrode weight or per millimeter of electrode volume. The state of charge represents the current proportion of available capacity compared to the maximum.

5.3 Cycling Behavior

Batteries are expected to maintain their primary characteristics over numerous discharge and charge cycles. This is a significant practical hurdle and is a focus of battery development and improvement efforts. Figure 12 illustrates the decline in initial capacity over cycling, taking into account three different levels of Coulombic efficiency - the proportion of previous charge capacity available for subsequent discharge. This efficiency depends on several factors, in particular the current and depth of discharge per cycle.

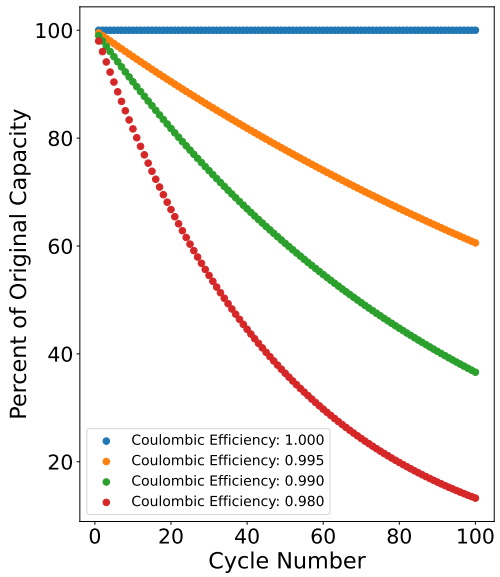

Figure 12: Influence of Coulombic efficiency upon available capacity during cycling.

Even small inefficiencies per cycle can have significant effects. For example, a loss of just half a percent per cycle will reduce the available capacity to just 78% of its original value after 50 cycles. By the 100th cycle, only 61% of the capacity remains at this rate, with an

even worse outcome if the Coulombic efficiency is lower.

Applications requiring a high number of operating cycles require cells to be designed and manufactured with a minimum loss of capacity per cycle. This requirement means compromising on other attributes. Supercapacitors, which are expected to have a large number of cycles, typically have much lower specific energy values than electrochemical cells used in applications where the amount of energy stored is the priority.

5.4 Self-Discharge

Another critical aspect in practical cells is self-discharge, where the available capacity decreases over time even in the absence of current flow through the external circuit. It is important to understand that the capacity of a cell is intrinsically linked to the electrodes and is determined by the ongoing chemical reactions between the neutral species within them. Any mechanism causing self-discharge must involve the transport of neutral species or the simultaneous movement of neutral combinations of charged species within the cell. When the latter occurs, it is electrochemical self-discharge because it involves the transport of charged species.

Various methods facilitate the movement of individual neutral species across a cell, such as transport through a nearby vapor phase, cracks in solid electrolytes, or as dissolved gases in a liquid electrolyte. These processes, without the transport of charged species, lead to chemical self-discharge. In addition, impurities can react with components in the electrodes or electrolyte, further reducing the available capacity over time.

5.5 Voltage curves

Voltage curves provide valuable insight into the electronic and structural changes that an electrode undergoes during cycling. For lithium-ion batteries with a metallic lithium reference anode, the voltage curve (V) is linearly related to the lithium chemical potential of the cathode ($\mu_{\mathrm{Li}}^{cathode}$). This lithium chemical potential is in turn derived from the Gibbs

free energy of the cathode, in particular for intercalation compounds, it reflects the slope (with an adjustment for a reference state) of the free energy with respect to the lithium concentration[141] (see Figure 13). The shape of the voltage profile thus provides insight into the insertion mechanism. For example, insertion of lithium into a solid solution produces a smooth, gradual voltage curve (Figure 13-left), whereas a two-phase reaction produces a plateau in the voltage profile due to the constant chemical potential across the common tangent bounding the two-phase region α and β (Figure 13-middle). Achieving the true equilibrium voltage, known as the open circuit voltage, requires very slow charge and discharge processes, measurable by galvanostatic or potentiostatic intermittent titration techniques (GITT or PITT). Normal charge and discharge cycles at typical rates deviate slightly from the true equilibrium curve due to sluggish kinetic processes such as diffusion, phase transitions and ohmic losses, resulting in polarization relative to the true equilibrium voltage curve. In addition, electrodes can undergo phase transformations, namely α, β, and γ, resulting in a discharge voltage profile with an inward step. This phenomenon is illustrated in Figure 13-right, where the discharge voltage curve (blue) contains two different plateaus.

Several discharge curves under low current or near equilibrium conditions are depicted in Figure 14. These curves illustrate the relationship between cell voltage and the state of charge parameter. The presentation of near equilibrium properties of these diverse cells aims to highlight significant behavioral differences, as evidenced by the shapes of their curves. Some discharge curves remain essentially flat ($LiFePO_4$), while others exhibit multiple flat regions ($LiMn_2O_4$), and some display a slanted and stretched S-shape (TiS_2), occasionally with a noticeable slope. These variations can be simplified into three fundamental types of discharge curve shapes, as illustrated in Figure 13.

In order to comprehend the potential for the electrode undergone phase transformations with an inward step it is essential to consider the phase diagram as illustrated in Figure 15a, where it is assumed that there are two stable binary phases, LiM and MX. In the absence of X, the composition proceeds along the Li-M edge of the ternary diagram, effectively

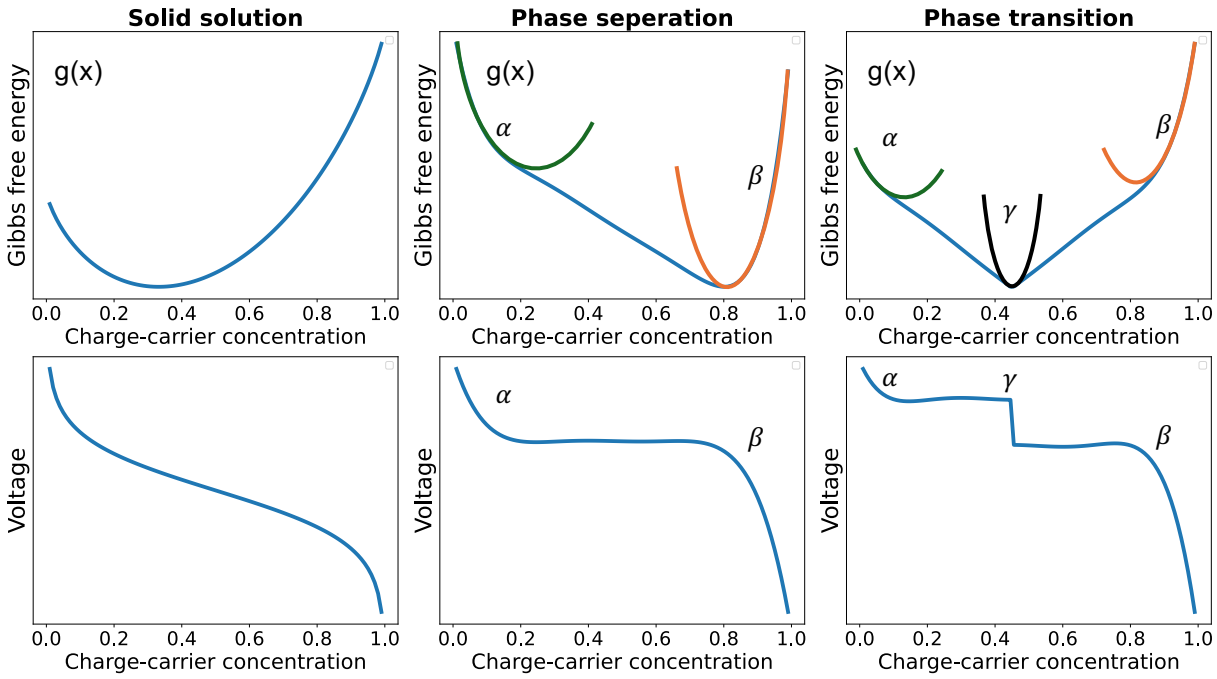

Figure 13: Representation of different types of discharge curves and their correlation with phase transformations. The Gibbs free energy (top) has been plotted for three different cathode materials and their corresponding voltage profiles (bottom) as a function of charge carrier concentration for the prototypical case of solid solution (left), phase separation (middle) into two α and β phases, and phase transformation (right) into three α, β, and γ phases.The relationship between the voltage curves and the slope of the Gibbs free energy of the electrode material is linear.

representing the binary Li-M system. Within this range, from pure M to LiM, there is a uniform potential plateau. The potential for pure lithium within this compositional range, denoted by triangle A in the ternary diagram, is given by

$$V_{\mathrm{A}} = -\frac{\Delta G_f(\mathrm{LiM})}{F}. \tag{8}$$

What happens when lithium reacts with a substance that initially contains some X? The overall composition follows a trajectory starting at the X-M boundary of the triangle and moving towards the lithium apex of the ternary diagram. The introduction of X into M does not change the plateau potential for compositions within triangle A. Consequently, there is a plateau at this potential, but its length varies depending on the initial composition.

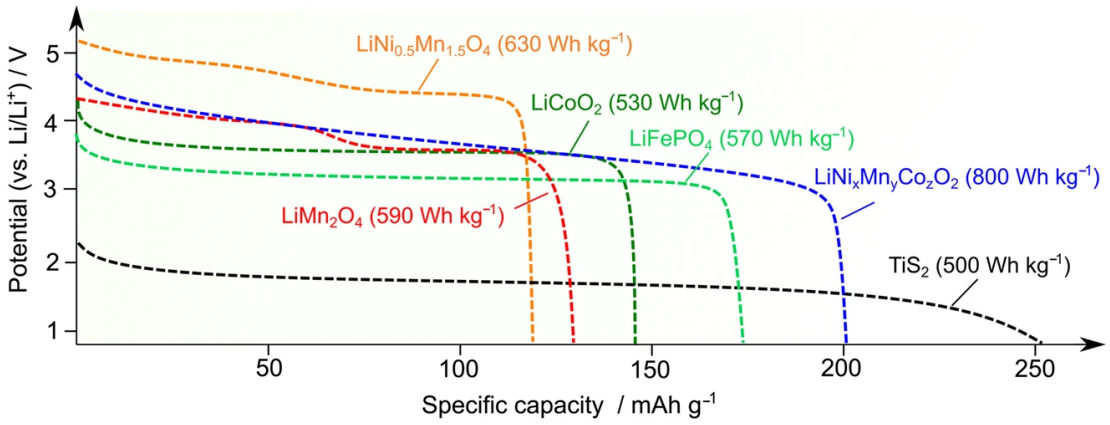

Figure 14: Example of battery discharge curves. The discharge profiles of TiS_2, $LiMn_2O_4$, $LiCoO_2$, $LiFePO_4$, $LiNi_{0.5}Mn_{1.5}O_4$ and $LiNi_xMn_yCo_zO_2$. The specific energy of each cathode is given in brackets, derived from the operating voltage of a Li-metal IC half-cell and the discharge capacity of each cathode.Voltage readings were taken in half cells relative to lithium metal. Reprinted from Ref.,[142] with permission from Springer Nature.

There is also an additional plateau at higher lithium concentrations as the total composition enters and passes through triangle B. The potential of compositions within this triangle is determined by

$$V_{\mathrm{B}} = -(\Delta G_f(\mathrm{MX}) - \Delta G_f(\mathrm{LiM}))/F. \tag{9}$$

Similarly to the binary Li-M system, when the total composition is in triangle C, the potential is that of pure lithium. These phenomena are illustrated in Figures 15a.

Figures 15b shows the variation of the electrode potential as a function of the total composition for three different initial electrode compositions as shown in Figures 15a. In all scenarios, the ratio of lithium stored per mole of M remains constant, but the mass of the electrode varies as a function of the relative weights of M and X. In addition, the average electrode potential tends towards that of pure lithium, which can be either beneficial or detrimental depending on whether the material serves as a negative or positive electrode in a lithium-based cell.

In practice, a binary system containing several intermediate phases may not be fully useful over its lithium composition range due to potential variations. In addition, poor

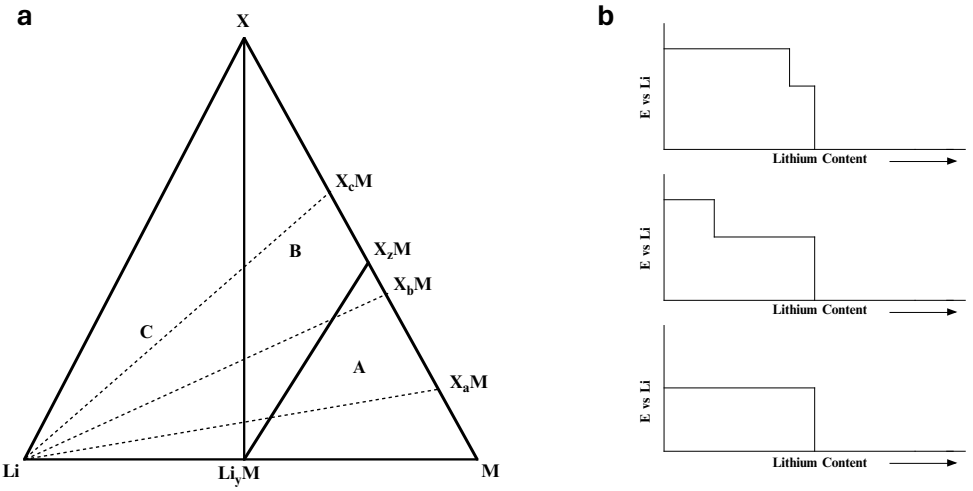

Figure 15: Schematic ternary phase diagram for the Li–M–X system. (a) Diagram illustrating the ternary phase relationships within the Li-M-X system, showing intermediate phases between the binary systems of Li-M and M-X. It delineates the composite composition paths for three different initial compositions by dashed lines. (b) Graph showing the fluctuation of the electrode potential upon the incremental addition of lithium for three different initial compositions: X_aM (top), X_bM (middle) and X_cM (bottom).

diffusion kinetics within one of the intermediate phases or the final phase can be problematic. Ternary systems offer numerous configurations, including those that accommodate ternary phases within the interior of the diagram. However, when screening potential systems for investigation, it is logical to start with systems with known binary and ternary phases.

6 Principles of Voltage in Electrochemical Cells

Assuming that an electrolyte acts as a selective barrier, allowing the passage of ionic entities while impeding the flow of electrons, the voltage of the cell (in the absence of current flow) is determined by differences in the chemically neutral compositions of the electrodes. Factors such as the properties of the electrolyte and the interactions at the electrode-electrolyte interfaces do not affect this voltage. Similarly, the electrode properties are critical in determining the capacity of the electrochemical cell.

Expanding on these basic concepts, this section looks in more detail at equilibrium or quasi-equilibrium states, focusing on the theoretical properties of systems that place upper

limits on critical parameters. However, real systems operating under load deviate from this ideal behavior. This deviation is mainly due to kinetic factors that vary between systems and depend on material properties, cell design and experimental settings. As a result, it becomes difficult to obtain consistent and quantifiable experimental results. This section examines the factors that govern equilibrium or near-equilibrium behavior.

6.1 Thermodynamic Properties of Individual Species

The primary driving force within a simple electrochemical cell is the change in Gibbs free energy, ΔG_r^0, alongside the hypothetical chemical reaction that takes place when substances within the electrodes interact. In the absence of current (open circuit conditions), this chemical driving force is balanced by an electrical driving force in the opposite direction.

The thermodynamic properties of a substance can be related to those of its constituents by using the concept of the chemical potential of a particular species. The chemical potential of a species "i" within a phase "j" is formally defined as

$$\mu_i = \partial G_j / \partial n_i \tag{10}$$

where the molar Gibbs free energy of phase j, denoted as G_j, and the mole fraction of species i in phase j, represented by n_i, can be expressed in integral form as follows:

$$\Delta \mu_i = \Delta G_j \tag{11}$$

As the amount of species i changes, so does the free energy of the phase, leading to similar dimensions between the chemical potential and the free energy. Consequently, variations in the chemical potential of species i will induce chemical forces that drive i towards regions of lower μ_i. In the absence of a net current in the electrolyte, this chemical force must be counterbalanced by an electrostatic force resulting from the voltage difference between the electrodes. The energy balance within the electrolyte, and therefore within the cell, can be

expressed in terms of the individual species i.

$$\Delta\mu_i = -z_i F V \tag{12}$$

The quantity of elementary charges carried by particles (ions) of species i is denoted as z_i. The chemical potential of a given species is linked to another thermodynamic parameter, known as its activity, denoted as a_i. This correlation is expressed by the following defining relation:

$$\mu_i = \mu_i^0 + RT \ln a_i \tag{13}$$

where μ_i^0 is a fixed value indicating the chemical potential of species i in its standard state. R is the gas constant and T is the absolute temperature. The activity of a given species refers to its effective concentration. If the activity of species i, denoted a_i, is unity, it behaves chemically as if it were pure i. Conversely, if a_i is 0.5, it indicates that the species is composed of half species i and is chemically inert to the other half. For properties such as vapor pressure, a substance with an activity of 0.5 has half the vapor pressure of pure i.

Consider an electrochemical setup where the reactivity of a substance, called species i, varies between the two electrodes: $a_i(-)$ for the negative electrode and $a_i(+)$ for the positive electrode. The difference in chemical potential between the positive and negative sides can be expressed as follows

$$\mu_i(+) - \mu_i(-) = RT \ln \left[a_i(+)/a_i(-)\right]. \tag{14}$$

When this difference in chemical potential is balanced by the counteracting electrostatic energy

$$V = -(RT/z_i F) \ln \left[a_i(+)/a_i(-)\right]. \tag{15}$$

This equation, known as the Nernst equation, relates the observable voltage of a cell to the chemical variance of an electrochemical cell. Essentially, it facilitates the conversion between chemical differences and electrical potentials. When the activity of a particular species at one electrode matches a standard reference, the Nernst equation gives the comparative electrical potential of the opposite electrode.

6.2 Potential Changes During Insertion Reactions

The electric potential externally measured at an electrode arises from the electrochemical potential of electrons contained within it η_{e^-}, commonly referred to as the Fermi level (E_F). Since potentials do not have absolute values, they are always evaluated as differences. The voltage across an electrochemical cell corresponds to the electrically measured difference between the Fermi levels of its two electrodes:

$$\Delta V = \Delta \eta_{e^-}. \tag{16}$$

The electrical potential measured at an electrode often varies as a function of its composition, particularly when guest species are introduced into or removed from the host material. The relevant compositional factor is the chemical potential of the electrically neutral electroactive species. When this species manifests as the cation M^+ within the electrode, the critical parameter becomes the chemical potential of neutral M, denoted μ_{M}. This is related to the electrochemical potentials of the ions and the electrons by

$$\mu_{\mathrm{M}} = \eta_{\mathrm{M}^+} + \eta_{e^-}. \tag{17}$$

Under open circuit conditions, there is no movement of ions across the cell. The driving force for ion flow within the electrolyte depends on the differential electrochemical potential

of the ions. This phenomenon is particularly evident in open circuit conditions as

$$\frac{d\eta_{\mathrm{M}^+}}{dx} = \Delta\eta_{\mathrm{M}^+} = 0. \tag{18}$$

Therefore, the open circuit voltage across the cell is directly related to the difference in the chemical potential of the neutral electroactive species in the two electrodes by

$$\Delta V = \Delta\eta_{e^-} = \frac{-1}{qz_{\mathrm{M}^+}}\Delta\mu_{\mathrm{M}}. \tag{19}$$

Standard practice is to represent both the difference in electrical potential (voltage) and the difference in chemical potential by subtracting the values at the left electrode from those at the right electrode.

A common method is to understand electron potentials based on the electron energy band model. Key aspects include the fluctuation of the density of available states with electron energy and the occupation of these states up to a maximum level determined by the chemical composition, known as the Fermi level.

In metals, the potential variation of available states is a continuous function of composition, allowing the application of free electron theory to express this relationship. In nonmetals, semiconductors and insulators, however, the density of states is discontinuous with respect to chemical composition. In certain potential ranges there are no states available for electron occupation. For example, simple semiconductors such as silicon or gallium arsenide have a valence band that is typically fully occupied, a band gap with no available states, and a conduction band with typically unoccupied states. The electron concentrations in these bands change with temperature due to thermal excitation and can be affected by dopants, changing the band occupancy. Optical excitation reflects the effects of thermal excitation.

In various materials, especially those with relatively low electronic conductivity, it is helpful to consider the relationship between energy state occupancy and changes in the

formal valence or charge of certain species within the host structure. For example, the introduction of an extra electron could change the formal charge of species such as W^{6+} to W^{5+}, Ti^{4+} to Ti^{3+}, Mn^{4+} to Mn^{3+}, or Fe^{3+} to Fe^{2+} in a transition metal oxide. Such occurrences are called redox reactions.

Consider a hypothetical case where an electrolyte is introduced into a lithium battery cell, as illustrated in Figure 16. For the sake of analytical clarity, we will ignore phenomena such as the formation of solid/electrolyte interphases, deeming them irrelevant to our current discussion. Since the electrolyte acts as an ionic conductor, the distribution of lithium ions must be balanced, especially when the external circuit is open. Consequently, the electrochemical potentials of the lithium ions at the anode, cathode and within the electrolyte medium must reach a state of equilibrium. However, a key question arises: How are the electronic energy levels realigned to precisely match their electrochemical potential difference with the V_{OC}? This complex phenomenon is elucidated by the formation of electric double layers (EDLs) at both the anode and cathode as the ion distribution equilibrium is established. The formation of these EDLs triggers potential changes at the electrodes, generating electric fields that harmonize the electrochemical potentials of the ions throughout the cell. At the same time, this process requires a counterbalancing readjustment of the electrochemical potentials of the electrons at the anode and cathode in opposite directions, ensuring that their disparity aligns with the V_{OC}. This emphasizes that the difference in the potential changes due to the formation of EDLs at the anode and cathode is intrinsically linked to the variation in the electrochemical potentials of the ions prior to the introduction of the electrolyte medium.

6.3 Electrical Double Layer

The electrical double layer is a fundamental model that describes the solid-liquid interface. It consists of a positively charged electrode surface layer and an adjacent negatively charged solution layer, which creates the Galvani potential difference. The Helmholtz model depicts solvated ions aligned along the electrode, separated by hydration shells, with the outer

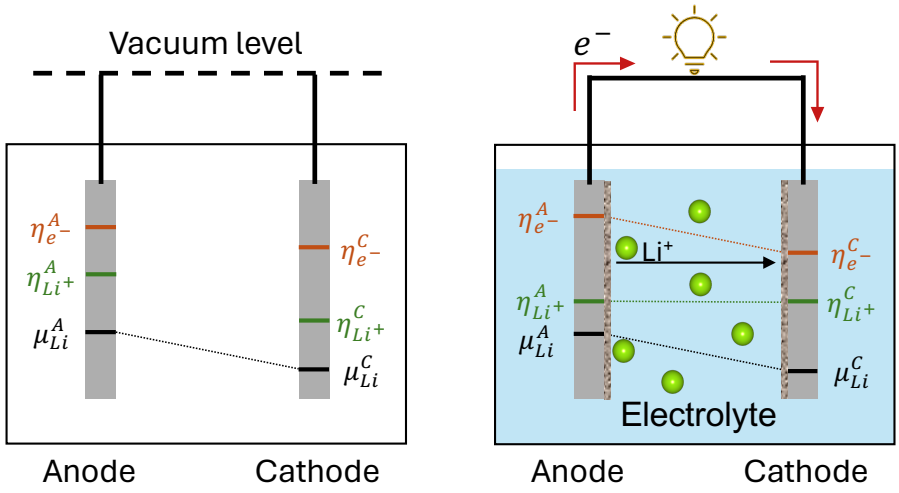

Figure 16: The chemical potential of lithium (μ_{Li}) as well as the electrochemical potentials of lithium ions (η_{Li^+}) and electrons (η_{e^-}) are examined for both anode and cathode materials. This analysis is conducted both prior to (left) and following (right) the introduction of an electrolyte under open-circuit conditions. It is important to emphasize that η_{Li^+} remains equal across the anode, cathode, and electrolyte when the electrode is submerged in the electrolyte. Dashed lines representing η_{Li^+} and η_{e^-} serve as visual aids and should not be interpreted as realistic potential curves.

Helmholtz plane (OHP) marking this arrangement (Figure 17a). Furthermore, the inner Helmholtz plane (IHP) is formed by ions bonded to the electrode after shedding their solvation shells. However, this structure is not accounted for in the model, as thermal motion disrupts it. In contrast, the Gouy–Chapman model incorporates thermal motion, which is analogous to the Debye–Hückel[143] model of the ionic atmosphere. This results in a more diffuse and dynamic ion distribution in the vicinity of the electrode surface (Figure 17b).

The electrical double layer establishes a potential gradient ($\Delta\phi$) across the electrode-electrolyte interface, influencing the equilibrium potential V_{eq}. This potential drop is governed by the Stern layer capacitance (C_{stern}), the diffuse layer capacitance (C_{dl}), and the surface charge density (σ):

$$\Delta\phi = \frac{\sigma}{C_{\mathrm{stern}} + C_{\mathrm{dl}}}$$

The double layer capacitance (C_{dl}) characterizes the charge storage capacity of the EDL

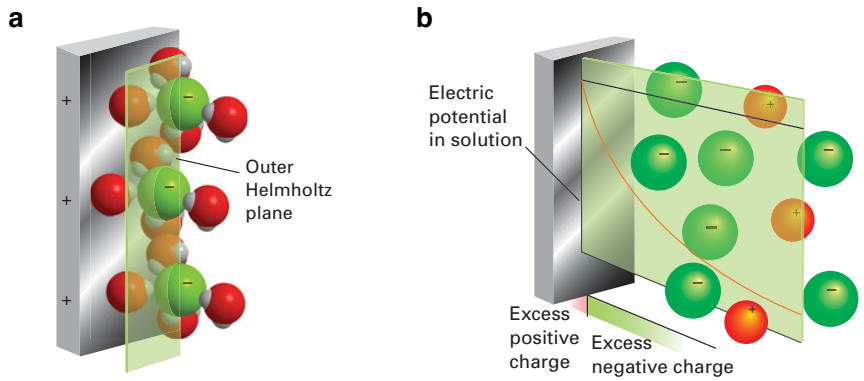

Figure 17: (a) A basic model of the electrode-solution interface conceptualizes it as two fixed charge planes: the outer Helmholtz plane (OHP), formed by ions and their solvating molecules, and the plane of the electrode itself. (b) The Gouy-Chapman model of the electrical double layer describes the outer region as a counter-charge atmosphere, similar to the Debye-Hückel theory[143] of ion atmospheres. The graph of electrical potential versus distance from the electrode surface illustrates the concept of the diffuse double layer.

and is related to the potential gradient ($\Delta\phi$) via:

$$C_{\mathrm{dl}} = \frac{dQ_{\mathrm{dl}}}{d\Delta\phi}$$

where Q_{dl} is the charge stored in the EDL. Higher C_{dl} values correspond to a greater charge storage capacity and a more pronounced potential gradient, leading to significant alterations in V_{eq} and, consequently, V_{OC}.

The composition of the electrolyte solution, including ion concentration and species mobility, influences the EDL's characteristics and, by extension, the V_{OC}. Changes in electrolyte composition alter the Stern layer capacitance (C_{stern}) and the diffusion properties of ions, impacting the charge distribution and potential gradient at the interface.

Understanding the interplay between the EDL and V_{OC} is essential for optimizing electrochemical cell design, enhancing energy efficiency, and ensuring long-term stability. Variations in EDL characteristics can affect the reversibility of electrochemical reactions, leading to fluctuations in V_{OC} over time and influencing cell performance.

Future research efforts will focus on developing advanced theoretical models and experimental techniques to elucidate the complex dynamics of the EDL and its role in determining

V_{OC}. Integration of fundamental electrochemical principles with advanced characterization methods will pave the way for the design of next-generation electrochemical devices with enhanced performance and reliability.

7 Structure of Interfaces in Electrochemical Devices

So far, the presence of the electrolyte at the electrochemical electrode/electrolyte interface in batteries has not been taken into account at all. It is evident that the properties of this interface are significantly influenced by the presence of the electrolyte. Nevertheless, the modeling of the electrolyte represents a significant theoretical and numerical challenge, particularly in the case of liquid electrolytes. In order to describe them properly, it is necessary to perform theoretical and numerically demanding statistical averages. To avoid this costly undertaking, a hierarchy of approximations has been developed. In contrast to the total energy, the free energy must be evaluated, including entropic contributions. In a grand-canonical approach, the electrolyte is not considered explicitly; rather, it is treated as a reservoir that provides the charge carriers, which are characterized by their electrochemical potential. In implicit solvent models,[144] the presence of the liquid electrolyte is accounted for as a dielectric continuum. Finally, the liquid electrolyte can be described explicitly in an atomistic manner. The following section will describe these approaches in detail.

7.1 Grand-Canonical Approach

In the grand canonical framework, the number of atoms within the systems under consideration remains variable. This framework, which is particularly relevant to interfacial structure, assumes that interfaces interact with thermodynamic reservoirs that host species capable of adsorption to or desorption from the interface. The energetic cost associated with transferring an atom or molecule between the reservoir and the interface is determined by the equilibrium chemical potential (μ_i) of the species, where 'i' represents either an atom or a

molecule. In particular, the properties of a reservoir remain unaffected by the extraction or addition of particles.

We subdivide the whole of the system being analyzed into three distinct subsystems: the electrode or solid, the gas phase and an interface region between these two subsystems. It is imperative that all three subsystems maintain thermodynamic equilibrium, which means that the chemical potentials of the species present in the system remain constant throughout. Any deviation from constancy in these chemical potentials would induce a particle flux that would restore equilibrium by re-establishing the constant chemical potential. The most appropriate thermodynamic potential to characterize such a system is the Gibbs free energy, denoted $G(T, p, N_i)$, where T is the temperature, p is the pressure and N_i is the particle numbers of the various species i.

At interfaces between electrochemical electrodes and electrolytes, the dynamics are significantly more complicated than at gas/surface interfaces,[145] as shown in Figure 18. In contrast to the sparse gas environment, a liquid electrolyte predominates at the electrode, housing dissolved anions and cations that confer electrical conductivity. In particular, the benchmark for calculating adsorption energies shifts from an atom or molecule in the gas phase to a dissolved species. Consequently, assessing the energy gain upon adsorption requires the investigation of solvation energies, a computationally intensive task.[146] To avoid the need to calculate the proton solvation energy in water, Nørskov et al.[147] proposed an alternative approach. By matching the reference potential to that of the standard hydrogen electrode, they established a relationship between the chemical potential (the free energy per H) for the reaction ($H^+ + e^-$) and that of $1/2H_2$. This basic principle laid the foundation for the "computational hydrogen electrode", a term coined in 2010.[148] However, the intricacies of this concept were initially explained in the supporting information (SI) of a later article.[148] We will revisit the derivation provided in the SI of that article. Of note is the departure from the use of the Standard Hydrogen Electrode (SHE) as in the aforementioned reference; instead, the authors here refer to the zero voltage definition relative to the

Reversible Hydrogen Electrode (RHE) as determined by the equilibrium of the reaction

$$\mathrm{H}^+ + e^- \rightleftarrows \frac{1}{2} + \mathrm{H}_2 \tag{20}$$

at all pH values and temperatures with H_2 at 1 bar pressure. Hence, it is possible to express the electrode potential of the proton-electron pair relative to the standard hydrogen electrode, taking into account the pH value and electrode potential U_{SHE},

$$\eta_{\mathrm{H}^+(aq)} + \eta_{e^-} = \frac{1}{2}\mu_{\mathrm{H}_2(g)} - eU_{\mathrm{SHE}} - k_B T \ln(10) pH. \tag{21}$$

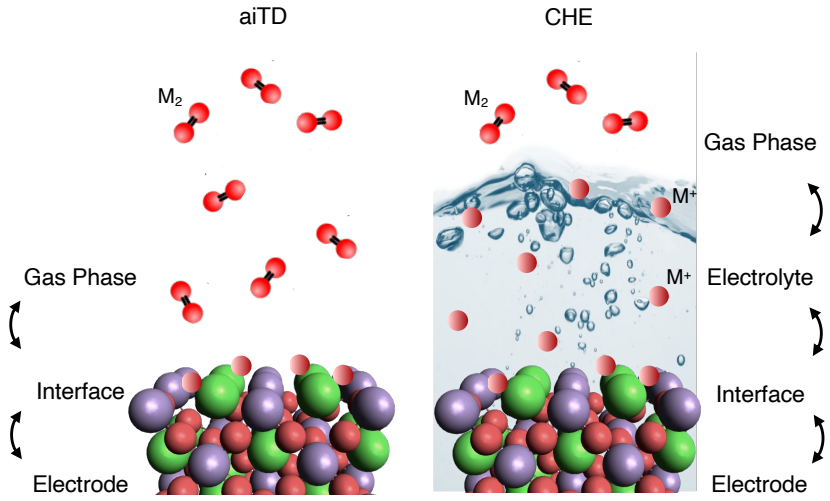

Figure 18: The illustration depicts the grand-canonical schemes to determine the equilibrium structure of gas–solid interfaces using the concept of *ab initio* thermodynamics (aiTD)[145] and of electrode–electrolyte interfaces using the concept of the computational hydrogen electrode (CHE).[147] Partially redrawn from Ref.[34]

However, the electrochemical potential remains constant whether the SHE or RHE reference is used, as the thermodynamic driving forces are identical. This computational hydrogen electrode (CHE) concept has predominantly been employed to investigate the structural stability of adsorbates at the interfaces of electrochemical electrodes and electrolytes,[149,150] as well as the potential-dependent adsorption energies of reaction intermediates in electrocatalysis.[148,151] It is crucial to emphasize that the applicability of the CHE framework extends

beyond the treatment of protons. Any solvated ionic species with an associated standard potential can be analyzed within this framework as follows:[149]

$$\eta_{\mathrm{M}^{z+}(aq)} + z\eta_{e^-} = \mu_{\mathrm{M}} - ze(U_{\mathrm{SHE}} - U_0) - k_B T \ln(a_{\mathrm{M}^{z+}}) \tag{22}$$

where U_0 is the reduction potential of the $\mathrm{M/M}^{z+}$ couple with respect to the SHE scale and pH is replaced by the activity $a_{\mathrm{M}^{z+}}$. In practice, this grand-canonical approach is often used to determine phase diagrams as a function of the electrochemical environment.This formalism can also be used to study the stability of intercalation compounds under given electrochemical conditions. This requires the insertion energy, which is analogous to the formation energy of the intercalation phase with respect to the pristine electrode material and the bulk phase of the charge carrier. In this way, the stable bulk phases can be evaluated at given electrochemical conditions, just as in the case of a surface. Furthermore, for a given electrode reaction, the CHE approach can also be used to determine the corresponding half-cell voltage with respect to the SHE.

Up to now, the derivation has been exact. In applications based on the concept of the computational hydrogen electrode the following approximations are typically made: firstly, the chemical potential of the gas phase species is taken in the limit of zero temperature and pressure; secondly, changes in the zero-point energies and entropy upon adsorption are neglected. This means that instead of the free energy, only total energies need to be calculated. The free energy of adsorption is then given by the following expression:

$$\Delta\gamma(U, a_i) \approx \frac{1}{A_s}\left(\frac{1}{2}E_{\mathrm{ads}}(\mathrm{M}_2) - N_{\mathrm{M}}\Delta\eta_{\mathrm{M}}(U, a_i)\right) \tag{23}$$

where the adsorption energy E_{ads} is evaluated with respect to the molecule M_2 in the gas phase, and $\Delta\eta_{\mathrm{M}}$ contains only the changes in the electrochemical potential as a function of electrode potential and activity. This expression only contains terms that can be conveniently calculated.

8 Method outlook

In the previous sections, we have presented the thermodynamic and kinetic characteristics that govern the properties of battery materials. In this section, we will examine the methodologies that are crucial for accurately predicting these properties. The field of multiscale simulation methodologies has evolved to encompass a range of techniques, including density functional theory (DFT),[152–154] *ab initio* molecular dynamics (AIMD),[155,156] reactive force field (e.g., ReaxFF) MD,[157] classical MD,[158] coarse-grained (CG) MD,[159] Monte Carlo (MC) method,[160] phase field method,[161] finite element method (FEM)[162] as shown in Figure 19. The multiscale covers the atomic scale, nanoscale, mesoscale (or microscale), and macroscale ($> 10^{-3}$ m).

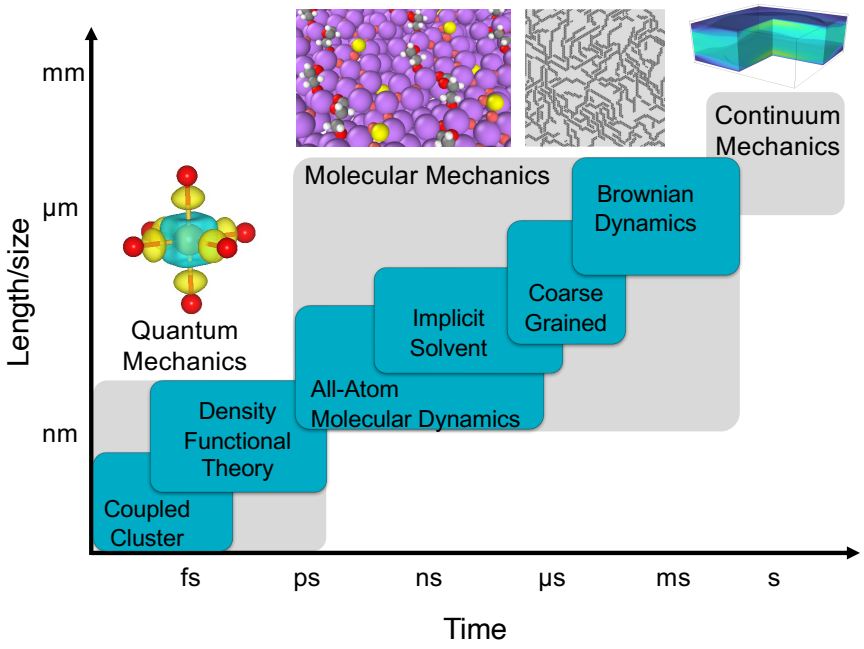

Figure 19: Approximate time and length scales characterizing various simulation techniques: quantum mechanics (QM), encompassing coupled cluster (CC) and DFT methods; molecular mechanics (MM), comprising all-atom molecular dynamics (AA-MD) simulations, implicit solvent, coarse-grained MD (IS-MD and CG-MD), and the Brownian dynamics (BD) technique; and continuum mechanics (CM). The depicted ranges represent an estimation of the time and length scales involved.

We focus on the atomic to mesoscale range, acknowledging the absence of strict scale

boundaries and emphasizing the unique challenges at each level. At the atomic scale, the central focus is on quantum effects and charge transfer dynamics. In contrast, at the nanoscale, the emphasis is on nonbonding interactions such as van der Waals forces. The method of choice for describing processes in bulk and interface systems is periodic electronic structure calculations based on DFT. It is acknowledged that DFT has certain limitations, including an inability to accurately predict band gaps and difficulties in describing strongly correlated systems, including some oxide materials. Nevertheless, DFT calculations combine numerical efficiency with sufficient reliability and accuracy for a multitude of properties pertinent to batteries. For instance, open circuit potentials and estimates of the gravimetric and volumetric density can be readily obtained through DFT calculations and employed as a computational screening tool for promising cathode/anode pairs.[163,164]

8.1 Density functional theory

Density functional theory (DFT)[152,153] is a remarkably powerful method, based on an exact theorem stating that the energy of the ground state is determined solely by the electron density, ρ. In a system with n electrons, the function $\rho(\mathbf{r})$ represents the total electron density at a given point $\mathbf{r}$ in space. The electronic energy is described as a functional of the electron density, $E[\rho]$. This implies that for any given function $\rho(\mathbf{r})$ there is a unique corresponding energy value.

8.1.1 Kohn-Sham orbitals and equations

The idea of a density functional for energy served as the basis for early, albeit helpful, approximate models such as the Thomas-Fermi method (derived from the work of E. Fermi and L.H. Thomas in the late 1920s) and the Hartree-Fock-Slater or X_α method[165] (derived from the work of J.C. Slater in the 1950s). However, in 1964 P. Hohenberg and W. Kohn[152] provided a formal proof that the ground state energy and all other electronic properties could be uniquely determined by the electron density. The Hohenberg-Kohn theorem does

not provide the explicit functional form linking energy and density; rather, it validates the presence of such a functional. The next significant advance in DFT came with the derivation of a set of one-electron equations capable of determining the electron density $\rho(\mathbf{r})$.

W. Kohn and L.J. Sham[153] demonstrated that the ground-state electronic energy E for a system containing n electrons can be expressed as

$$\begin{aligned} E[\rho] &= -\frac{\hbar^2}{2m_e}\sum_{i=1}^{n}\int \psi_i^*(\mathbf{r_1})\nabla_1^2\psi_i(\mathbf{r_1})d\mathbf{r_1} - \sum_{I=1}^{N}\frac{Z_I e^2}{4\pi\epsilon_0 \mathbf{r_{I1}}}\rho(\mathbf{r_1})d\mathbf{r_1} \\ &\quad + \frac{1}{2}\int \frac{e^2\rho(\mathbf{r_1})\rho(\mathbf{r_2})}{4\pi\epsilon_0 \mathbf{r_{12}}}d\mathbf{r_1}d\mathbf{r_2} + E_{XC}[\rho] \end{aligned} \tag{24}$$

where the one-electron spatial orbitals $\psi_i (i = 1, 2, ..., n)$ are the Kohn–Sham orbitals, the solutions of the equations given below. The exact electron density of the ground-state is then determined by

$$\rho(\mathbf{r}) = \sum_{i=1}^{n} |\psi_i(\mathbf{r})|^2 \tag{25}$$

where the sum is over all occupied Kohn-Sham (KS) orbitals; once these orbitals have been calculated, the value of ρ is determined. The first term in equation 24 represents the kinetic energy of the electrons, while the second term represents the attraction between electrons and nuclei, with the sum extending over all N nuclei indexed by I and having atomic number Z_I. The third term represents the Coulomb interaction between the aggregated charge distribution (summed over all KS orbitals) at positions $\mathbf{r_1}$ and $\mathbf{r_2}$. The last term is the exchange correlation energy, which remains elusive. This energy, denoted E_{XC}, is a functional of the density and includes all non-classical electron-electron interactions. Despite the assurance of the Hohenberg-Kohn theorem that E, and hence E_{XC}, must be functionals of the electron density, the exact analytical form of the latter remains unknown, necessitating the use of approximate expressions.

The KS orbitals are determined through the resolution of the Kohn-Sham equations,

which are formulated by employing the variational principle to the electronic energy $E[\rho]$, with the charge density specified in equation 25. The KS equations for the one-electron orbitals $\psi_i(\mathbf{r_1})$ are of the form

$$\Big\{-\frac{\hbar^2}{2m_e}\nabla_1^2 - \sum_{I=1}^{N}\frac{Z_I e^2}{4\pi\epsilon_0 \mathbf{r_{I1}}} + \int \frac{e^2\rho(\mathbf{r_2})}{4\pi\epsilon_0 \mathbf{r_{12}}}d\mathbf{r_2} + V_{XC}(\mathbf{r_1})\Big\}\psi_i(\mathbf{r_1}) = \varepsilon_i\psi_i(\mathbf{r_1}) \tag{26}$$

where ε_i are the KS orbital energies and V_{XC} is the exchange–correlation potential, derivative of the exchange–correlation energy:

$$V_{XC}[\rho] = \frac{\delta E_{XC}[\rho]}{\delta\rho} \tag{27}$$

If we know E_{XC}, we can derive V_{XC}. The significance of the KS orbitals lies in their facilitation of density computation using equation 25. These equations are iteratively solved in a self-consistent manner. Initially, we guess the electron density ρ, typically by employing a superposition of of atomic densities. Utilizing an approximate form for the functional $E_{XC}[\rho]$, which remains fixed throughout all iterations, we then calculate V_{XC} as a function of $\mathbf{r}$. The KS equations are subsequently solved to yield an initial set of KS orbitals. This set of orbitals is utilized to improve density calculation from equation 25, and the process iterates until density and exchange-correlation energy converge within a defined tolerance. The electronic energy is then determined using equation 24.

8.1.2 Exchange-correlation functionals

Numerous schemes have been developed to derive approximate forms of the exchange-correlation energy functional, and research is ongoing to improve its accuracy. The main error in density functional theory typically arises from the inherent approximation of this functional, which is commonly divided into exchange (related to the exchange energy) and correlation (related to the dynamic correlation energy) functionals. In the Local Density

Approximation (LDA),[166,167] the exchange-correlation functional is typically obtained by

$$E_{XC} = \int \rho(\mathbf{r}) \varepsilon_{XC}[\rho(\mathbf{r})] d\mathbf{r} \tag{28}$$

where ε_{XC} represents the exchange-correlation energy per electron in a homogeneous electron gas characterized by a constant density. With a homogeneous electron gas, an infinite number of electrons move through an infinitely large volume. This space maintains electroneutrality due to a uniform and widespread distribution of positive charge. While equation 28 serves as an approximation, since actual molecules do not distribute positive or electronic charge uniformly, the computationally efficient Local Density Approximation (LDA) offers surprisingly high accuracy, particularly in predicting structural properties. However, its accuracy decreases as the electron density in the system varies. For many molecules, LDA tends to overestimate binding energies compared to experimental results. To account for the non-uniform electron density, a non-local correction involving the electron density gradient is often incorporated into equation 28. Various gradient-corrected functionals have been proposed, the Generalized Gradient Approximation (GGA)[168] being one such approach. In general, GGA, an extension of LDA with gradient corrections, provides ground-state bond distances to within 0.03 a_0 atomic units and bond energies to within about 20 kJ/mol.

The next level of density functionals, known as meta-GGA,[169,170] goes beyond conventional models by including not only density gradients but also second-order density derivatives. These functionals can be redefined using the kinetic energy density as an additional parameter instead of the second order density derivatives. TPSS,[171] and SCAN[172] are functional in this context.

Another generation of functionals are hybrid functionals,[173,174] which use exact exchange from Hartree-Fock in conjunction with density functional exchange energy.

$$E_X^{HF} = -\frac{1}{2} \sum_{n,m} \int d\mathbf{r_1} \int d\mathbf{r_2} \frac{e^2 \psi_m^*(\mathbf{r_1}) \psi_n(\mathbf{r_1}) \psi_n^*(\mathbf{r_2}) \psi_m(\mathbf{r_2})}{4\pi\epsilon_0 \mathbf{r_{12}}} \tag{29}$$

The $\psi_n(\mathbf{r})$ is the Kohn-Sham wave functions. The rationale behind this method is based on the adiabatic connection formula,[175,176] which formulates the exchange-correlation energy as a convolution of the exchange and correlation potential energies over a spectrum of interaction strengths represented by λ. In this framework, the interaction component of the Hamiltonian is proportionally adjusted by λ, yielding a universal functional, which depends on λ and the electron density. The energy resulting from these interactions can thus be formulated as a function of λ.

The basic concept of hybrid functionals is to use an interpolation method to fit the integrand between its end points. When λ (the interpolation parameter) is equal to zero, the integrand corresponds exactly to the exchange energy of the non-interacting condition. Conversely, in the presence of full interaction, the LDA or GGA functionals are appropriately applied. Consequently, a linear interpolation approach would result in

$$E_{XC}[\rho] = \int_0^1 d\lambda U_{XC}^{\lambda\hat{W}}[\rho] = \frac{1}{2}\left(U_{XC}^0 + U_{XC}^{\hat{W}}\right) = E_{XC}^{GGA} + \frac{1}{2}\left(E_X^{HF} - E_X^{GGA}\right) \tag{30}$$

Perdew[177] has argued that a factor of $\frac{1}{4}$ would actually be better than a factor of $\frac{1}{2}$. Hybrid functionals exhibit superior performance compared to GGA functionals regarding binding energies, band gaps, and reaction energies. However, they exhibit limitations in describing solids due to the extensive nature of the exact exchange hole within a solid. The elongated range of this hole leads to long-range tails, which are swiftly neutralized upon interaction activation by correlation effects. To address this, it is proposed to utilize a reduced mixing factor for the long-range portion of the exchange hole. This adjustment involves truncating the extended interaction range when computing the Hartree-Fock exchange,[178] resulting in enhanced band gap accuracy and decreased computational complexity.[179]

From a different perspective, Anisimov et al. [180] introduced the LDA+U method to address a specific challenge in the accurate description of transition metal oxides. These materials often exhibit Mott insulator behavior, contrary to the predictions of GGA calcu-

lations, which often classify them as metals. To correct for this, they included a correlation term[181] inspired by the Hubbard model and corrected for double counting with E_{dc}.

Novak et al. [182] further linked this method to hybrid functionals by restricting the exact exchange contribution to a defined orbital shell. Unlike LDA+U, where the Coulomb matrix elements are attenuated by a screening factor, hybrid functionals modulate these interactions by a mixing factor. Both approaches, LDA+U and local hybrid,[183] share the common feature of significantly reducing off-site matrix element contributions to the interaction. Sotoudeh et al. [183] applied this method to transition metal oxides and obtained results similar to those obtained by full implementation of hybrid functionals.[184]

8.1.3 Self-interaction Error

The standard DFT calculations based on GGA functionals reflect a systematic tendency to underestimate the experimentally determined voltages of layered lithium transition metal oxides by up to 1.0 V, as shown in Figure 20.

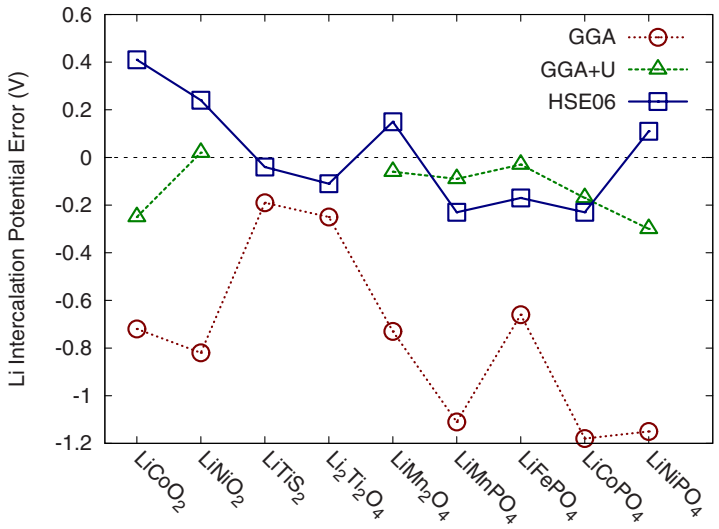

Figure 20: A comparative analysis of intercalation voltage errors using different calculation methods: GGA (Generalised Gradient Approximation), represented by red circles, GGA+U, represented by green triangles, and the HSE06 (Heyd-Scuseria-Ernzerhof)[178] hybrid functional, represented by blue squares. Note that the Hubbard U value for titanium (Ti) is set to zero, making GGA equivalent to GGA+U. Reprinted from Ref.,[185] copyright American Physical Society.

The inability of DFT to accurately predict the stresses in lithium transition metal oxides is due to a fundamental problem within (semi-)local DFT methods. Specifically, the mean-field approximation used to describe the electrostatic interaction between electrons introduces a self-interaction problem. This self-interaction, where each electron interacts with itself, remains inadequately accounted for by the commonly used LDA and GGA functionals. As a consequence, this self-interaction error leads to an artificial dispersion of the electrons, which particularly affects systems with strongly correlated electrons.[186] For example, many transition metal oxides exhibit distinct electron density features, such as localized *d*-electrons at metal centers, which are not captured by conventional DFT calculations. In particular, GGA often incorrectly predicts metallic ground states for insulating transition metal oxides relevant to lithium-ion batteries.[186] Even in simple cases such as the oxidized water dimer, DFT calculations using GGA functionals incorrectly predict both the energetics and the electronic structure of the dimer.[187]

While error-correction mechanisms within DFT can mitigate this problem in scenarios such as energetic comparisons of different polymorphs, such approaches prove inadequate for modeling redox reactions. Such reactions require the calculation of energy differences between materials with very different electronic configurations, which precludes effective error cancellation. Chevrier et al.[185] showed that hybrid DFT calculations using the HSE06[178] functional show comparable accuracy in predicting redox potentials compared to the GGA+U method, albeit without the need for additional parameters. However, even with the application of HSE06,[178] notable discrepancies between predicted and observed voltages can occur in systems with complicated electronic structures, such as Li_xCoO_2, which undergoes a metal-insulator transition upon delithiation. Seo et al. [188] observed that fine-tuning the amount of exact exchange according to system-specific parameters derived from spectroscopic reference band gaps can further improve the accuracy of calculated equilibrium voltages and voltage profiles within hybrid functional DFT. Figure 20 shows a comparison of equilibrium voltages between lithium transition metal oxides and phosphates calculated

using GGA, GGA+U and HSE06.[178]

8.2 Equilibrium cell voltage from first principles

It is currently possible to estimate many important macroscopic properties of batteries with a satisfactory degree of accuracy using fundamental results derived from DFT structural relaxation and energy calculations.[141,189] For example, the average voltage (relative to a metallic anode) of a M_nX cathode when charged to $M_{n-x}X$ can be correlated with the change in Gibbs free energy, which in turn can be approximated by the shift in the 0 K DFT energy,[190] as follows

$$\begin{aligned} V &= -\frac{G[\mathrm{M}_n\mathrm{X}] - G[\mathrm{M}_{n-x}\mathrm{X}] - xG[\mathrm{M}]}{xe} \\ &\approx \frac{E_{\mathrm{DFT}}[\mathrm{M}_n\mathrm{X}] - E_{\mathrm{DFT}}[\mathrm{M}_{n-x}\mathrm{X}] - xE_{\mathrm{DFT}}[\mathrm{M}]}{xe} \end{aligned} \tag{31}$$

where x represents the quantity of M transferred per unit during this process. G stands for the Gibbs free energy, E_{DFT} represents the energy computed through DFT, and e signifies the charge of an electron. This expression arises from the integration of the Nernst equation across a range of M composition denoted by x. It serves as a useful approximation for estimating the voltage of intercalation compounds like $LiFePO_4$, which undergo a two-phase reaction (as previously illustrated in Figure 14), under the assumption that all intermediary stable phases are accurately identified using DFT. However, this approximation overlooks finite-temperature effects and thus cannot accurately predict the voltage behavior of intercalation compounds that operate via a solid solution mechanism.

Additional properties that can be predicted by DFT calculations and crystallographic analysis include theoretical specific capacity and volumetric capacity. The theoretical specific and volumetric capacities are determined by dividing the number of lithium ions that can be extracted per unit formula by the total molecular weight and volume (sometimes obtained by DFT relaxation) per unit formula, respectively. Consequently, multiplying the average

voltage by the theoretical specific capacity and volumetric capacity gives the theoretical specific energy and energy density respectively.

Nevertheless, as battery structures can be rather complex, particularly at the interface between electrode and electrolyte, DFT calculations are sometimes too numerically demanding to describe these structures. In the case of a liquid electrolyte, instead of explicitly considering the solvent molecules, they might be described within an implicit solvent model,[144] i.e., as a continuous dielectric. This approach is numerically attractive and yields reasonable trends for electrochemical electrode/electrolyte interfaces,[191] but it is not clear how reliable the method is in terms of quantitative results.

8.3 Thermodynamics from Electronic Structure

Statistical mechanics[192] facilitates the correlation between the temperature-dependent macroscopic properties of a battery material and its intrinsic electronic configuration. The fundamental concept driving this relationship is encapsulated in the partition function equation which, under conditions of constant temperature and lithium concentration, assumes the following formulation:

$$Z = \sum_i \exp^{-\beta E_i} \tag{32}$$

where Z is the partition function, which denotes the total statistical sum of the system; i indexes the different quantum states of the system; E_i is the energy associated with the ith state (excitation), which can be determined via DFT; k_B is the Boltzmann constant, a fundamental constant in thermodynamics; and finally T is the temperature of the system.

Three categories of excitations can be distinguished in intercalation compounds: (i) electronic excitations, which involve events such as the transition of a valence band electron to a conduction band; (ii) vibrational excitations, which arise from the thermal motion of atoms around their ideal crystalline positions; and (iii) configurational degrees of freedom, which

are related to the different arrangements of charge carriers (e.g. Li ions) and vacancies in the interstitials of the intercalation host. While electronic and vibrational excitations have a quantitative impact on thermodynamic potentials, the most significant contribution to the thermodynamic properties of intercalation compounds comes from configurational degrees of freedom. These configurational excitations are not limited to the distribution of charge carriers and vacancies within a host, but can also arise from the different ways in which different localized oxidation states are distributed, which is particularly evident in compounds with localized electronic states. For example, the configurational entropy arises from all possible distributions of +2 and +3 oxidation states on the Fe sites of the olivine host Li_xFePO_4.[193]

The Helmholtz free energy is correlated with the partition function by the expression $F = k_B T \ln Z$. Various thermodynamic properties can then be derived by taking suitable derivatives of the free energy with respect to experimentally manipulable parameters.

8.4 Formation Energy and Stability

A prerequisite for the application of any material is its stability under certain conditions. Thermodynamic stability, a crucial aspect, is determined by the Gibbs energy of decomposition (ΔG_d), which represents the energy difference between the formation of the material (ΔG_f) and that of all other compounds in the relevant chemical context. Despite the challenges of incorporating temperature-dependent thermodynamics into high-throughput density functional theory (DFT) and the limited application of machine learning (ML) methods in this area,[194] material stability is predominantly evaluated using the decomposition enthalpy (ΔH_d).[195] This metric approximates the energy difference between a given compound and competing compounds within a defined chemical context.

The quantity ΔH_d is obtained by a convex hull construction in the formation enthalpy (ΔH_f) composition space. Figure 21 shows an example of a binary A-B space with three known compounds, A_4B, A_2B and AB_3. The convex hull is the lower convex enthalpy envelope that lies below all points in the composition space (blue line). Stable compositions

lie on the convex hull and unstable compositions lie above it. A_4B is unstable (above the hull), so $\Delta H_d > 0$ and is calculated as the distance in ΔH_f between A_4B and the convex hull of stable points. AB_3 is stable (on the hull) so $\Delta H_d < 0$ and is calculated as the distance in ΔH_f between AB_3 and a hypothetical convex hull constructed without AB_3 (dashed line). So ΔH_d is the minimum amount that ΔH_f must decrease for an unstable compound to become thermodynamically stable, or the maximum amount that ΔH_f can increase for a stable compound to remain stable. Note that ΔH_d provides a distribution of values for stable compounds, whereas the more common "energy above the hull" is equal to 0 for all stable compounds. The convex hull construction described here for a binary system generalizes to chemical spaces consisting of any number of elements.

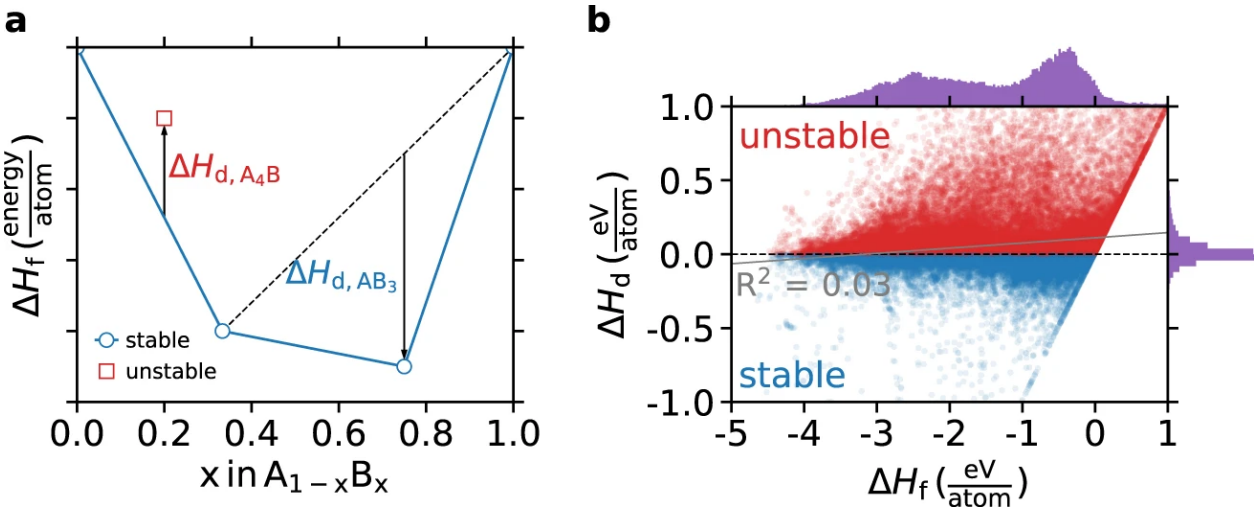

Figure 21: The distinction between formation and decomposition energies. (a) A convex hull is constructed to derive the decomposition enthalpy (ΔH_d) from the formation enthalpy (ΔH_f). (b) An analysis of 85,014 ground state records in the Materials Project shows minimal correlation between ΔH_d and ΔH_f. Interestingly, a strong linear correlation only appears for chemical spaces containing a single compound, which represents about 3% of the compounds analyzed. These singular compounds were excluded from the determination of the correlation coefficient, R^2. In addition, a normalized histogram of ΔH_f (and ΔH_d) is shown, binned every 10 meV/atom, providing further insight into the energy distributions. Reprinted from Ref.,[196] with permission from Springer Nature.

Therefore, while ΔH_f. measures how likely a compound is to form from its constituent elements, the thermodynamic factor governing phase stability is ΔH_d, which emerges from

the interplay among ΔH_f values for all compounds within a chemical system. While the enthalpies of formation can reach several electron volts (eV), ΔH_d typically falls within a range one to two orders of magnitude lower. Furthermore, thermodynamic stability exhibits nonlinear behavior with respect to ΔH_d, particularly around zero; negative values signify stable compounds, while positive values indicate instability or metastability.

Although ΔH_d dictates stability, machine learning (ML) models typically predict the absolute ΔH_f as the standard thermodynamic property.[197,198] This preference largely stems from the fact that ΔH_f is inherent to a specific compound, whereas ΔH_d relies inherently on a compound's stability concerning neighboring compositions, rendering it less suitable for direct learning.

Using data from the Materials Project (MP),[199] Bartel et al.[200] used the convex hull method to derive ΔH_d values for 85,014 inorganic crystalline solids, mainly from the Inorganic Crystal Structure Database (ICSD).[201,202] These values were then plotted against ΔH_f in Figure 21. Their analysis reveals a lack of significant linear correlation between ΔH_d and ΔH_f, except in cases where only one compound occupies a chemical space ($\Delta H_d = \Delta H_f$), a scenario observed in only $\sim$3% of materials within the MP. While ΔH_f exhibits a wide range of energies (mean $\pm$ mean absolute deviation $= -1.42 \pm 0.95$ eV/atom), ΔH_d exhibits a much narrower range of energies (0.06 ± 0.12 eV/atom), indicating the greater sensitivity or subtlety of ΔH_d in prediction. Histograms illustrating the distributions of ΔH_f and ΔH_d are shown in Figure 21. Despite the lack of a linear relationship between ΔH_d and ΔH_f, and the limited energy span of ΔH_d, predictive models based on ΔH_f could still accurately predict ΔH_d, provided they account for relative variations in ΔH_f within a given chemical space with a precision comparable to the range of variation in ΔH_d. Alternatively, such models could benefit from significant error reduction when comparing energies of compounds with similar chemical properties.

8.5 X-ray absorption near-edge spectroscopy

Having established the principles of stability, we now turn our attention to probing the electronic structure, oxidation states, and local chemical environments of elements within a material. X-ray absorption near-edge spectroscopy (XANES) is a technique that is widely used for this purpose in material characterization, particularly in experimental settings. In this method, a nuclear electron is excited into valence or conduction bands. In semiconductors and insulators, where electrons tend to remain localized on atoms, it is essential to accurately account for electron-hole interactions in calculations. The two main methods used for this purpose are the supercell core-hole (SCH)[203] method and the Bethe-Salpeter equation (BSE)[204] method.

The supercell core-hole method involves the targeted removal of a specific core electron, resulting in a positive charge vacancy. To simulate the subsequent excitation of this electron to higher energy states, an electron is added to the valence or conduction band to mimic the final state of the excitation process, a technique known as final state approximation. This configuration allows a comprehensive electronic minimization process to be carried out. In metals, the core hole is effectively shielded by the surrounding electrons, leading to negligible discrepancies between core hole and regular calculations. However, in semiconductors and insulators, where the screening is weak, strong electron-hole interactions occur, causing not only a reduction in excited state energies relative to the valence states, but also significant changes in the band structure. Consequently, the primary effect in core-hole calculations is the relaxation of valence and conduction electrons, while the relaxation of core states is typically negligible. This property facilitates smooth integration into a projector augmented wave (PAW)[205] framework without the need for real-time recalculation of PAW potentials at each step of the electronic self-consistent cycle.

It is crucial to use sufficiently large supercells to minimize interactions between neighboring core holes within periodic boundary conditions. Consequently, the computational cost of this method is primarily due to the use of large supercells. Nevertheless, it is generally

more computationally efficient than the BSE[204] method for core electrons.

The dielectric function utilized in the SCH method is approached by considering electromagnetic wave wavelengths, which are typically much larger than the characteristic momenta within solids. We initiate the analysis by focusing on the transverse expression for the imaginary component of the dielectric function under conditions of long wavelengths. This expression is represented as:

$$\epsilon^{(2)}_{\alpha\beta}(\omega, \mathbf{q}=0) = \frac{4\pi^2 e^2 \hbar^4}{\Omega \omega^2 m_e^2} \sum_{c,v,\mathbf{k}} 2w_{\mathbf{k}} \delta(\varepsilon_{c\mathbf{k}} - \varepsilon_{v\mathbf{k}} - \omega) \times M_\alpha^{v\to c} M_\beta^{v\to c*} \tag{33}$$

In this formula, $\epsilon^{(2)}_{\alpha\beta}(\omega, \mathbf{q}=0)$ denotes the imaginary part of the dielectric function for transverse polarization. Various parameters such as e (elementary charge), $\hbar$ (reduced Planck's constant), Ω (volume of the unit cell), ω (angular frequency), m_e (electron mass), $\varepsilon_{c\mathbf{k}}$ and $\varepsilon_{v\mathbf{k}}$ (energies of conduction and valence bands, respectively, at momentum $\mathbf{k}$), $w_{\mathbf{k}}$ (weight of the $\mathbf{k}$ point in the Brillouin zone), and $M_\alpha^{v\to c}$ (matrix elements for transitions from the valence to conduction band) are involved.

In the PAW method, all-electron orbitals $|\psi_{n\mathbf{k}}\rangle$ are obtained through a linear transformation of pseudo orbitals $|\tilde{\psi}_{n\mathbf{k}}\rangle$:

$$|\psi_{n\mathbf{k}}\rangle = |\tilde{\psi}_{n\mathbf{k}}\rangle + \sum_i (|\phi_i\rangle - |\tilde{\phi}_i\rangle)\langle \tilde{p}_i | \tilde{\psi}_{n\mathbf{k}}\rangle. \tag{34}$$

The pseudo orbitals depend on band index n and crystal momentum $\mathbf{k}$. $|\phi_i\rangle$, $|\tilde{\phi}_i\rangle$, and $|\tilde{p}_i\rangle$ represent all-electron partial waves, pseudo partial waves, and projectors respectively. The index i denotes the atomic site and other relevant quantities at each site. Matrix elements are given by:

$$
\begin{aligned}
M_{\alpha}^{v\to c} &= \langle \psi_{c\mathbf{k}} | i\nabla_{\alpha} - \mathbf{k}_{\alpha} | \psi_{v\mathbf{k}} \rangle \\
&= \langle \tilde{\psi}_{c\mathbf{k}} | i\nabla_{\alpha} - \mathbf{k}_{\alpha} | \tilde{\psi}_{v\mathbf{k}} \rangle \\
&\quad + \sum_{ij} \langle \tilde{\psi}_{c\mathbf{k}} | \tilde{p}_i \rangle \langle \tilde{p}_j | \tilde{\psi}_{v\mathbf{k}} \rangle i(\langle \phi_i | \nabla_{\alpha} | \phi_j \rangle - \langle \tilde{\phi}_i | \nabla_{\alpha} | \tilde{\phi}_j \rangle).
\end{aligned} \tag{35}
$$

In X-ray absorption spectroscopy, focusing on one core hole at a single site allows simplification of equations. The index i now enumerates the main, angular, and magnetic quantum numbers. Utilizing the completeness relation, the matrix elements simplify to:

$$
M_{\alpha}^{\text{core}\to c\mathbf{k}} = \sum_{i} \langle \tilde{\psi}_{c\mathbf{k}} | \tilde{p}_i \rangle \langle \phi_i | \nabla_{\alpha} | \phi_{\text{core}} \rangle. \tag{36}
$$

Additionally, the summation over bands can be limited to conduction bands c:

$$
\epsilon_{\alpha\beta}^{(2)}(\omega) = \frac{4\pi^2 e^2 \hbar^4}{\Omega \omega^2 m_e^2} \sum_{c,\mathbf{k}} 2w_{\mathbf{k}} \delta(\varepsilon_{c\mathbf{k}} - \varepsilon_{\text{core}} - \omega) \times M_{\alpha}^{\text{core}\to c\mathbf{k}} M_{\beta}^{\text{core}\to c\mathbf{k}*}. \tag{37}
$$

Similar to XANES, electron energy-loss near-edge structure (ELNES) focuses on the excitation of core electrons, but it is a part of the broader electron energy-loss spectrum (EELS). EELS captures the energy lost by electrons as they pass through a material, with ELNES specifically highlighting the contributions from core electron excitations to empty orbitals of a given element.

As an example, the detailed comparison of the Ti $L_{2,3}$ fine structure of TiS_2 before and after the first cycle is shown in Figure 22. The Ti-3d character of the pristine sample was characterized by the presence of three-fold degenerate t_{2g} states (shoulder peaks) and two-fold degenerate e_g states (peaks at 459.2 eV and 464.9 eV). The crystal field splitting (t_{2g} – e_g) is reasonably resolved in TiS_2, as evidenced by the clear shoulder peaks at 457.4 eV and 463.1 eV. However, upon discharging the system, the shoulder peaks disappeared. This indicates a reduction in the t_{2g} – e_g splitting of the Ti $L_{2,3}$ edge, which is characteristic of

the reduction of Ti. Furthermore, the Ti $L_{2,3}$ edge was shifted by approximately 0.7 eV to lower energies, which confirmed the reduction of the Ti oxidation state. Upon charging, the Ti $L_{2,3}$ edge shifted back to its previous position, while the shoulder peaks reappeared. This demonstrated a consistent reversible redox process. The calculated density of states (DOS) in conjunction with the calculated EELS data also supported the aforementioned findings, as illustrated in Figure 22. In the case of TiS_2, the filled valence band, which extends from -5.5 eV to 0 eV, is predominantly of S-p character, with a minor contribution from Ti-d orbitals. The Ti-d states that are relevant for the redox properties are predominantly located above the Fermi level between 0 and 4 eV. Upon transitioning from TiS_2 to $LiTiS_2$, the monovalent Li ions are introduced into the system, resulting in the filling of the σ^* states with additional electrons. The results of the density of states (DOS) calculations indicated that the Ti states were occupied. A detailed examination of the spectral region of interest in the calculated EELS revealed that the redox activity is associated with peaks that lie within the energy window from 0 to 3 eV. The disappearance of the lower peak corresponding to the Ti-t_{2g} orbital after Li insertion was in accordance with the measured EELS data, thereby further verifying that Ti is the center of the redox reaction.

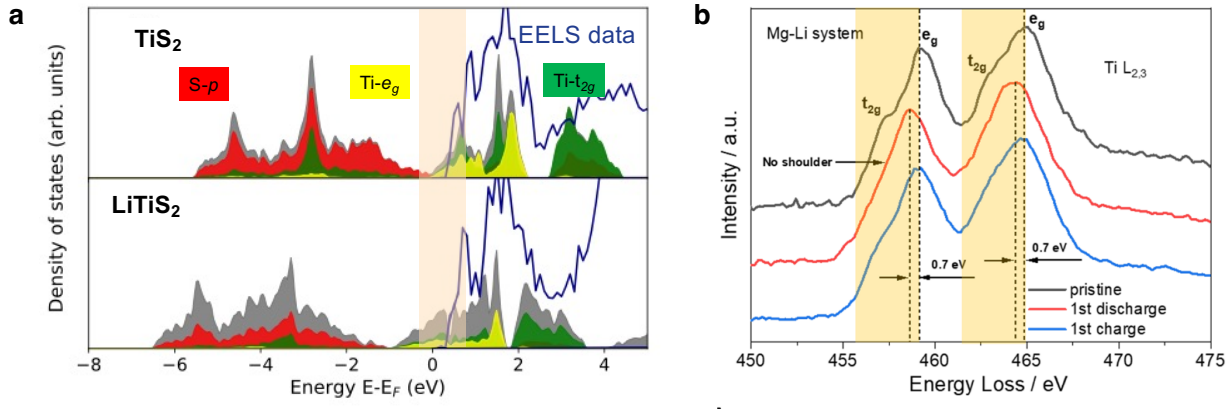

Figure 22: (a) The calculated density of states of (DOS) of TiS_2 (top) and $LiTiS_2$ (bottom) structures. The graphs show the total DOS (grey) and the projected DOS for S-p (red), Ti-t_{2g} (green), Ti-e_g (yellow) states. The calculated EELS data is represented by dark blue color.(b) EELS spectra of TiS_2 in the Mg-Li systems. Reprinted from Ref.,[206] published under a CC BY license.

8.6 Crystal Orbital Hamiltonian Population

Crystal Orbital Hamiltonian Population (COHP)[207] analysis is a powerful method employed in computational materials science to dissect and understand chemical bonding interactions within crystalline materials. COHP relies on quantum mechanical principles to elucidate the nature of chemical bonding in solids. To grasp the theoretical underpinnings of COHP, it is important to gain a comprehensive understanding of the fundamental concepts that underpin electronic structure calculations, density functional theory (DFT), and Hamiltonian matrices. In DFT, the electronic structure of a material is described by the Kohn-Sham equations:

$$H_{KS}\psi_i(\mathbf{r}) = \varepsilon_i\psi_i(\mathbf{r})$$

where H_{KS} is the Kohn-Sham Hamiltonian operator, $\psi_i(\mathbf{r})$ are the Kohn-Sham orbitals, and ε_i are the corresponding eigenvalues. The electronic Hamiltonian matrix elements H_{ij} describe the interaction between electrons on different atoms. These elements can be expressed as:

$$H_{ij} = \langle\psi_i|H_{KS}|\psi_j\rangle$$

The overlap population, denoted as P_{ij}, quantifies the overlap of Kohn-Sham orbitals between pairs of atoms. It is computed as:

$$P_{ij} = \sum_{\alpha,\beta}\langle\psi_{i\alpha}|\psi_{j\beta}\rangle$$

where $\psi_{i\alpha}$ and $\psi_{j\beta}$ represent the atomic orbitals on atoms i and j, respectively. The total COHP, denoted as $\mathrm{COHP}_{ij}(E)$, is calculated as the sum of the Hamiltonian matrix elements and the overlap population, weighted by the density of states (DOS) at energy E:

$$\mathrm{COHP}_{ij}(E) = \sum_{\alpha,\beta} \sum_{\epsilon} N(\epsilon) H_{\alpha\beta} \langle \psi_{i\alpha} | \psi_{j\beta} \rangle$$

where $N(\epsilon)$ is the DOS at energy ϵ, and $H_{\alpha\beta}$ are the Hamiltonian matrix elements. These calculations are typically performed as post-processing steps on the electronic structure data obtained from DFT simulations. By analyzing the COHP curves, researchers gain insights into the nature and strength of chemical bonds in crystalline materials, aiding in materials design and optimization efforts.

As an illustration, the bonding and anti-bonding states of the previously mentioned TiS_2 were examined using COHP analysis, as shown in Figure 23. Upon reduction, the continuum associated with the anti-bonding states (blue) near the Fermi level broadens due to the delocalization of electrons in the empty Ti-*d* states. In the bonding continuum (red), which is primarily composed of S-*p* orbitals, the sharp peak disappears, indicating weakened bonding. This is likely due to a slight lengthening of the Ti–S bond during Li^+ intercalation, as evidenced by the DOS calculations (See Figure 22). These findings align well with the EELS data, suggesting that titanium is the primary redox site.

8.7 Molecular Dynamics

Molecular dynamics (MD)[208] is a computational tool used to study the dynamic behavior of atomic systems. Central to MD simulations is the representation of atomic interactions, encapsulated in the so-called potential energy surface (PES). In *ab initio* MD (AIMD), this PES is derived by solving the Schrödinger equation using either the Born-Oppenheimer[209] or the Car-Parrinello[210] method. Conversely, classical MD uses parameterized interatomic potentials (IAPs) to model these interactions. Traditionally, these IAPs are constructed based on mathematical functions fitted to either experimental data or *ab initio* calculations.[211]

The primary consideration between *ab initio* and classical MD is the balance between computational effort, accuracy and applicability. *Ab initio* MD offers high accuracy and

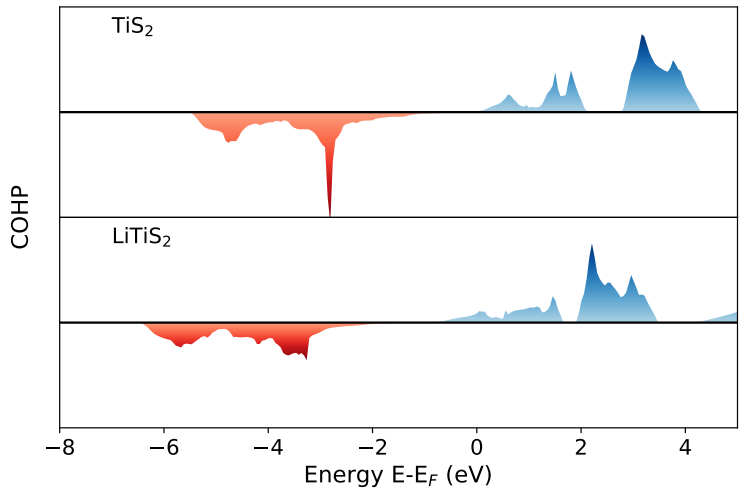

Figure 23: The Crystal Orbital Hamiltonian Population (COHP) analysis between a Ti-d orbital and a S-p orbital. The COHP values are depicted with negative values in red, representing bonding interactions, and positive values in blue, representing anti-bonding interactions. These values are plotted below and above the horizontal black line, respectively. The zero energy level is aligned with the top of the valence band. Reprinted from Ref.,[206] published under a CC BY license.

broad applicability across the periodic table, but its computational requirements and poor scalability (greater than $O(N^3)$) limit typical simulations to relatively small system sizes (less than 1000 atoms) and short time frames (about 100 picoseconds). In contrast, classical MD has been used for larger system sizes (up to millions of atoms) and longer time scales (more than 1 nanosecond). Nevertheless, the construction of a sufficiently accurate IAP tailored to a specific chemical context is a major challenge.

Recently, there has been a growing interest in using machine learning (ML) techniques to explore the connection between potential energy surfaces (PES) and descriptors of the local environment.[212,213] This approach shows promise as a comprehensive method for developing interatomic potentials (IAPs). In a typical workflow, known as ML-IAP fitting, a large data set of representative structures is first collected. These structures can be obtained from snapshots in AIMD simulations or carefully selected displacements from equilibrium structures, with their energies and forces calculated using DFT calculations. These sampled structures are then characterized using atomic descriptors that maintain strict invariances

with respect to translation, rotation and permutation of similar species. Examples of such descriptors include symmetry functions, moment tensors, bispectrum and smooth overlap of atomic positions. Finally, a machine learning model, such as linear regression,[214] Gaussian process regression[213] or neural networks,[212] is used to learn the relationship between the PES and the local environment descriptors. These ML-IAPs have demonstrated a remarkable ability to achieve energy and force predictions close to DFT accuracy, often surpassing traditional interatomic potential models, in a wide range of chemical systems.

Molecular dynamics (MD) simulations yield crucial insights into atomic behavior over time, enabling the derivation of various material properties. These include mobile ion diffusivity, conductivity, and others. For instance, jump diffusivity (D_J) can be derived from the slope of the mean square displacement (MSD) plot of mobile ion center of mass over time. Similarly, tracer diffusivity (D^*) can be obtained from the slope of individual mobile ion MSD averaged over time. Mobile ion conductivity σ and the Haven ratio H_r can then be calculated using the following equation:

$$\sigma = q^2 c \frac{D_J}{k_B T} = \frac{q^2 c}{H_r} \frac{D^*}{k_B T} \tag{38}$$

where c represents the number of mobile ions per unit volume, and the symbol q denotes the ion charge. Notably, due to the slow convergence of center of mass MSD, D_J calculations typically rely on classical MD simulations (or kinetic Monte Carlo), whereas D^* is more accessible through AIMD simulations, especially for fast ion conductors. Additionally, by conducting MD simulations at various temperatures, an Arrhenius plot of log(D) versus 1/T can be generated to determine the activation barrier (E_a) for diffusion. This allows for the extrapolation of diffusivities and conductivities at different temperatures. Moreover, MD simulations can analyze site occupancies at finite temperatures. For instance, investigating lithium occupancy at different Wyckoff positions involves analyzing lithium ion distribution and radial distribution function (RDF). Furthermore, MD simulations, particularly AIMD

which accurately describes bond formation and breaking, are utilized for modeling interfacial reactions.[215–217]

Molecular dynamic calculations have gained increasing importance, serving as essential tools to verify and complement analytical theories. The review by Mishin[218] highlights the significance of atomistic computer simulations in studying diffusion processes. Nowadays, simulation methods provide a robust means to gain fundamental insights into atomic jump processes[19] within materials, and their capabilities have significantly improved. Reliable potentials for atomic interactions have been established, enabling a quantitative description of point defect properties. The challenge lies in understanding, describing, and calculating diffusion coefficients in specific metals, alloys, or compounds.

De Blasio et al.[219] used an equivariant message-passing graph neural network model to accurately predict subatomic energies, forces and spin-resolved charge densities (see Figure 24). This model, which exhibits linear scaling, allows the analysis of extensive electronic-scale MD simulation data spanning hundreds of nanoseconds with an accuracy comparable to DFT. Their investigation focused on electron transfer coupled diffusion phenomena within a NASICON system of about 300 atoms observed on the nanosecond time scale. This allowed a comprehensive study of how changes in sodium concentration affect the diffusion behavior of Na-ions. They suggest that a coordinated ion exchange mechanism serves as the primary diffusion pathway, highlighting the ability of the model to capture intricate dynamics within the structure. Furthermore, by training a machine learning (ML) model on DFT-derived spin densities, they have explored variations in electronic densities surrounding vanadium ions during Na-ion migration. The results suggest a correlation between Na-ion migration and redox processes.

These findings represent a successful application of equivariant graph neural network-based surrogate models (in terms of energy, force and charge density) to investigate the electrochemical behavior of complex transition metal oxides and polyanions at the electronic scale. Significantly, the computational time required for ML calculations is several orders of

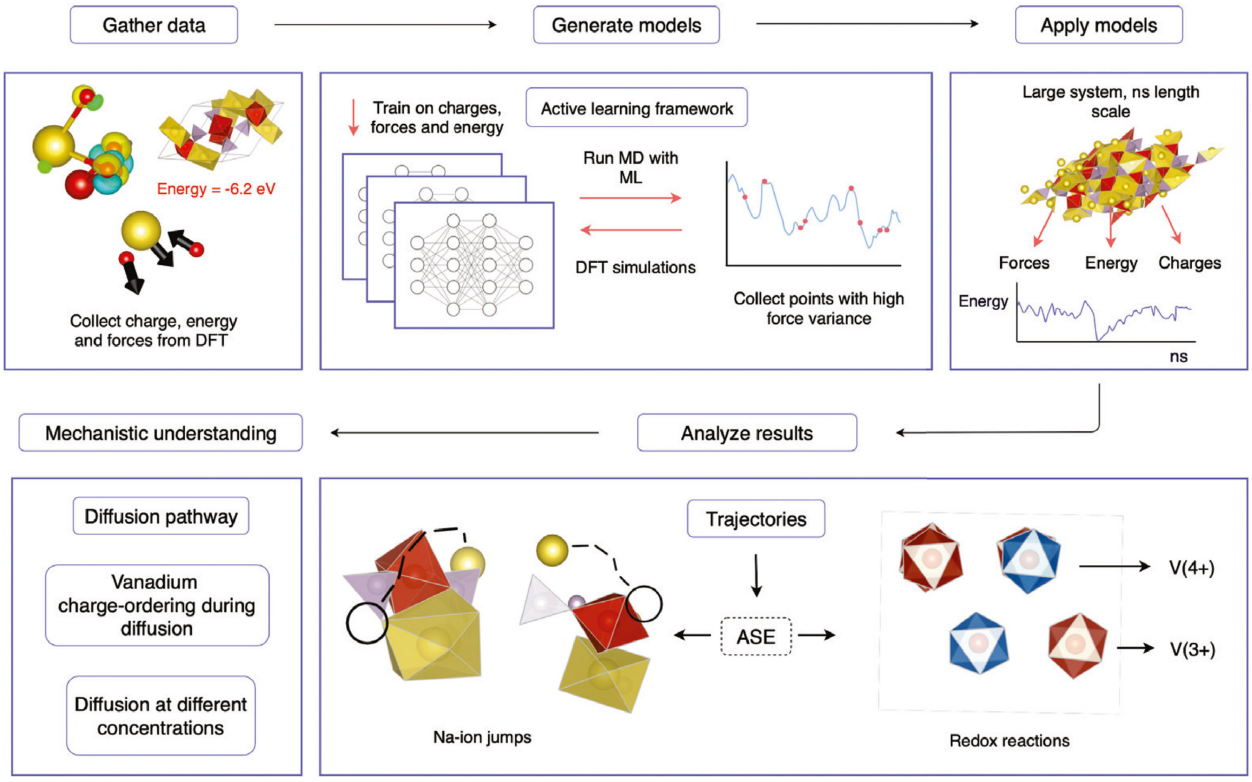

Figure 24: Schematic of the ML workflow. First, data on charges, forces and energies are collected from density functional theory (DFT) simulations. An ensemble of ML models is then trained to incorporate uncertainties in energy, forces and charge density. An active learning approach is then used to iteratively refine the models using new data that may fall outside the distribution, improving their accuracy and reliability. Finally, these models are capable of performing molecular dynamics (MD) simulations at the nanosecond scale, using a supercell of 300 atoms for our specific investigation. Subsequent analysis of the MD results will be carried out at different charge states and temperatures. Reprinted from Ref.,[219] with permission from Elsevier.

magnitude less than that of DFT, facilitating accurate analysis of large and complex systems on the nanosecond time scale. The methodology used in this study can be easily extended to different structural configurations and chemical compositions.

8.8 Force Fields Modeling

Atomistic simulations using force fields,[208] i.e., parameterized classical interaction potentials, are numerically very attractive and allow even millions of atoms to be taken into account. Unfortunately, they are not able to describe chemical reactions appropriately. A horizon-

tal multiscale technique, known as the QM/MM approach,[158] can be employed to combine quantum and classical molecular mechanics. This approach involves treating the central portion of the system, which requires a chemically accurate treatment, with quantum mechanics (QM), whereas the environment is treated with classical molecular mechanics (MM). This is a highly effective technique, but it is essential to ensure that the interface between the quantum and the classical region is accurately described.

Reactive force field (ReaxFF)[157] methods are capable of describing chemical reactions through the incorporation of bond-order terms. However, they are computationally much cheaper than quantum chemical calculations, and hence they offer a numerically attractive alternative. Nevertheless, their construction is very time-consuming and scales exponentially with the number of elements included in the ReaxFF. Typically, only up to three elements can be taken into account in a ReaxFF parameterization,[220] which limits their usefulness for battery simulations.

Similarly, traditional force fields can also be very helpful when structural information is to be obtained, for example, when the interfacial structure of SEI components in contact with the electrolyte are to be determined.[221] In recent times, numerical interpolation schemes for potential energy surfaces based on machine-learning techniques such as artificial neural networks have become increasingly popular.[212,222] Once such interaction potentials have been created, they enable the execution of numerically efficient atomistic simulations of complex structures and interfaces.[223]

8.9 Phase Field Modeling

Phase field modeling[161,224] has emerged as a powerful computational tool for investigating phase transitions and microstructural evolution in material systems. Its application to battery research[225,226] is promising, providing insights into the intricate dynamics of multiple phases within battery electrodes and electrolytes.

The phase-field approach[224] distinguishes between different physical states, referred to

as 'phases', by using variables $\phi = \{\phi_1, ..., \phi_\alpha, ..., \phi_N\}^T$ denoting volume fractions. These variables can represent different materials and phases, such as crystalline polymorphs or ordered states of the same material. The Allen-Cahn model in conjunction with a grand potential formulation[227] approximates the chemical free energy, denoted as $f_{\text{chem}}(\phi, x)$ by interpolating phase-dependent contributions. Specifically, the chemical free energy of each phase is represented by a fitting function, while the energetic barrier leading to a miscibility gap is introduced by an obstacle potential. This term serves as an additional phase mixing contribution, representing the activation energy required for phase transformation. For a two-phase interface this can be expressed as

$$f_{\alpha\beta} = \phi_\alpha f_\alpha(x^\alpha) + \phi_\beta f_\beta(x^\beta) + \Delta f_{\text{phmix},\alpha\beta} \tag{39}$$

where the phase mixing contribution is $\Delta f_{\text{phmix},\alpha\beta} = \frac{16}{\epsilon\pi^2}\gamma_{\alpha\beta}\phi_\alpha\phi_\beta$. More generally, the homogeneous free energy landscape is defined by

$$f_{\text{chem}} + f_{\text{ob}} = \sum_{\alpha}^{N} f_{\text{chem}}^{\alpha}(x^\alpha)\phi_\alpha + \frac{16}{\epsilon\pi^2}\sum_{\alpha,\beta>\alpha}^{N}\gamma_{\alpha\beta}\phi_\alpha\phi_\beta. \tag{40}$$

The fitting functions for the phase dependent chemical energies f_{chem}^{α} need to fulfill the invertibility criterion[228] such that the chemical potential can be expressed as a function of composition $\mu(x_\alpha)$.

The lattice constants of the intercalation host depend on both phase and concentration. The stiffness tensors obtained from density functional theory (DFT) calculations are directly integrated as input for multiphase field (MPF) simulations. These are based on the assumption of elastic deformations, with the occurring interfaces assumed to be coherent, characterized by an interfacial energy of about $\gamma_{\alpha\beta} \approx 0.1\,\text{J/m}^2$.

In battery systems, phase transitions occur during charge and discharge cycles, requiring a nuanced understanding of phase distribution and evolution within electrode materials. Phase field modeling allows researchers to predict and visualize these transitions under vary-

ing operating conditions, shedding light on the fundamental mechanisms governing battery performance. By simulating phase evolution, such as lithiation and delithiation in lithium-ion battery electrodes, phase field models facilitate the exploration of design parameters critical to optimizing battery performance. These parameters include particle size, morphology and electrode architecture, which have a profound effect on electrochemical kinetics and overall battery efficiency. In addition, phase field modeling helps elucidate degradation mechanisms, such as electrode cracking and electrolyte decomposition, which can degrade battery performance and safety over time. By simulating these processes, researchers can develop strategies to mitigate degradation and improve battery reliability and lifetime.

9 Ion transport

At the atomic scale, positively charged ions such as lithium (Li^+), sodium (Na^+) or magnesium (Mg^{2+}) exhibit movement within solids along specific migration pathways. These movements involve transitions between stable sites and transition states within a framework of negatively charged ions (e.g. oxygen (O^{2-}), sulphur (S^{2-}) or polyatomic anions). The properties of these sites, in particular their energy levels, are mainly determined by the local configuration of the ions, known as ion coordination. In crystalline compounds, this coordination typically manifests itself in tetrahedral or octahedral configurations.

Consequently, the trajectory of an ion through a material depends on the availability and connectivity of different sites dictated by the arrangement of negatively charged ions. Historically, crystalline structures with a body-centered cubic arrangement of anions have been commonly observed in highly efficient ion conductors such as α-AgI. Recent investigations by Wang et al.[229] suggest that this particular arrangement facilitates direct transitions between adjacent tetrahedral sites with minimal activation energy (E_a), obviating the need for high-energy tetrahedral-octahedral transitions. This body-centred cubic configuration is present in several fast ion conductors, such as $Li_{10}GeP_2S_{12}$ and $Li_7P_3S_{11}$, providing a valuable

framework for the design of novel materials with enhanced ionic conductivity.

Within crystalline structures, vacancies or positively charged interstitials are recognized as the mobile entities. There are three primary migration processes: (1) vacancy diffusion, where ions move towards nearby vacancies, (2) the direct interstitial mechanism, which occurs between partially occupied sites, and (3) the concerted or correlated interstitial mechanism, where a moving interstitial ion displaces a neighboring lattice ion to an adjacent position. The traversal of lattice atoms by the moving atom requires energy to overcome activation barriers along the migration path. Typically, the energy required to activate the jump exceeds the thermal energy $k_B T$.

At finite temperatures, atoms within a crystal oscillate in their equilibrium positions. These oscillations are often not strong enough to overcome barriers, so the atom returns to its original position. However, occasionally substantial displacements occur that allow the atom to successfully diffuse. These activation events are rare compared to the frequencies of lattice vibrations, which are characterized by the Debye frequency, typically between 10^{12} and 10^{13} s^{-1}. As soon as an atom moves due to an activation event, the energy dissipates rapidly. As a result, the atom is deactivated and undergoes, on average, many lattice vibrations before initiating another jump. In a crystal, atoms undergo thermally activated motion, moving between lattice sites (or interstitials) through a sequence of distinct jumps.

The concept of atomic migration across neighboring lattice sites was first proposed by Wert[230] and has since been significantly elaborated by Vineyard.[231] Vineyard approach is based on the canonical ensemble framework of statistical mechanics, which accounts for the statistical distribution of atomic coordinates and momenta. The mechanism of atomic displacement can be conceptualized as occurring within an energetically defined landscape characterized by the difference in Gibbs free energy (G^{migr}) between the transition state barrier and the equilibrium configuration. Here G^{migr} denotes the Gibbs free energy associated with the atomic migration (denoted by the superscript $migr$), which can be decomposed into

$$G^{migr} = H^{migr} - TS^{migr} \tag{41}$$

where H^{migr} represents the enthalpy associated with the migration, while S^{migr} represents the entropy associated with the migration. Using statistical thermodynamics, Vineyard[231] showed that the jump rate (ω), which is the number of jumps per unit time to a neighboring site, can be expressed as

$$\omega = \nu^0 \exp(-\frac{G^{migr}}{k_B T}) = \nu^0 \exp(\frac{S^{migr}}{k_B}) \exp(-\frac{H^{migr}}{k_B T}). \tag{42}$$

The parameter known as the attempt frequency, denoted as ν^0, is widely recognized as the Debye frequency and represents the rate of oscillation close to equilibrium along the reaction pathway. Here k_B is the Boltzmann constant and T is the absolute temperature. The entropy of migration reflects the change in lattice vibrations associated with the displacement of the jumping atom from its equilibrium position to the saddle point configuration. In the Vineyard method, the probability of reaching the transition state is derived by comparing the configurational partition functions of the initial and transition states, while the rate of crossing is determined by the unidirectional forward flux at the transition state. In the harmonic approximation, the expression for the migration entropy is thus formulated as

$$S^{migr} = k_B \left[\sum_{j=1}^{3N} \ln \left(\frac{h\nu_j}{k_B T} \right) - \sum_{j=1}^{3N-1} \ln \left(\frac{h\nu'_j}{k_B T} \right) \right]. \tag{43}$$

The frequencies ν_j represent the $3N$ normal modes for vibrations around the equilibrium site, while the $3N-1$ frequencies ν'_j correspond to the vibrations at the saddle point perpendicular to the jump direction with the constrained motion.

The macroscopic diffusivity can be derived from the energy barrier associated with individual diffusion events using transition state theory, also known as rate theory.[232] Assuming

that the energy of the system greatly exceeds the thermal energy ($h\nu \gg k_B T$), the effective frequency ($\nu^* = \nu^0 \exp(S^{migr}/k_B T)$) in the Arrhenius expression is determined by the ratio of the product of the $3N$ normal frequencies of the entire crystal at its initial configuration during a transition event to the product of the $3N-1$ normal frequencies of the crystal when it is constrained at a saddle point configuration:[231]

$$\omega = \frac{1}{2\pi} \frac{\prod_{j=1}^{3N} \nu_j}{\prod_{j=1}^{3N-1} \nu'_j} \exp\left(-\frac{H^{migr}}{k_B T}\right) = \nu^* \exp\left(-\frac{H^{migr}}{k_B T}\right). \tag{44}$$

At a macroscopic level, the movement of particles in a substance, known as diffusion, is governed by Fick's first law. This law states that the flux of particles ($\vec{J}$) is inversely proportional to the concentration gradient ($\vec{\nabla} c$) and is characterized by the diffusion coefficient (D):

$$\vec{J} = -D\vec{\nabla} c \tag{45}$$

Here, $\vec{J}$ represents the flux of particles passing through a given area per unit time, while D quantifies the rate of diffusion relative to the concentration gradient. Typically measured in square units of length per unit time (such as cm^2/s or m^2/s), the diffusion coefficient reflects the speed at which particles, like atoms or ions, disperse within a medium due to random thermal motion. It is crucial to differentiate chemical diffusion, driven by concentration gradients, from tracer or Einstein diffusion, which arises from thermal fluctuations. At low particle concentrations, chemical and tracer diffusion coefficients coincide.

Ionic conductivity is a measure of a material's ability to conduct electric current via the movement of charged ions. Ionic conductivity, or σ, is a particularly significant factor in electrolytes, where substances conduct electricity.σ is determined by the product of three

key factors: the mobile ion concentration (c), the ion charge (q), and the ion mobility (μ):

$$\sigma = qc\mu. \tag{46}$$

Typically measured in Siemens per meter (S/m), ionic conductivity distinctly describes the transmission of electric current through charged ion motion. While diffusion coefficient, at low particle densities, characterizes particle movement via random motion, ionic conductivity specifically refers to electric current conduction through charged ions.

The temperature dependence of ionic conductivity (σ) is described by:

$$\sigma = \frac{\sigma_0}{k_B T} \exp\left(-\frac{H^{migr}}{k_B T}\right) \approx \frac{\sigma_0}{k_B T} \exp\left(-\frac{E_a}{k_B T}\right) \tag{47}$$

Where σ_0 accounts for various factors including entropy of migration, jump distance, attempt frequency, and reaction mechanism. The activation energy barrier is represented by E_a. Additionally, in the case of non-interacting charge carriers, ionic conductivity can be expressed in terms of the diffusion coefficient (D) using the Nernst-Einstein relationship:

$$D = \frac{\sigma}{cq^2} H_r \, k_B T \tag{48}$$

Here, H_r denotes the Haven ratio, contingent upon the specific diffusion mechanism. It is noteworthy that the conventional Nernst-Einstein equation might not hold in the presence of particle correlations, requiring a more precise formula derived from linear response theory for accurate assessment of ionic conductivity.

Point defects within crystalline solids significantly influence material ionic conductivity. In 1926, Frenkel introduced the concept of point defects, proposing that thermal agitation leads to atom transitions, creating lattice vacancies. This phenomenon, known as Frenkel defect, encompasses the notions of vacancies and self-interstitials. Subsequent work by Wagner and Schottky expanded on this, considering disorder in binary compounds, including

vacancies, self-interstitials, and defects where atoms occupy incorrect lattice positions.

In defect-free crystals, lattice periodicity determines mass and charge density. However, the introduction of a point defect disrupts this pattern, impacting conductivity differently in metals and ionic crystals. While metals exhibit uncharged point defects due to electronic screening by conduction electrons, ionic crystals exhibit charged point defects to maintain charge neutrality. Frenkel and Schottky disorder models describe these defect distributions, crucial in materials like NaCl. In semiconductors, point defects introduce energy levels within the band gap, their charge states dependent on the Fermi level position.

9.1 Estimation of migration barriers

The activation energy (E_a) within solid materials can be determined by various experimental methods such as impedance spectroscopy, nuclear magnetic resonance (NMR). Alternatively, theoretical estimates of E_a can be derived using saddle-point search algorithms such as the nudged elastic band (NEB)[233,234] method (see Figure 25). In addition, E_a can be derived theoretically by extrapolation from molecular dynamics (MD) simulations performed over different temperature ranges as shown in Figure 25.

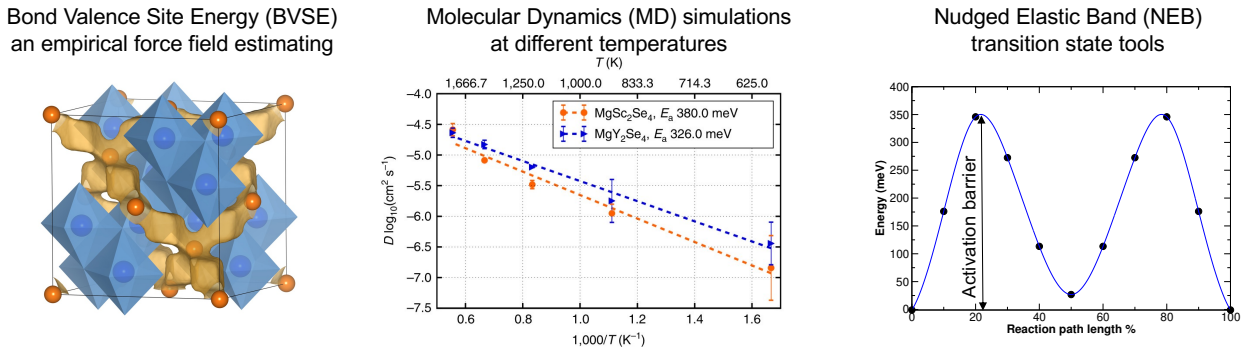

Figure 25: Computational simulations using Bond Valence Site Energy (BVSE), Ab Initio Molecular Dynamics (AIMD) and Nudged Elastic Band (NEB) techniques to elucidate the migration pathway and activation energy within the spinel crystalline framework. The AIMD is reprinted from Ref.,[235] published under a CC BY license.

The NEB approach calculates the minimum energy path (MEP) using an elastic band composed of geometric configurations, called "images", that approximate the MEP. Each

image corresponds to a unique configuration along the ion migration path. Initially, the band is relaxed to the MEP via a force projection mechanism. This mechanism involves the perpendicular force ($F^{\perp}$) due to potential energy and the parallel spring force ($F^{\parallel}$) acting on the band. The $F^{\parallel}$ ensures approximately equal spacing between the images, giving the band elastic properties and aiding in the accurate determination of the MEP profile. Convergence of the initial band to the MEP is achieved by minimizing the net force, F^{NEB}. Due to the straightforward calculation of forces in Density Functional Theory (DFT), the NEB method has been widely used in conjunction with DFT to calculate the activation energy (E_a) of ions in solids.

However, accurately predicting minimum energy paths is a time-consuming task as each frame within the band requires a separate Discrete Fourier Transform calculation. In addition, simply interpolating between the initial and final states may not provide an optimal starting band, potentially hindering the convergence of the nudged elastic band method. Rong et al. [236] introduced two strategies to speed up NEB calculations: first, the PathFinder algorithm, which exploits the tendency of ions to migrate within host structures while avoiding regions of significant electronic charge density changes or neighboring atoms/bonds; and second, the ApproxNEB approach, which estimates the energy of each frame using a less computationally intensive single-point DFT calculation. The combination of PathFinder (for approximate path determination) and ApproxNEB (for approximate energy calculation) allows the approximate prediction of activation energies (E_a). Another approach to approximate MEPs is the Bond Valence Site Energy (BVSE)[237] method, which is similar to an empirical force field that evaluates the energies surrounding different ionic sites (see Figure 25). This includes considering the coordination number, bond distances, and angles around the diffusion site. The BVSE utilizes the bond valence model to calculate the site energy of the diffusion site. The bond valence model relates the valence sum of the surrounding atoms to the bond length and provides an estimation of the site energy. Comparing the BVSE of the initial and final states of the diffusion process, shows the energy

difference between these states represents the energy barrier for ionic diffusion. Nishitani et al.[238] successfully applied BVSE to study the migration of Mg^{2+} in several host materials, accurately reproducing the barriers observed in costly DFT-NEB calculations. These inexpensive methods provide an alternative means of identifying efficient Mg conductors from large data sets. Note that the BVSE method is an empirical approach, and the accuracy of the calculated energy barriers may depend on the quality of the bond valence parameters and the assumptions made during the analysis.

9.2 NeuralNEB

DFT becomes too expensive when applied to large-scale exploration. Machine learning (ML) models have emerged as highly effective emulators of small molecule DFT calculations, potentially offering a replacement for DFT in such tasks. Accurately predicting the potential energy surface around transition states and minimal energy paths is crucial for successful kinetics studies. Unfortunately, the scarcity of relevant data in the literature has hindered this capability in the past. Schreiner et al.[239] trained equivariant graph neural network-based models using data from the Transition1x dataset, which consists of 10,000 elementary reactions. They employed these models as potentials for the nudged elastic band algorithm and achieved impressive results, with a mean average error of 0.23 eV and a root mean squared error of 0.52 eV on barrier energies for unseen reactions. To compare performance, they also trained equivalent models on QM9x and ANI1x datasets. Furthermore, their ML models outperformed Density Functional based Tight Binding in terms of both accuracy and computational resources required. These findings indicate that ML models have reached a level where they can be successfully applied to the study of chemical reaction kinetics, given an adequate amount of relevant data.

9.3 Pinball model

Kahle et al.[240] presented an effective model for characterizing the potential energy surface of lithium diffusion in a solid-state ionic conductor, assuming complete ionization of the Li atoms and disregard the minor influence of the electronic valence charge density on the instantaneous position of the Li ions. Then they immobilize the host lattice atoms at their equilibrium positions, thereby freezing the valence charge density as well. This configuration, known as the "pinball model", enables highly cost-effective molecular dynamics simulations. In the frozen lattice case, the charge density adjusts self-consistently to the actual positions of the diffusing Li ions. Their results demonstrate that the pinball model accurately reproduces the static and dynamic properties of the diffusing Li ions, including forces, power spectra, and diffusion coefficients, when compared to the self-consistent frozen-host lattice simulations. The frozen-lattice approximation itself often proves sufficiently accurate and serves as a reliable approximation in most materials. These findings provide efficient methods for simulating lithium diffusion in the solid state and offer further insights into the impact of charge-density rearrangements and lattice vibrations on lithium diffusion.

10 Scaling relations in crystalline materials

In the previous section, we focused on ion mobility within crystalline materials and identified factors that contribute to high ion mobility. However, for battery electrode materials, additional critical performance metrics such as energy density come into play. Specifically, cathodes must exhibit robust charge carrier binding, as this directly affects the open circuit voltage and hence the energy density.[241] Consequently, an optimal cathode should combine strong binding with low charge-carrier migration barriers.

In chemistry, however, Brønsted-Evans-Polanyi scaling relationships between reaction and activation energies are typically observed.[243,244] Such relationships extend to the insertion of atoms or ions into solid materials: higher binding energies of interstitials in host

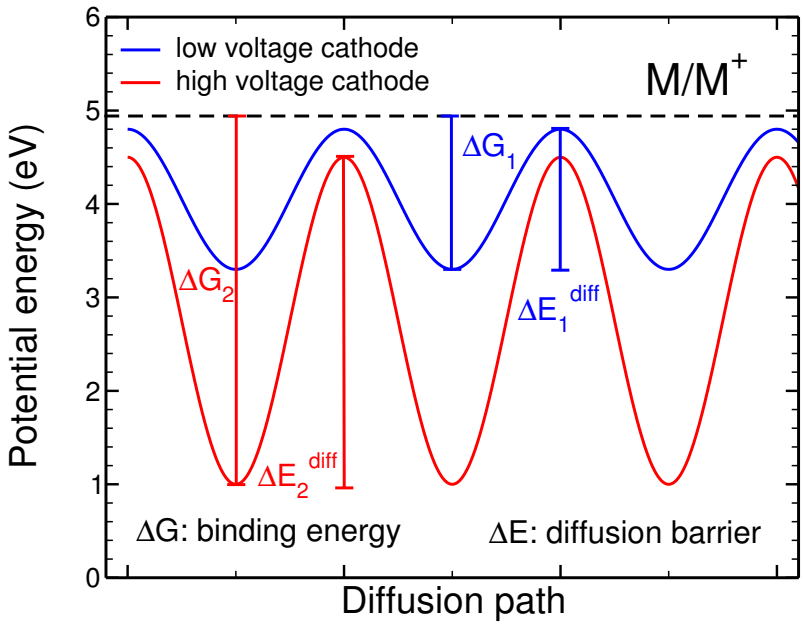

Figure 26: Illustration of the scaling relations between binding energies and diffusion barriers in the migration in crystalline materials: The larger the binding energies, the higher the diffusion barriers for the propagation from one minimum to the next. Reprinted from Ref. ,[242] published under a CC BY license.

materials correspond to larger diffusion barriers that hinder migration from one binding site to the next (see Figure 26). ΔG_1 represents the relatively low binding energy of a metal atom in a host material relative to the cohesive energy of the metal. Materials with a higher binding energy ΔG_2 typically have higher diffusion barriers ΔE_2^{diff} than materials with a lower binding energy. Consequently, a solid electrolyte should have low binding energies in order to have low diffusion barriers.

Such scaling relationships have recently been observed in spinel materials with respect to ion mobility.[245] For cathode materials in rocking chair batteries, high binding energies directly correspond to high open circuit voltages and thus high energy densities. However, according to these scaling relations, it is challenging to achieve high energy densities and fast ion mobilities with the same material. A trade-off between these properties must therefore be made, as breaking these scaling relations is necessary to combine high energy density with easy ion migration.

There are cases where such Brønsted-Evans-Polanyi type scaling relationships have been broken. For example, single-atom alloy (SAA) catalysts break the scaling relationships between high reactivity and strong binding of reaction products .[246] These catalysts typically consist of catalytically active elements atomically dispersed in an inert host metal.[247] While the reactive Pt atom lowers the barrier to hydrogen dissociation, the resulting atomic hydrogen fragments bind weakly to the Cu matrix.

Translating this concept to ion migration in crystalline solids is challenging. Typically, binding sites in solids correspond to highly coordinated configurations, such as six-fold coordination in octahedral sites or four-fold coordination in tetrahedral sites, while transition states exhibit lower coordination, such as three-fold coordination in spinel materials.[248] Doping the spinel material with a highly reactive atom can have a stronger effect on the low-coordinated transition state, where the distances are often smaller than at highly coordinated binding sites.

The influence of doping on the ion migration properties of solid electrolytes has been studied previously.[249,250] However, no general conclusive trends have been derived. Since doping is a stochastic process and migration involves overcoming numerous barriers, the coordination effect described above may not always apply. Nevertheless, breaking the scaling relationships between reaction energies and migration barriers may be highly advantageous and warrants the exploration of different approaches to achieve this. Alternative strategies have been proposed, including cointercalation, pillared structures, and anion redox. These will be examined in more detail below.

10.1 Dual Cation Co-Intercalation Strategy

Co-intercalation is a process whereby multiple ions are inserted into the host lattice simultaneously, which has the potential to disrupt the typical coordination environments and alter migration pathways. This has been proposed recently for the diffusion of Li, Na and Mg ions in the bulk phase of TiS_2.[206] They employed a multimodal approach merging experimen-

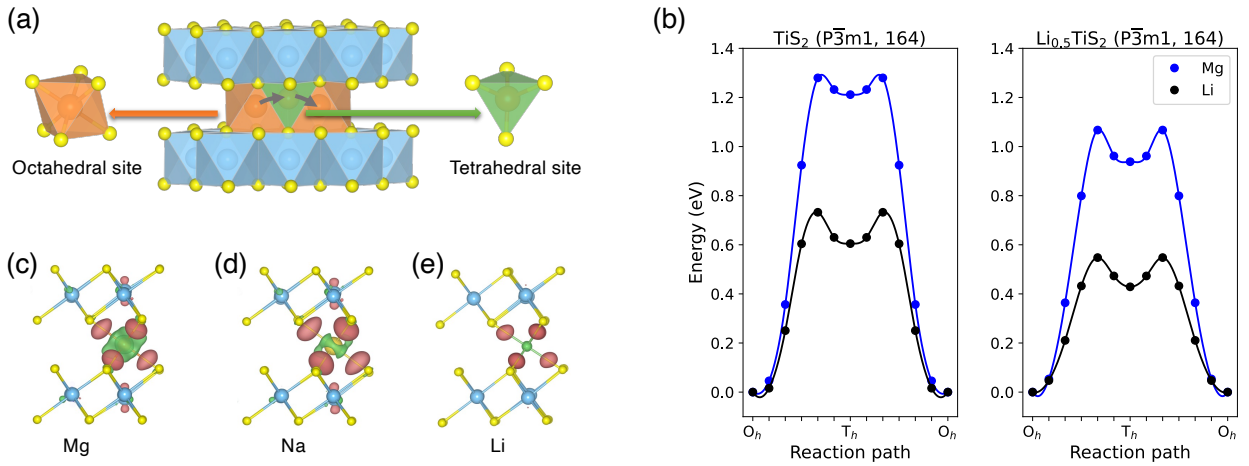

Figure 27: (a) The O1-TiS_2 crystal structure with Li and Mg atoms intercalated in octahedral (O_h) sites indicated by orange. The tetrahedral (T_h) site would serve as a metastable site during the hopping process in the diffusion channel between nearby O_h sites, which is indicated by green. (b) Li and Mg ions diffusion in bulk TiS_2 and $Li_{0.5}TiS_2$. Significant reductions in activation barriers are observed when Li fills 50% of interlayer sites. (c) A comparison of the spatial distribution of the difference in charge density with a Li, Na, and Mg atom in an O_h site. The brown and green isosurfaces represent the charge accumulation and depletion regions, respectively. Reprinted from Ref.,[206] published under a CC BY license.

tal and theoretical methodologies to elucidate the impact of the size of monovalent charge carriers (Li^+/Na^+) and the thermodynamic and structural stability of the host compound on the feasibility of cation co-intercalation. To evaluate the effect of monovalent ions on Mg ion reactivity, a comprehensive array of elemental, structural, and redox probes have been employed in conjunction with standard electrochemical techniques. Elemental analysis demonstrated the direct impact of monovalent ion size on the intercalation of divalent Mg ions. Structural characterization of cycled TiS_2, combined with density functional theory (DFT) investigations (Figure 27), highlighted the significance of thermodynamic and structural stability of the host compound for accommodating multiple cationic charge carriers reversibly. It is particularly noteworthy that phase transformation, especially in layered materials susceptible to phase change due to layer sliding, facilitates the co-intercalation of diverse carrier ions.

The migration process in TiS_2 is a direct hopping process from one O_h site, facilitated by

the T_h site. This process normally requires a significant amount of energy to overcome the barriers. Figure 27a provides a schematic representation of the diffusion path. The activation energies for lithium and magnesium ions are 0.60 and 1.28 eV, respectively. It appears that the charge rehybridization upon Mg insertion is higher than that of Li and Na. The divalent character of the Mg ion strongly encourages charge rehybridization (Figure 27c-e), which explains why Mg ions move slowly in layered TiS_2. However, the Mg-Li system did not undergo any phase change when O1-TiS_2 was co-intercalated with Mg and Li ions. The thermodynamic and structural stability of a variety of lithiated ternary Li_xTiS_2 compositions, along with interlayer expansion, enabled improved solid-state diffusion of Mg^{2+} with the migration barrier being reduced by more than 0.2 eV (Figure 27b). Conversely, TiS_2 underwent a phase change to a mixture of metastable P3 and O3 phases upon the first full discharge in the Mg-Na system. Despite the greater interlayer expansion, the metastability of the P3 phase and the unfavorable energetics of the prismatic site have prevented the co-intercalation of the smaller and densely charged Mg^{2+}. Indeed, calculations and experiments demonstrated that the incorporation of Mg^{2+} in P3 and O3 structures resulted in significant structural distortions, which provided insight into the rationale behind the low Mg diffusion.

10.2 Kinetics in Pillared V_2O_5

First-principles calculations within the framework of Density Functional Theory (DFT) were conducted to gain a deeper understanding of the thermodynamics and kinetics involved in the process of Li-ion intercalation in pillared V_2O_5. In the preliminary model construction, we adopted the crystal structure observed in V_2O_5-nH_2O.[251] This structure exhibits bilayers of V_2O_5 arranged in a stacking fashion along the *c*-axis within a monoclinic unit cell (space group C2/m). In contrast to the structured arrangement of individual layers observed in crystalline V_2O_5, this structure consists of stacked elongated ribbon-like structures composed of bilayers of individual V_2O_5 layers. The layers are composed of square pyramidal VO_5 units, as illustrated in Figure 28. The minimum distance between the bilayers is approximately 11.5

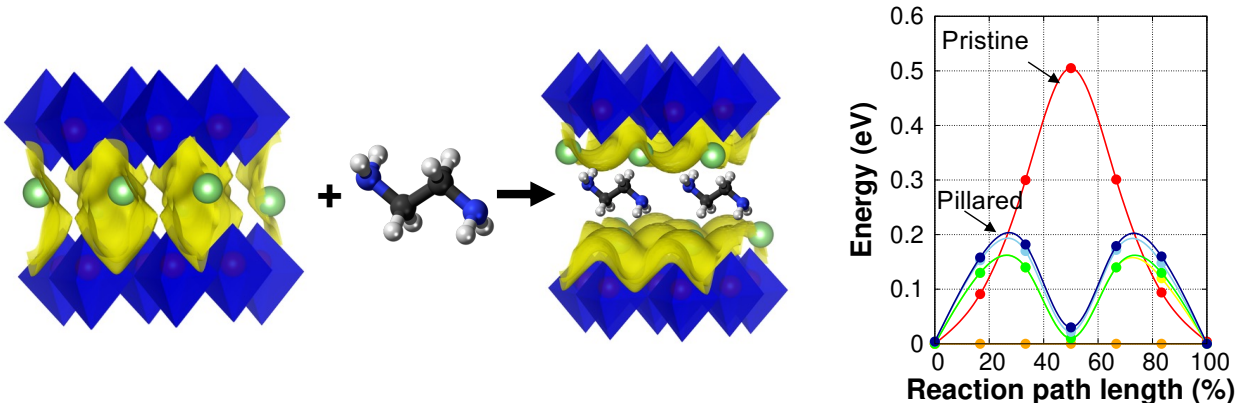

Figure 28: Simulated Bond Valence Site Energy (BVSE) profiles comparing the pristine compound with the compound following an increase in interlayer spacing. Green spheres represent lithium atoms, while blue octahedrons depict vanadium atoms coordinated by oxygen in an octahedral fashion. The yellow surfaces illustrate pathways for lithium-ion migration. The isovalue is set to 0.08 e/Å^3. Energy barriers (in eV) for Li^+ ion migration plotted against the reaction path coordinate, obtained via periodic DFT calculations in combination with nudged elastic band (NEB) method. The migration occurs between two pyramidal sites across the triangle face sharing tetrahedral site, under the low-concentration condition with a stoichiometry of $Li_{0.0625}V_2O_5$. NEB results illustrating the energy profiles for the pristine material (shown in red) and the material with increasing layer spacing of 13, 15, and 17 Å represented by dark blue, light blue, and green curves respectively.

Å, representing the most prominent repetitive pattern within the structure. This distance is subject to expansion or contraction as guest ions or molecules are incorporated into the framework.

The investigation starts by analyzing the characteristics of Li^+ ion migration pathways within LiV_2O_5, utilizing the Bond Valence Site Energy (BVSE) approach as shown in Figure 28. According to the static BVSE model, there are 1D pathways for Li sites. However, an increase in interlayer spacing facilitates the connection between channels, resulting in the formation of a 2D network of Li^+ ion paths. Interestingly, the migration pathways for the system with an increase in interlayer spacing illustrates interactions with oxygen in a non-equivalent manner, adhering predominantly to one side, thereby facilitating a diffusion process more akin to surface diffusion.

In LiV_2O_5, Li^+ ions occupy pyramidal sites surrounded by five oxygen atoms from neigh-

boring VO_6 octahedra in the upper and lower layers. When migrating between sites, the ions traverse triangular faces, requiring significant activation energy. Calculated activation energies (E_a) for Li^+ ions were 0.5 eV, decreasing to 0.2 eV with increasing layer spacing (Figure 28). These values allow the calculation of diffusion coefficients (D) at room temperature ($k_BT = 0.026$ eV) using the Arrhenius expression $D \sim \exp(-E_a/k_BT)$. The diffusion coefficient for Li ions at room temperature is 10^{-9} cm^2/s, and this value increases to 10^{-4} cm^2/s for larger layer spacings. The diffusion coefficient for Li ions in the pristine system is 10^5 times smaller than with increased layer spacing, indicating a significant mobility enhancement by opening the layer spacing. It should be noted that the migration barrier calculations were performed at 0 K.

This study also indicates that anion redox is not evident in V_2O_5. It can be concluded that V serves as the primary redox site for carrier intercalation. Furthermore, analyzing the voltages associated with these redox reactions provides deeper insight into their electrochemical characteristics. For V_2O_5, a calculated open circuit potential of 3.8 V, comparable with the system with expanding layer spacing of 3.4 V. This suggests that pillars could potentially offset this voltage decline, enhancing electrode performance.

10.3 Anion Redox

Anion redox plays a crucial role in the disruption of scaling relationships,[252] thereby expanding the potential applications of layered oxides to include both cation and anion redox for energy storage. Anion redox refers to redox processes involving undercoordinated anions such as oxygen, which are a common local feature in many compounds with excess lithium.[252] Theoretical predictions[253] suggest that this phenomenon occurs by extracting electrons from non-bonding p-like states (Figure 29a-c), known as orphan orbitals, resulting in a change in the formal valence of the affected oxygen ion from O^{2-} to O^{n-} (where $n < 2$). This process occurs within the crystal structure, although minor distortions such as shortening of the $O-O$ bond lengths between adjacent oxygen ions have been proposed. These distortions

can lead to the formation of 'dimers' through a reductive coupling mechanism (Figure 29d) where neighboring oxygen ions are also oxidized.[254,255] However, the resulting bond lengths are still significantly longer than the short bonds seen in molecular oxygen or peroxide and superoxide ions.

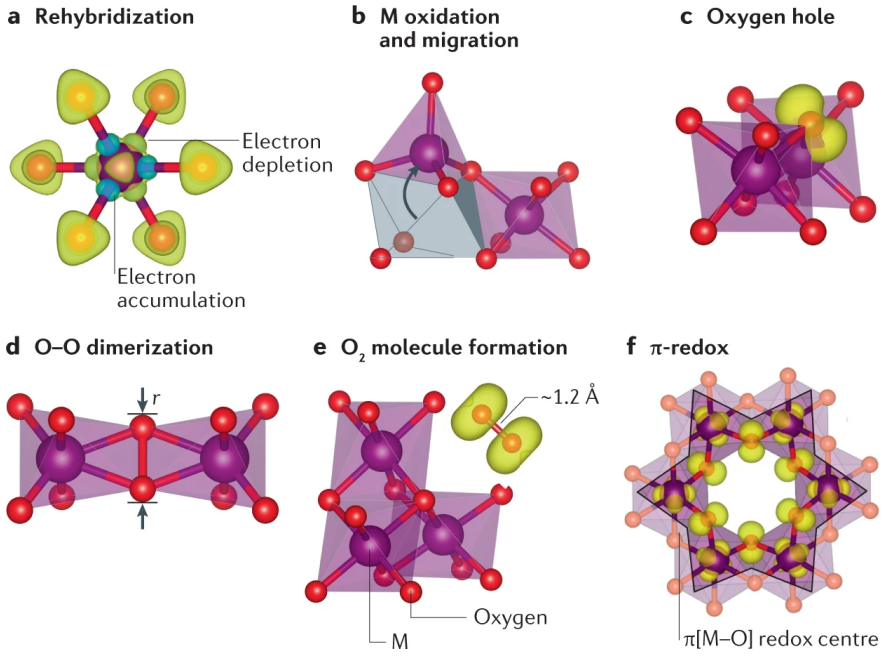

Figure 29: Distinct redox mechanisms. (a) When transition metals undergo redox reactions, there is typically a significant reconfiguration of electron distribution, particularly between the metal (M) and its coordinated oxygen atoms. Oxygen atoms are depicted in red, the transition metal in purple, and regions of electron density are illustrated with yellow and light blue contour plots.(b) Certain redox processes involving transition metals necessitate alterations in coordination, resulting in the migration of the transition metal.(c) Within lithium-excess materials containing undercoordinated oxygen atoms, vacancies can arise in the non-bonding orbitals of oxygen.(d) Anion redox reactions may induce structural distortions such as the formation of oxygen-oxygen dimers. The distance between dimerized oxygen atoms can range from greater than 2 Å to as short as observed in molecular O_2^{n-} species (approximately 1.2-1.6 Å).(e) Oxygen dimers have the capability to detach from the crystal lattice, either becoming confined within sub-nanometer-sized voids or migrating to the surface, where they irreversibly depart from the crystal structure.Reprintef from Ref.,[252] with permission from Springer Nature.

The molecular oxygen redox process involves oxygen ions and leads to specific structural changes and the formation of stable covalent bonds. During this mechanism, a pair of oxygen ions can either combine to form a dimer with short bond distances[256] (approximately 1.2-

1.6 Å) or separate from the crystal lattice to form molecular species such as O_2 or O_2^{n-}, which occupy confined regions within the crystal structure[257] (Figure 29e). Prior to the redox reaction, oxygen ions have a formal oxidation state of O^{2-}, which changes to O^0 in the formation of a neutral oxygen molecule or to O^{1-} in a peroxide molecule (O_2^{2-}). In addition, other molecular species such as O_2^- and O_2^{3-} are possible.[258] A critical aspect of the molecular oxygen redox mechanism is the formation of a short covalent bond between two oxygen ions in the 1.2-1.6 Å range, resulting in significant local changes in the crystal lattice, either through lattice distortion or cation migration.

The concept of delocalized π redox offers a novel perspective on the interplay between traditional transition metal redox reactions and lattice oxygen redox hypothesis.[259] This proposed mechanism suggests that non-bonding transition metal d orbitals interact with non-bonding oxygen p orbitals to form π bonds, resulting in an extended molecular orbital with redox activity (Figure 29f). Unlike conventional atomic oxidation states, the redox-active orbital is shared by several transition metal and oxygen atoms, forming a hybridized redox center over a larger molecular unit. This connectivity strongly influences the oxidation potential, stability and structural changes in the material. In particular, delocalized π redox relies on the presence of transition metal electrons, making it inaccessible to d^0 transition metal ions. While spectroscopic techniques can identify traditional transition metal and molecular oxygen redox reactions, the spectroscopic signatures of lattice oxygen redox and delocalized π redox mechanisms remain theoretical and require further investigation for definitive confirmation.

11 The Role of Covalent Interactions in Diffusion

To understand the dynamics of diffusion within crystalline structures, it is essential to look at the intricacies of the interactions that govern atomic stability and mobility. In this respect, an understanding of the interplay between covalent and ionic interactions is crucial.

Using periodic density functional theory (DFT) calculations, Sotoudeh et al.[260] studied the mobility of Mg ions in spinel chalcogenides, a class of materials with potential applications as cathodes in Mg ion batteries.[15] The research highlights the critical role that trigonal distortions play in spinel structures, affecting both Mg site preference and migration barriers. A remarkable correlation is observed with the choice of transition metals in these spinels: an increase in d band occupancy correlates with a decrease in lattice constants and an increase in trigonal distortions. These changes lead to increased migration barriers and consequently to a decrease in diffusivities. In addition, Bader charge analysis reveals a pronounced dominance of anionic redox in sulfide and selenide spinels compared to oxide counterparts upon Mg insertion into the lattice.

In many spinel structures studied so far, tetrahedral sites have shown greater stability to Mg insertion than octahedral sites. Interestingly, in Sc-based spinels, a reversal of this stability is observed at low Mg concentrations. Detailed analysis reveals that this variability in site preference arises from the interplay between coordination and bond length induced by trigonal distortions and absolute changes in bond distances, highlighting the significant role of covalent contributions to chemical interactions within spinels. These analyses highlight the inadequacy of a purely electrostatic interaction model to capture all factors influencing ion mobility and stability.

11.1 Electronegativity and bond enthalpy

The Pauling scale of electronegativity is a valuable tool for predicting bond enthalpies and evaluating bond polarities. Figure 30a shows the Van Arkel-Ketelaar triangle including the Mg binary compounds. A large difference in electronegativity indicates ionic bonding characteristics (shown in yellow), as present in MgO and MgF_2. CsF (not shown) would lie at the apex of the triangle. At the bottom of the triangle corresponding to a vanishing electronegativity difference, an increasing mean electronegativity is associated with more directional bonding. Hence the lower right corner gathers covalent systems whereas the

lower left corner contains metallic systems.

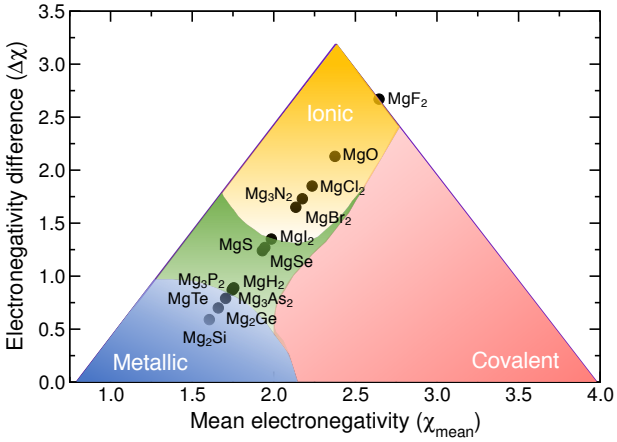

Figure 30: Van Arkel-Ketelaar triangle with the considered Mg_nX_m binaries plotted as a function of the mean electronegativity and the difference in the electronegativity of the two components. Reprinted from Ref. ,[261] published under a CC BY license.

The Mg_nX_m binaries all fall along a line between metallic and ionic bonding which is based on the fact that the cation in the binaries, Mg^{2+}, has not been varied. In detail, MgF_2 has the highest electronegativity difference $\Delta\chi$ indicating a strong ionic bond. This is also true for MgO, whereas Mg_2Si is associated with the lowest value $\Delta\chi$ demonstrating metallic bonding. The remaining compounds, Mg-halides, Mg-chalcogenides, Mg-pnictides, and Mg-tetrels, are located between strong ionic and metallic bonding indicated by the green area. They are divided into three groups. $MgCl_2$, $MgBr_2$, and Mg_3N_2 are characterized by a large electronegativity difference of about 1.7 demonstrating a predominately ionic bonding (light yellow region). MgI_2, MgS, and MgSe have $\Delta\chi \approx 1.3$, the other Mg binaries have electronegativity differences below 1.

The deviation from the purely ionic interaction can be characterized by the difference in the electronegativity $\Delta\chi^2$ of the interacting compounds which is also the basis for the Van Arkel-Ketelaar triangle. In this context it should be noted that the Pauling electronegativity in the form revised by Allred[262] that has been used here is based on a quite accurate, semi-

empirical formula for dissociation energies, namely

$$(\chi_{\mathrm{A}} - \chi_{\mathrm{B}})^2 = E_d(\mathrm{AB}) - \frac{E_d(\mathrm{AA}) + E_d(\mathrm{BB})}{2} \ . \tag{49}$$

This illustrates that the square of the difference in the electronegativities takes the deviation from a purely ionic interaction in a compound crystal into account. It is in fact true that the stronger polarizability of "soft" anions has already been used to explain the higher ion mobility in chalcogenides containing sulfur and selenide compared to oxides[263] with their softness reflected in the lower electronegativity of sulfur and selenide.[264,265]

12 Descriptors

12.1 Descriptors for ion mobility

Descriptors reflect correlations between the mechanisms that drive a particular property or function and a set of physically meaningful parameters. The determination of descriptors can considerably speed up the search for novel materials with desired functional or multi-functional properties because once they are identified, only the particular descriptor needs to be optimized in the first step. One of the most famous examples of descriptors is the correlation between the oxygen binding energy of a metallic catalyst and its reactivity in terms of the oxygen reduction reaction, following the Sabatier principle.[147] Descriptors have also been established in battery research. One example is the self-diffusion barrier of alkali and alkaline earth metals, which is correlated with the tendency of the corresponding metal anodes to exhibit dendrite growth.[66] With respect to the ion mobility in crystalline materials, there was the notion that still no common trends and mechanisms among different classes of ion conductors had been identified.[266]

Typically, the size and charge of the migrating atom have been considered as determining factors as shown in Figure 31, but they are not sufficient to capture a complete picture. The

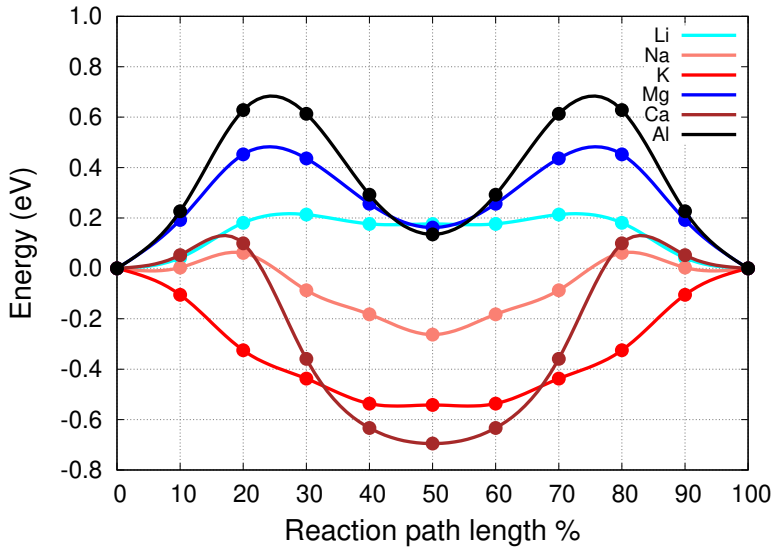

Figure 31: Charge carrier migration in the ACr_2S_4 spinel structure with A = Li, Na, K, Mg, Ca, and Al. The energies are taken relative to the energy of the charge carrier in the tetrahedral coordination. Reprinted from Ref.,[242] published under a CC BY license.

concepts of soft and hard ions have also been invoked, but not in a quantitative way.[235] Recently, these factors have been taken into account using the difference in electronegativity between the migrating cations and the counter anions of the host lattice.[261] As a descriptor for the height of migration barriers in crystalline materials, the so-called migration number was suggested:

$$N_{\mathrm{migr}}^{\mathrm{AX}} = (r_{\mathrm{A}} + r_{\mathrm{X}})\ n_{\mathrm{A}} n_{\mathrm{X}}\ \left(\chi_{\mathrm{A}} - \chi_{\mathrm{X}}\right)^2\ . \tag{50}$$

Here, A corresponds to the migration ion, X to the counter ion of the host lattice, r_{A} and n_{X} are their ionic radii, n_{A} and n_{X} the absolute values of the formal integer oxidation states, and χ_{A} and χ_{X} their electronegativities. By plotting calculated migration barriers as a function of this migration number, both for the variation of the migrating ion A and the counter ion X, linear scaling relations are observed.[261] This basically confirms the fact that in order to fully understand the migration mechanism, the deviation from a purely ionic interaction in a crystal structure must be taken into account.[260] Based on this descriptor and through computational analysis, a novel oxide spinel framework was characterized and predicted to

exhibit high Mg conductivity.[267]

Several additional features influencing ion mobility have been discussed in the literature, including lattice dynamics, phonon frequencies, and amplitudes.[19,268–270] The polarizability of atoms, categorized as a chemical feature, has also been suggested as a potential correlate to ion migration.[271] The crystalline lattice framework and structural features can play a role as well, with coordination geometries enhancing cation site stability and increasing migration barriers.[89] Low energy barriers are observed in structures adopting a body-centered cubic (bcc) anion sublattice, facilitating direct hopping between tetrahedral sites.[272] Larger cell volumes, reducing migration barriers by enlarging the migration channel, are also influential,[235] with larger, more polarizable anions contributing to this effect. Recently, a proposed structural feature promoting ionic conductivity involves corner-sharing connectivity in oxide crystal structures, attributed to distorted lithium environments and reduced interactions with non-lithium cations.[273] Through high-throughput computational screening, ten new oxide frameworks were discovered and experimentally validated in $LiGa(SeO_3)_2$, exhibiting notable ionic conductivity and activation energy of 0.17 eV.[273]

Screening the spinel structures for different charge carriers revealed that the migration number served as a viable descriptor as illustrated in Figure 32. However, for the lanthanide spinel compounds, the transition metal ionic radius was found to play a role in terms of stability and migration energy barriers.[274] The effect of lattice distortions due to atomic size mismatches is another important consideration, as it can reduce the barriers associated with certain ion migration pathways.[275] Furthermore, solids characterized by lower densities, such as high-temperature polymorphs and glasses, have demonstrated enhanced ionic conductivity due to 'paddlewheel' dynamics.[276,277] Therefore, identifying a suitable descriptor is a daunting task due to the complex nature of migration reactions involving different diffusion mechanisms and pathways, highlighting the need for classification methods, such as categorization based on mobile ions or lattice structures.

Machine learning (ML) provides a means to achieve these goals by identifying complex

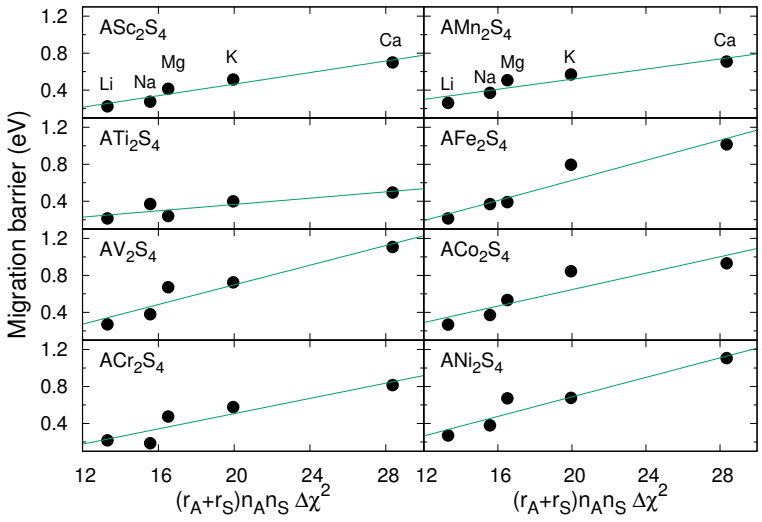

Figure 32: Migration barriers obtained from DFT-NEB calculations versus migration number N_{migr} for AB_2S_4 spinel compounds with eight different transition metals B = Sc, Ti, V, Cr, Mn, Fe, Co, Ni and upon variation of migrating cations A = Mg, Na, K, Mg, Ca. Reprinted from Ref. ,[261] published under a CC BY license.

relationships between different features and a particular property. Recently Kim et al.[278] utilized ML to identify critical chemical and structural features that affect ion mobility in anti-perovskite lattice-based solid-state batteries, highlighting properties such as hopping distance and channel width. In another investigation, López et al.[279] utilized first-principles materials simulations and data analysis techniques to uncover that correlations between ion diffusivity and materials descriptors are most pronounced when linked to vibrational nature with anharmonic effects. Interestingly, elastic and vibrational descriptors, rather than conventional ones like chemical composition and ion mobility, prove to be more effective in categorizing solid-state electrolytes into universal groups. This highlights the significance of considering temperature effects in databases for an enhanced understanding and a generalized approach to energy material design. Optimizing these descriptors for ion mobility in energy storage materials is essential. A classification approach centered on the migration mechanism emerges as an appropriate strategy and by tailoring structural, electrochemical and transport properties, researchers can design materials with high ion mobility.

12.2 Dendrite Growth

The occurrence of dendritic growth[23,43,280] represents a significant challenge, particularly in the anodic region of lithium-ion batteries. Dendrites, schematically depicted in Figure 33, are needle- or bush-shaped structures formed during lithium deposition at the anode. They pose risks such as irreversible battery damage and potential hazards such as fire. When dendrites bridge the anode and cathode, short circuits occur, generating intense heat that can ignite the flammable electrolyte, leading to battery fires. It is important to note that dendrite formation is not exclusive to anodes containing metallic lithium; it also occurs under conditions of high charge rates or low temperatures.[281] Even in the absence of short circuits, dendrite formation degrades battery performance by reducing cyclability, depleting anode material and contaminating the electrolyte.

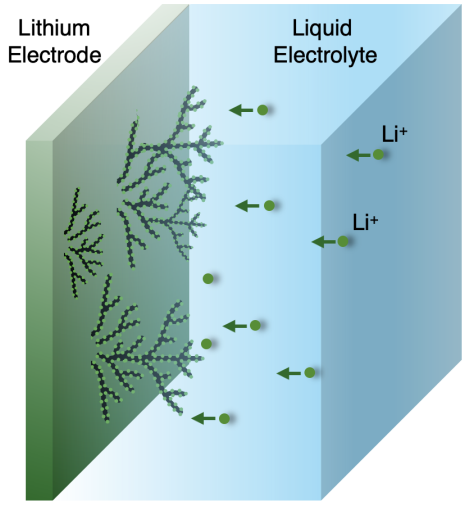

Figure 33: Schematic sketch of dendrite growth in Li-metal battery.

A number of theories have been put forth, including the influence of irregularities in the surface charge caused by imperfections in the solid electrolyte interface (SEI) and preferential growth from existing surface protrusions.[282] Molecular simulations using coarse-grained models have demonstrated that the propensity for dendrite formation increases with electrode overpotential.[283]

It is noteworthy that not all charge carriers within metallic structures exhibit identical tendencies towards dendrite formation. Studies have demonstrated that magnesium, in contrast to lithium, does not aggregate on copper or gold substrates but rather develops uniform structures.[284] This characteristic renders magnesium a promising alternative to lithium in battery applications,[103] given its higher volumetric energy density, which is facilitated by its ability to carry two elementary charge units. Furthermore, magnesium represents a more sustainable solution, being more abundant in the earth's crust, which also enhances its economic attractiveness.

It is crucial to acknowledge that existing theories on dendrite growth are often not specific to particular elements but rather generic regarding the metal's properties involved in dendrite formation. Consequently, these models are unable to account for the disparate behaviors observed in magnesium and lithium in the context of dendrite growth. An understanding of growth phenomena at interfaces is closely tied to the diffusion coefficients (D) and deposition flux (F).[285] It is of note that the ratio D/F represents a critical factor in the theory of nucleation.[286] Consequently, an increase in the deposition flux has an analogous effect to a reduction in diffusivity. The observation that dendrite growth tends to occur at high charge rates and/or low operating temperatures is consistent with this understanding, as charge rate directly influences deposition flux, while temperature governs diffusion coefficients.

In order to gain insight into the differing behaviors of Mg and Li in relation to dendrite growth, periodic Density Functional Theory (DFT) calculations were conducted.[66] Their findings indicate that on Li(001), the hopping mechanism remains marginally more favorable than the exchange mechanism. However, the most significant observation is the markedly smaller self-diffusion barrier of 20 meV on Mg(0001) in comparison to Li(001) and Na(001). The low diffusion barrier endows deposited Mg atoms with high mobility, facilitating their smooth propagation on the surface until they attach to island edges, resulting in a more efficient growth mode. Conversely, higher diffusion barriers result in deposited adatoms remaining stationary, which in turn leads to a rougher growth mode. Furthermore, they

consider diffusion barriers that are relevant for three-dimensional growth, such as barriers for diffusion across steps. Their findings align with experimental observations, indicating that Li dendrite growth is an inherent property of the metal. However, these calculations have overlooked the influence of the battery's operational environment. It is important to note that the presence of electrolytes and the solid-electrolyte interphase (SEI) can significantly alter the diffusion properties. Furthermore, the electrode potentials during charging and discharging cycles have not been considered. It is therefore essential to consider these factors in order to gain a comprehensive understanding of dendrite formation in batteries.

13 Electrochemical stability

The effective use of electrolytes depends on both their ionic conductivity and their stability under different conditions. In particular, they must be able to withstand thermal decomposition and reactions with surrounding substances. In addition, their use should prioritize ionic conduction over electronic conduction, ensuring that they operate within their stability ranges.[139] In other words, an electrolyte must withstand the reducing conditions of the negative electrode and the oxidizing conditions of the positive electrode. The term "stability window" was coined some years ago to describe the potential range within which an electrolyte remains useful.

Although kinetic considerations may be important in some cases, stability window is primarily a question of thermodynamics.[287] This is particularly relevant in the case of negative potentials due to the widespread use of highly reactive substances such as alkali metals or their alloys as negative electrode components in various modern systems.

When the potential of an electrode falls outside the stability range of the electrolyte, a reaction occurs at the electrode/electrolyte interface. This phenomenon can occur on either or both electrodes. For example, if two chemically inert electrodes, such as platinum wires, are immersed in a basic aqueous electrolyte solution and the voltage between them

exceeds the threshold corresponding to the standard Gibbs free energy for water formation (approximately 1.23 V at room temperature), electrolysis will occur. In this process, the electrolyte becomes unstable, resulting in the evolution of hydrogen gas at the negative electrode and oxygen gas at the positive electrode.

13.1 Binary Electrolyte Phases

If the electrolyte is a binary phase containing an alkali metal, the determination of stability becomes straightforward with knowledge of the phase diagram and relevant thermodynamic data.[274] The stability range is defined by the voltages at which charge carrier (e.g. Mg-ion) is extracted from the electrolyte, leading to the formation of an Mg-deficient decomposition layer between the solid electrolyte and the cathode. Conversely, the insertion of magnesium into the electrolyte results in the formation of the Mg-reduced decomposition layer.In the Mg binaries, below 0 V vs. Mg/Mg^{2+}, metallic Mg is the stable form. Above 0 V, the binaries consisting of oxidized Mg together with the anions are stable up to a voltage that corresponds to the formation energy ΔG_f^0, of the binaries,

$$\Delta V = -(\Delta G_f^0 / zF) \ , \tag{51}$$

where F is the Faraday constant and z corresponds to the elementary charges that are transferred upon the discharging reaction with $z = 2$ for Mg batteries. At higher voltages, magnesium is extracted, providing the oxidized cations.It is important to mention that the potential implications of exposing the solid electrolytes to the high magnesium potentials have been investigated without accounting for additional reactions between the electrolyte and the anode or cathode materials.

The electrochemical stability windows of the binary compounds in comparison to Mg/Mg^{2+} are presented in Figure 34, which was calculated according to Eq. 51. For binary compounds, the Mg-triels and Mg-tetrels exhibit poor stability, as evidenced by the narrow stability win-

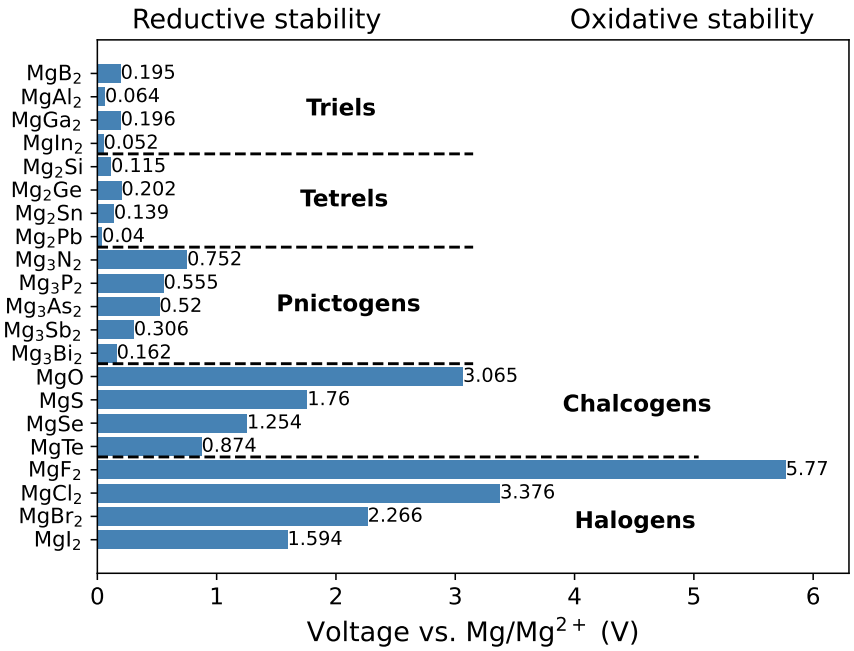

Figure 34: Electrochemical stability windows of Mg binaries indicating the voltages vs. Mg metal that the binaries are stable and not decomposed. Compounds are listed through the anions group in the periodic table. Reprinted from Ref.,[274] with permission from American Chemical Society.

dow and consequently low oxidation resistance. Mg-pnictogens are associated with a larger stability window. For instance, Mg_3N_2 is stable over a range of 0 to 0.75 V at room temperature. Nevertheless, the widths of the stability windows remain relatively narrow, with a range of less than 1.0 V. In contrast, all of the Mg-halogens and Mg-chalcogens are notably more stable over a broader range of potentials at room temperature. It is noteworthy that the oxidative stabilities exhibit a strong correlation with the anion electronegativities. For a strongly electronegative anion, such as fluorine, the corresponding binary compound, MgF_2 is stable against Mg up to potentials of more than 5.0 V. Consequently, among all the considered binary compounds, the Mg chalcogenides and halides exhibit the highest stability. A similar approach based on the grand potential has been employed in a recent computational study of binary materials in Mg batteries.[288] It should be noted that the solid electrolytes often have a lower energy range over which they are stable compared to liquids.[287]

13.2 Ternary Electrolyte Phases

The stability of electrolytes comprising of more than two components is more complicated. To illustrate the principles and methodology, let us consider a hypothetical ternary system comprising components Mg, a second metal denoted as Sc, and Sulfur (S). Ternary Mg-Sc-S phase diagrams are constructed for each spinel compounds utilizing a library of DFT computed bulk energies of materials with crystal structure from the Materials Project database,[199] as shown in Figure 35. Only two binary sulfides of Sc, nominally ScS and Sc_2S_3 are stable and no phases exist between Mg and Sc, and that only one ternary phase exists, $MgSc_2S_4$. The thermodynamic parameters of the triangle $MgSc_2S_4$-MgS-ScS in Figure 35 will determine its limits of stability in the low-potential magnesium-rich direction, and those in the triangle $MgSc_2S_4$-Sc_2S_3-ScS will determine its limit of stability in the high-potential magnesium-poor direction, in the case of the possible solid electrolyte phase $MgSc_2S_4$. Therefore, for these ternary spinels, the lower limit of the stability window has been obtained using the relevant Mg decomposition reaction between the solid electrolyte and the anode

$$\mathrm{Mg} + \mathrm{MgSc_2S_4} \rightarrow 2\mathrm{MgS} + 2\mathrm{ScS}, \tag{52}$$

and the minimum voltage vs. magnesium is determined from

$$V = -(\Delta G_r^0 / zF), \tag{53}$$

where

$$\Delta G_r^0 = \Delta G_f^0(products) - \Delta G_f^0(reactants). \tag{54}$$

Likewise, the maximum potential up to which this phase remains stable is determined

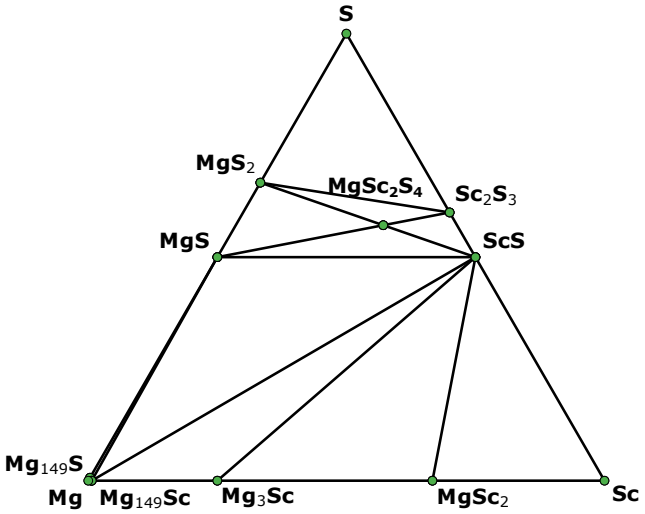

Figure 35: A ternary phase diagram illustrates the Mg–Sc–S system, indicating stable crystalline phases determined by energy calculations relative to the hull. Labels and points denote these phases, while lines represent reaction vectors, indicating changes in elemental concentrations for the stable phases.Reprinted from Ref.,[274] with permission from American Chemical Society.

by the Mg spinel decomposition reaction involving the solid electrolyte and the cathode

$$2\mathrm{ScS} + \mathrm{MgSc_2S_4} \rightarrow \mathrm{Mg} + 2\mathrm{Sc_2S_3}, \tag{55}$$

This can be converted to a voltage vs. magnesium by using Eqs. 53 and 54. Note that we determined the stabilities of all considered solid electrolytes for a temperature of 0 K.

To propose suitable and practical materials for the electrolyte phase is the assessment of stability limits in the low-potential magnesium-rich and high-potential magnesium-poor directions. For this purpose, the electrolyte stability windows of the ternary spinel phases have been determined using the Gibbs free energy of the phases according to Eq. 53 and 54, as shown in Figure 36. The reductive stability reactions are determined by the triangle MgM_2O_4-MgS-MS, whereas the oxidative stability is calculated using the metal sulfide phases MgM_2O_4-M_2S_3-MS. According to Figure 36, all calculated stability windows are smaller than

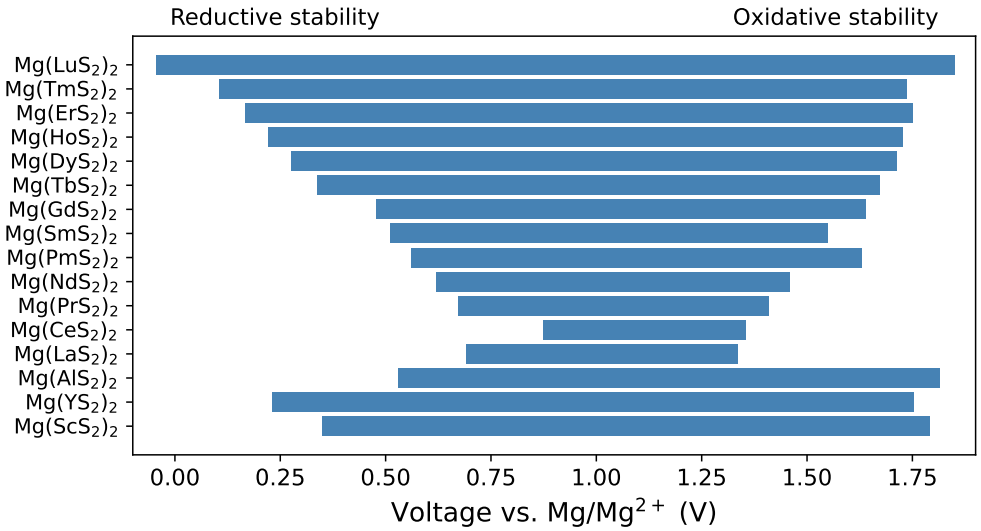

Figure 36: The electrochemical stability windows of the MgM_2S_4 compounds were determined as a function of the voltages vs. Mg metal. Reprinted from Ref.,[274] with permission from American Chemical Society.

1.8 V. Among the considered candidates, those sulfide spinels with large ionic radii of the M-cation (La, Ce, Pr, Nd, Pm, and Sm) display narrow stability windows due to the instability against Mg metal. The largest stability windows are found for the metals Lu, Y, and Sc.

The objective of this analysis was to assess potential solid electrolytes or coatings to be used in electrochemical cells. Among the binary compounds, magnesium bromide ($MgBr_2$), magnesium iodide (MgI_2), and magnesium chloride ($MgCl_2$) demonstrated favorable stability against the highly reducing magnesium metal anode, along with acceptable magnesium ion mobility. With regard to the spinel compounds, the ionic radius of the transition metals was identified as a pivotal factor influencing stability. While all compounds exhibited sufficiently low barriers for magnesium migration, only magnesium lutetium sulfide ($MgLu_2S_4$), magnesium yttrium sulfide (MgY_2S_4), and magnesium scandium sulfide ($MgSc_2S_4$) demonstrated electrochemical stability over a voltage range of approximately 2 V. These findings are expected to provide valuable guidance for the development of rapid magnesium-conducting solid materials with enhanced properties.

This methodology has been applied to calculated stability windows of LiCl, LiF, Li_2ZrCl_6,

and Li_2ZrF_6 as a function of Li^+/Li.[289] The electrochemical stability of LiF is found to be the highest in the range of 0–6.4 V, with a zero reduction potential versus lithium. Similarly, LiCl is stable up to 5.1 V with a zero reduction potential. The Li_2ZrCl_6 exhibits a limited electrochemical stability window of only 1.89–4.57 V. In contrast, the fully fluorinated counterpart (Li_2ZrF_6) exhibits a substantially broader stability window, spanning 1.24–6.53 V. This suggests that a partial substitution of chlorine by fluorine will also result in an extension of the stability window, which is in agreement with the experimental findings.[289]

13.3 Compatibility with alkaline metal anodes

In solid-state batteries[16–18] another critical challenge is to effectively combine solid-state electrolytes with highly reactive alkali metal anodes. It is imperative to establish compatible interfaces between these anodes and electrolytes to protect against gradual electrolyte material degradation. Recent advances[290] have identified a protective hydrate compound ($Na_3SbS_4.8H_2O$) by computational methods for the solid state electrolyte Na_3SbS_4, which was subsequently confirmed experimentally as a reliable electrolyte-anode interface for sodium metal batteries (Figure 37). First-principles calculations were used to screen potential passivating materials stable in interaction with sodium metal, with NaH and Na_2O emerging as promising candidates. In addition, NEB calculations were used to evaluate the migration energies of sodium vacancies within hydrates, with $Na_3SbS_4.8H_2O$ emerging as a favorable sodium-ion conductor due to lower migration barriers. Experimentally, a hydrate layer was synthesized by exposing Na_3SbS_4 to ambient air, resulting in the formation of $Na_3SbS_4.8H_2O$. This hydrated phase partially reacts with sodium metal to produce NaH and Na_2O as passivating materials, as confirmed by spatially resolved synchrotron x-ray diffraction. Symmetric cells ($Na//Na_3SbS_4//Na$) were assembled using custom pressure cells to evaluate sodium plating and stripping performance under air-exposed and pristine conditions at 0.1 mA cm^{-2}. Consistent with theoretical predictions, the air-exposed scenario exhibited lower and more consistent plating and stripping overpotentials over a 25

hour period, whereas the pristine case exhibited steadily increasing polarization.

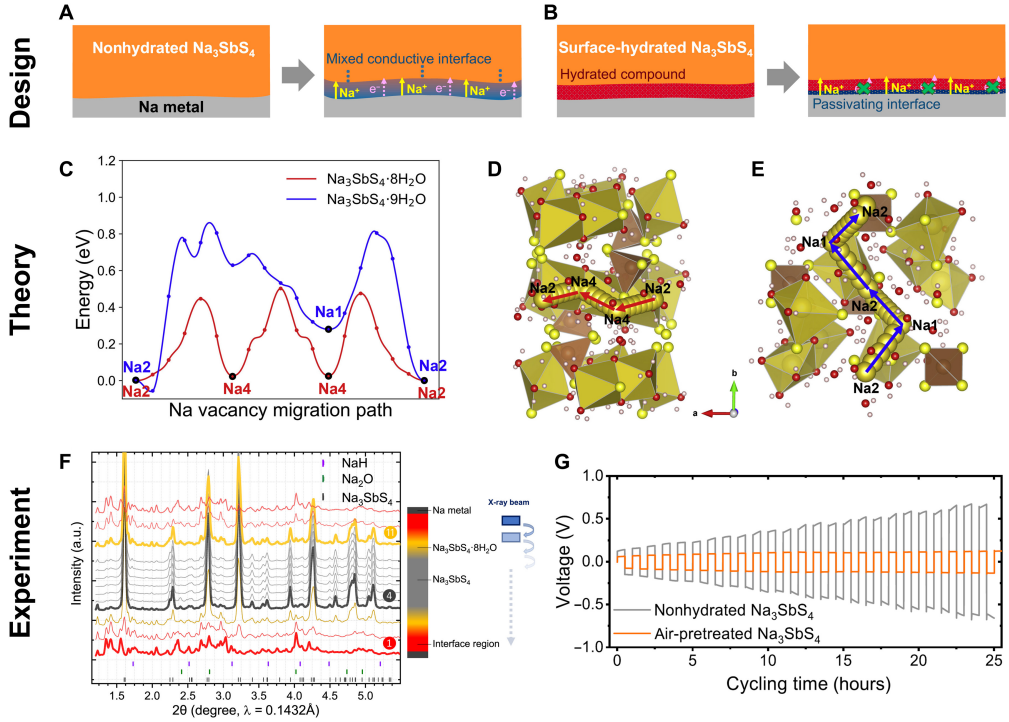

Figure 37: Improving the stability of the interface between a sodium (Na) anode and the solid-state electrolyte Na_3SbS_4 through surface hydration. (A and B) Illustration depicting the interface between the electrolyte and Na metal: one for the non-hydrated Na_3SbS_4 solid electrolyte showing the formation of a mixed conductive layer after cycling, and the other for the surface-hydrated Na_3SbS_4 electrolyte demonstrating the formation of a protective interface. (C) Calculations of the migration energies of sodium vacancies along optimal paths using nudged elastic band calculations for surface-hydrated Na_3SbS_4 electrolytes: $Na_3SbS_4.8H_2O$ and $Na_3SbS_4.9H_2O$. (D and E) Schematics showing the migration pathways of sodium vacancies with minimal barriers in $Na_3SbS_4.8H_2O$ along the [100] direction (D) and in $Na_3SbS_4.9H_2O$ along the [010] direction (E). $Na(H_2O,S)_6$ octahedra and SbS_4 tetrahedra are colored yellow and brown, respectively. (F) Experimental confirmation of the regions with hydrated interfaces in a $Na/Na_3SbS_4/Na$ symmetric cell through spatially resolved post-operando synchrotron x-ray diffractogram. The bolded red, gray, and yellow spectra correspond to the interface region, solid electrolyte, and the hydrated $Na_3SbS_4.8H_2O$, respectively. (G) Galvanostatic cycling of $Na/Na_3SbS_4/Na$ symmetric cells at a current density of 0.1 mA cm^{-2}, showing increasing potentials for cells without surface hydration pretreatment (gray). Figures adapted from Ref.,[290] with permission from Elsevier.

We propose future avenues for the application of analogous theory-experiment frameworks. These include developments in battery technology that utilize multivalent ions, such as magnesium and aluminium. Furthermore, an examination of the formation of the bat-

tery interface and its evolution under cycling conditions can yield valuable insights, which can in turn inform high-throughput computations and machine learning algorithms for the advancement of next-generation energy storage systems.

14 Theory-guided experimental design

Current research into emerging battery technologies still relies heavily on the Edisonian trial-and-error methodology. These investigations typically follow a sequential process of material synthesis, electrode and electrolyte fabrication, and subsequent cell assembly and testing. It has been estimated that there are over 10^{100} permutations in the selection of active materials and electrolytes alone.[291] As improvements in cell performance are observed, additional simulation work may be undertaken to uncover the underlying relationships between structure and properties within a given chemical space. This raises two important questions: Can theoretical frameworks be used more effectively to design experiments, thereby reducing the time and resources required? And if so, how can we develop a workflow that seamlessly integrates theoretical modeling and experimental work?

The synergy between theoretical modeling and practical experimentation is proving to be crucial in the pursuit of advancing battery technology[292,293] (see Figure 38. This integration accelerates scientific and technological progress in the field of batteries. Rather than relying solely on trial-and-error methods, theoretical calculations play a key role in guiding experimental design. For example, the use of first-principles calculations enables rapid screening of vast chemical spaces to predict potential battery materials.[273] These predictions are then validated by careful experimental testing, forming a continuous feedback loop. Theoretical calculations also help elucidate intricate battery phenomena, such as ion diffusion mechanisms and electronic structure effects, that are otherwise elusive by empirical means alone. Furthermore, a structural feature has been identified[273] that promotes ionic conductivity. This involves corner-sharing connectivity in oxide crystal structures, which is attributed to

distorted lithium environments and reduced interactions with non-lithium cations. Through high-throughput computational screening, ten new oxide frameworks were discovered and experimentally validated in $LiGa(SeO_3)_2$, exhibiting notable ionic conductivity with an activation energy of 0.17 eV.

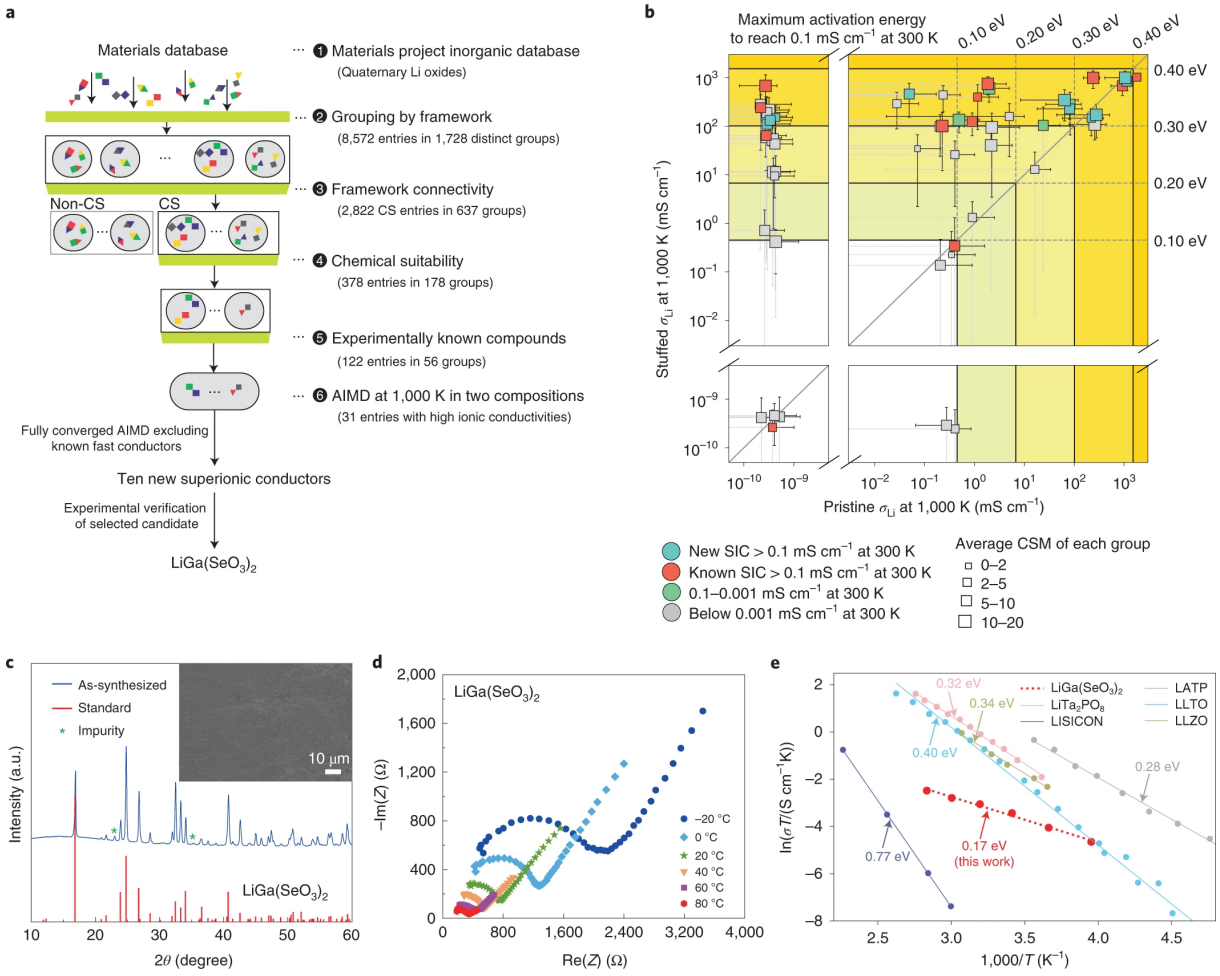

Figure 38: Identifying potential superionic conductors through computational screening. a,b, Diagram illustrating the multi-step computational screening process (a) and a summary presenting the calculated ionic conductivities of 56 materials from Step 6 (b). The minimum ionic conductivities (σ_{Li}) required at 1,000 K for achieving an extrapolated 0.1 mS cm^{-1} at 300 K are depicted by horizontal and vertical lines, with corresponding activation energies labeled. c, X-ray diffraction (XRD) pattern of $LiGa(SeO_3)_2$ with a scanning electron microscope (SEM) image of the densified pellet. d, Temperature-dependent impedance (Z) plots of $LiGa(SeO_3)_2$, where the semicircle represents bulk ionic conductivity. e, Arrhenius plot comparing the bulk ionic conductivities of $LiGa(SeO_3)_2$ to other oxide superionic conductors: $LiTa_2PO_8$, LISICON, $Li_{1+x}Al_xTi_{2-x}(PO_4)_3$, $Li_{3x}La_{2/3-x}TiO_3$ (LLTO), and $Li_7La_3Zr_2O_{12}$ (LLZO). The units are arbitrary (a.u.) Reprinted from Ref.,[273] with permission from Springer Nature.

Another example is the spinel structure, which exhibits a desirable combination of capacity and voltage.[267] Recent studies have reported experimental migration barriers of approximately 600 meV for Mg^{2+} in Cr- and Mn-spinel oxides, which aligns with density functional theory (DFT) calculations.[294,295] The strong Coulombic interactions between the Mg cations and the oxide host lattice generally impede the reversibility of Mg intercalation and result in elevated Mg migration barriers. In addition, migration in the spinel structure is mediated by intermediate octahedral sites whose relative stability to the initial tetrahedral site, called site preference, strongly influences the resulting migration barriers.[260] Migration barriers in spinel materials have recently been employed to derive a descriptor for ion mobility based on ionic radii, oxidation states, and electronegativities, screening of both cation and anion chemistry.[261] The utilization of this principle has demonstrated that oxide spinels incorporating electronegative transition metal cations of substantial size have the potential to exhibit elevated Mg^{2+} mobility. as shown in Figure 39.

In addition, models and simulations can predict critical battery parameters such as state of charge, state of health and cycle life, complementing experimental measurements for comprehensive performance evaluation. This combination enables accurate quantitative assessments of performance thresholds, such as remaining useful life and optimal rapid charging rates, thereby reducing the risks associated with short circuits or premature failures. Throughout the research process, theoretical models and simulations facilitate both virtual and physical experiments, providing valuable insights beyond observed phenomena. They act as a safeguard against potential human error or bias in data interpretation, validating empirical findings against real-time electrochemical performance.

Overall, the harmonious integration of theoretical calculations and experimental efforts provides a predictive framework for understanding the intricate electrochemical processes inherent in batteries. This holistic understanding reveals fundamental trends and guiding principles in battery material design, enabling us to design and manipulate electrochemical reactions to create superior batteries.

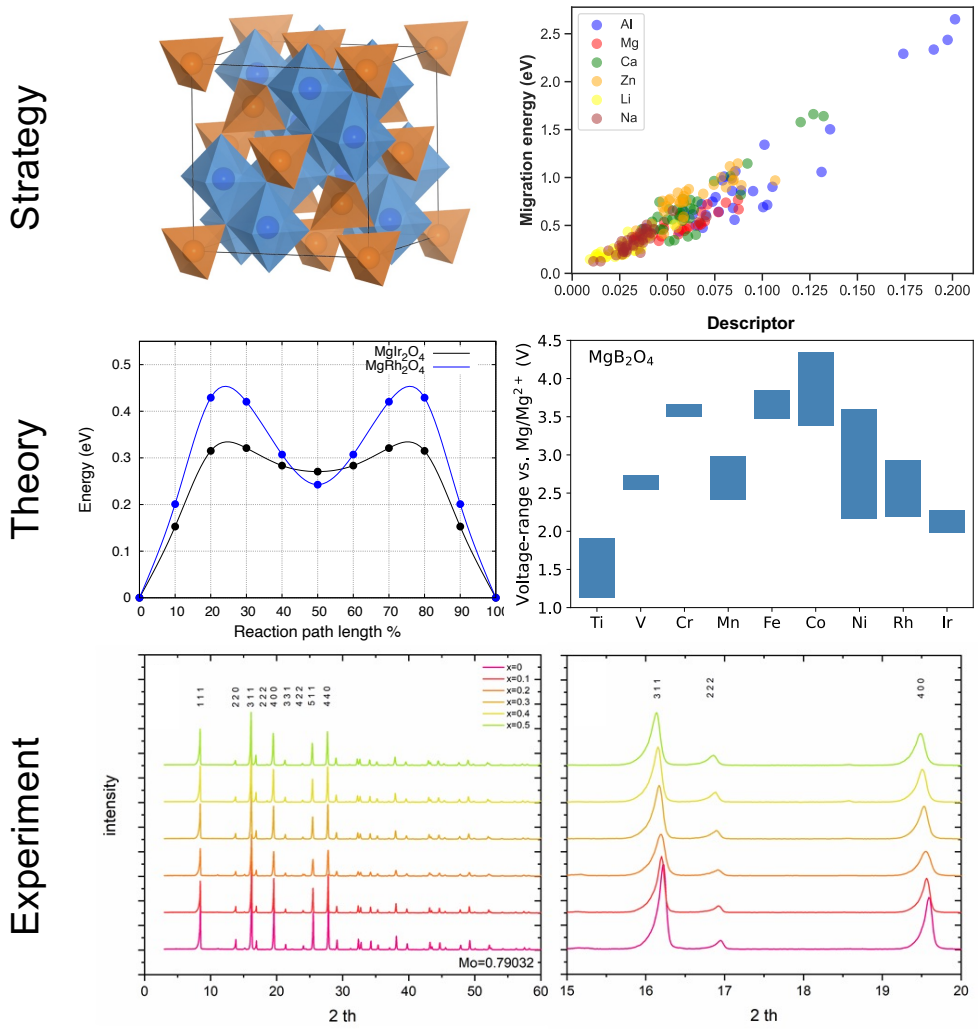

Figure 39: Screening for new Mg-ion conductors with a spinel framework and experimental verification of $MgCr_{2-x}Rh_xO_4$. The strategy employed includes the crystal structure and screening of all possible charge carriers, transition metals and anions to identify the optimal descriptor for ion mobility. The theoretical approach involves the identification of two compounds, namely $MgRh_2O_4$ and $MgIr_2O_4$, which exhibit promising ionic conductivity. This is based on the migration energies of Mg vacancies along the minimum energy paths, as determined by nudged elastic band calculations. Additionally, the voltage ranges required for use as cathode materials in Mg cells have been calculated. The experimental component comprises an X-ray diffraction pattern for synthesizing the $MgCr_{2-x}Rh_xO_4$ compound. Theory and experiment parts are reprinted from Ref.,[267] with permission from American Chemical Society.

14.1 Computational screening and workflows

Due to the advancement in computing power, computational methods for quickly finding materials with enhanced properties have gained popularity.[296–298] However, the interest in

materials usually involves multiple properties, and their relationship is complex. For instance, high-performance materials must remain stable under operating conditions to be valuable. Hence, a systematic approach is necessary for computational screening studies, guided by predefined workflows.

One such workflow, aimed at accelerating the discovery of battery electrode materials with improved migration properties,[299] is depicted in Figure 40. This workflow begins with evaluating the stability of candidate materials by analyzing volume changes and energy above the hull. Subsequently, open-circuit voltages are estimated by calculating insertion energy at vacant sites. Based on predetermined criteria, the computationally expensive Nudged Elastic Band (NEB) calculations, used to determine migration barrier heights, are performed if necessary.

This workflow was applied to identify suitable cathode materials for Mg-ion batteries,[300] utilizing ternary and quaternary structures from a database containing Mg, oxygen, and transition metals. Consequently, two cathode materials exhibiting significantly higher open-circuit potential than the Chevrel phase, the prototype cathode material for Mg-ion batteries, were discovered. However, these high-voltage materials are characterized by relatively high migration barriers exceeding 1 eV, consistent with the Brønsted–Evans–Polanyi (BEP) scaling relations between reaction energies and migration barriers discussed earlier. Note that a similar workflow was employed to screen topological quantum cathode materials as candidates for K-ion batteries.[301]

A comparable workflow was also utilized in a computational screening study focusing on perovskite materials, considering potential charge carriers such as Li, Na, K, Mg, Ca, Zn, and Al.[164] In total, 280 different perovskite compounds were evaluated. After assessing energy densities, volume changes, and energy above the hull, only 13 compounds emerged as promising candidates, for which diffusion barriers were then determined. Ultimately, three candidates suitable for post-Li battery technologies with multivalent ions were identified, warranting further investigation.

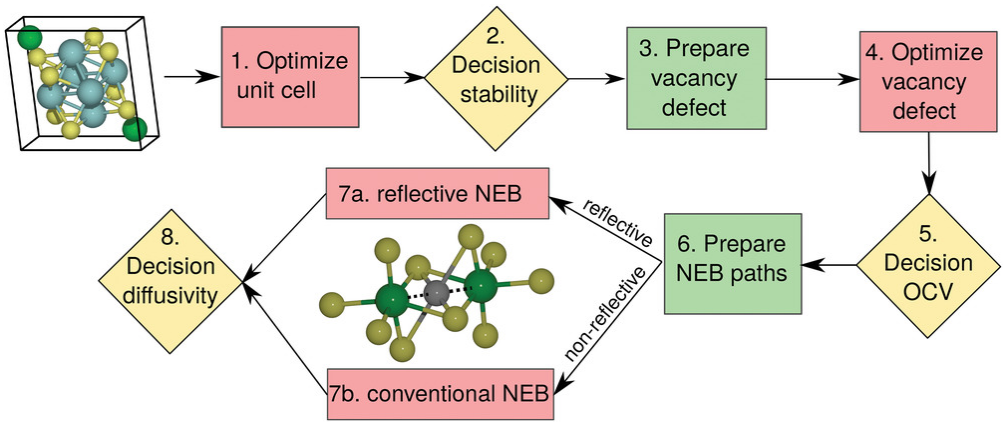

Figure 40: Illustration of the workflow for accelerating the discovery of battery electrode materials with improved migration properties. Reprinted from Ref. ,[299] published under a CC BY license.

15 Battery Informatics Data

Machine learning is a data-driven approach that aims to extrapolate patterns from existing examples to facilitate decision-making, bypassing the need for explicit programming.[291] The effectiveness of machine learning largely depends on the quality and quantity of data available, as abundant, high-quality data allows for more precise identification of underlying patterns, thereby improving predictive capabilities in unfamiliar scenarios.[302] In computer vision in particular, standardized datasets such as the Modified National Institute of Standards and Technology's collection of handwritten digits, which consists of 70,000 images for each digit,[303] illustrate the importance of rich and well-curated data. Similarly, in speech recognition, datasets such as those from the Chime-5 challenge, containing over 50 hours of conversation data with 98,448 utterances,[304] highlight the importance of rich and organized data in improving machine learning outcomes.

Despite this progress in certain areas, the materials science community has not fully benefited from such data-rich environments. Only a limited number of materials properties have been cataloged with both high quality and quantity, which is a significant barrier to the widespread adoption of machine learning as a standard tool in materials research. Table 5 provides an overview of the different types of datasets available for battery informatics

research, categorizing them according to their generation and collection methods, including computational databases, experimental datasets, high-throughput experimental data, and databases generated by text mining techniques. This categorization allows for a focused discussion of the challenges and opportunities presented by each type of dataset in the context of materials research.

Table 5: Examples of Different Types of Datasets for Battery Informatics Research

Dataset	Source	Content	Quantity	Challenge
Materials Project;[199] OQMD;[305,306] AFlowLib;[307] ESP;[308] CMR;[309] NOMAD[310]	Computation	Crystalline and electronic structure, energy, elastic properties, etc	>10,000	Expensive to collect kinetic and transport properties
ICSD;[201,202] COD;[311] Pauling file[312]	Published literature	Crystalline structure, phase diagram, intrinsic physical properties	>10,000	Restricted to a few properties such as crystalline structures

Computational databases use complex sequences of simulations to calculate and store thermodynamic, electronic and structural data for tens of thousands of inorganic compounds using density functional theory (Table 5). These meticulously curated databases provide vast amounts of high quality information and drive a significant proportion of materials informatics research. In particular, the prediction of formation energies stands out as an early demonstration of the power of statistical techniques in materials research. This methodology continues to be instrumental in the evaluation and refinement of new machine learning methods for materials property analysis, particularly in feature engineering and pattern recognition.[313]

Data from computational materials databases facilitate the estimation of various thermodynamic properties of battery materials. For example, the open circuit voltages of electrode materials can be derived by including phases in both discharge and charge states within

the dataset. The Materials Project[199] provides calculated voltages for an extensive range of intercalation and conversion electrode materials. Using this dataset, statistical analysis of voltage trends for oxide-based cathode candidates in Li-ion batteries reveals the influence of factors such as polyanion group, redox metal and oxygen/counter cation ratio on voltage and O_2 release temperature.[314] The wealth of data is used to synthesize overarching principles for the design of safe cathode systems.

In addition, material properties such as interface stability between the electrode and the solid electrolyte can be directly inferred from information in the computational materials database.[315] Aykol et al.[316] used computational data from OQMD[305,306] to screen a large number of oxygen-bearing materials with high phase stability, electrochemical stability and resistance to hydrofluoric acid for use as cathode coating layers. Optimal hydrofluoric acid scavengers were identified for different cathode types. Xiao et al.[317] carried out a screening of Li-containing compounds to identify coating materials with the desired stability and compatibility properties for cathodes and solid-state electrolytes. Subsequent detailed analyses led to the identification of suitable oxide candidates for cathode coating. The wealth of high-quality data stored in computational materials databases allows these studies to explore a wide compositional space for materials with specific functionalities without relying on machine learning.

A small subset of properties critical to battery research can be efficiently calculated using available computing resources. However, many important properties such as rate capability, cycling behavior, degradation and cell-level performance cannot be easily simulated using computational techniques. Even for properties that can be calculated using established methods, the computational cost escalates significantly when exploring a large and diverse configurational space. For example, the estimation of ionic transport properties in solid materials requires computationally intensive techniques such as the nudge elastic band (NEB) method and *ab initio* molecular dynamics (AIMD), both of which exceed the computational requirements of structure relaxation. Consequently, the availability of diffusion data for

machine learning (ML) approaches is limited. Despite the use of modern IT infrastructure and software tools, the evaluation of alkali superionic conductors has proceeded at a modest pace, exploring around 200 compositions over two years with relatively limited computational resources.[318] However, this exploration rate pales in comparison to the rapid calculation of thermodynamic properties.

In addition to computational databases, efforts have been made to create comprehensive and organized datasets of material properties by experimental means. The Inorganic Crystal Structure Database (ICSD)[201,202] archives structural details of inorganic substances dating back to 1913 and will have over 210,000 entries by December 2020, with updates every six months. The Crystallography Open Database (COD)[311] contains more than 150,000 structures and provides search and download facilities. The Pauling Files,[312] as of January 2019, include 51,974 entries of experimental and computational temperature-composition phase diagrams, 357,612 entries of crystalline structure data, and 156,274 records of various intrinsic physical properties of inorganic solids from a wide range of publications.

The construction of such large databases relies on the collective contributions of the scientific community and requires rigorous quality control. For individual researchers, a common approach is to apply standardized procedures within a parameter space and supplement the data with discrete measurements.

15.1 Machine learning in battery research

In the field of battery informatics, machine learning (ML) is finding widespread applications, with the exploration of innovative battery materials emerging as a particularly dynamic area. A common approach in the field of machine learning (ML) and materials discovery is to first construct predictive models that accurately predict a material's performance with respect to a specific function, typically characterized by one or a small number of critical material properties. This facilitates the identification of candidates with superior performance. However, as previously stated, it is necessary to address the issue of limited data availability. Here,

we review recent advances in ML-guided materials discovery with respect to key battery materials.

The search for novel solid-state ionic conductors presents a number of challenges.[266] Firstly, the process of ionic conduction is complex, involving dynamic phenomena on different time and length scales, influenced by geometric and chemical variables.[19] Developing an effective model for predicting conductivity requires careful feature engineering to capture the underlying physics of conduction. Second, known ionic conductors exhibit a great deal of structural and compositional diversity. For example, solid-state Li-ion conductors encompass compositions that include oxides, sulfides, nitrides and halides,[319] and exhibit a wide range of crystalline frameworks including perovskite,[320] argyrodite,[321] garnet,[322] NASICON,[323] and LGPS.[324] This extensive diversity poses a challenge to machine learning (ML) models, as they may struggle to navigate uncharted territory without sufficient reference data. Finally, ionic conductivity is highly sensitive to subtle compositional changes. While computational methods such as *ab initio* molecular dynamics (AIMD) can accurately simulate conductivity in agreement with experimental results, the practical application of these computationally intensive methods for screening numerous doping possibilities across a vast and unbounded configuration space remains a significant challenge.

In recent years, strategies have emerged to overcome these obstacles. The process of creating appropriate descriptors for feature engineering can be categorized into three main approaches: domain knowledge-based chemical features, physics-based robust descriptors, and feature abstraction through deep learning.

Domain knowledge-based chemical features use empirical rules to encode the structural and compositional properties of individual compounds into vectors. These hand-crafted descriptors cover various aspects such as elemental composition, local structural attributes such as bond coordination and distances, and overall structural properties such as crystalline cell volume and packing fraction. However, the abundance of hand-crafted features often leads to low correlation with the target property, requiring careful feature selection

to avoid overfitting. For example, Sendek[325] developed 40 empirical features to predict the conductivity of lithium-containing compounds, ultimately selecting five features for an optimal logistic model. Similarly, Nakayama[326] used histogram statistics of composition- and structure-derived features to create vector-form descriptors for oxides containing lithium and zinc, focusing on features such as the radial distribution function of the oxygen-oxygen interaction, which is critical for modeling the Li migration barrier using gradient boosting regression.

In another study, Jalem et al.[327] used neural network models to predict both the diffusion barrier and cohesive energy of olivine $LiMXO_4$ compounds. Their results showed positive correlations between the diffusion barrier and descriptors such as the average bond length of the Li octahedron, the distortion index of the Li octahedron and the Li-O-X bond angle. Conversely, negative correlations were observed with descriptors such as the effective coordination number of lithium, the distance between two X tetrahedra near the midplane, and the distortion index of the M octahedron. Extending their approach, Jalem et al.[328] identified six local structure descriptors for the diffusion barrier in tavorite $LiMTO_4F$ compounds using the same neural network architecture. In particular, they identified descriptors common to olivine and tavorite compounds, such as the variance of the bond angle of the M octahedron and the average bond length of the Li octahedron, while noting that the polyhedral volume of the Li octahedron and the effective charge of the M cation reduce the barrier.

Several factors influence the conductivity properties observed in the above studies. These factors include the number of coordinated lithium ions, the volume of interstitials, local distortions in the coordination environment and the charges carried by non-lithium species. Understanding how these factors relate to conductivity is straightforward from a physical point of view. For example, a high coordination number implies a significant energy barrier to bond breaking during diffusion. Conversely, for small cations such as lithium, a high coordination number often indicates a geometrically frustrated environment, which helps to minimize the energy gap between favorable and unfavorable bonding environments.[329] The

same geometric principle applies to the local distortion of lithium bonding environments. In particular, most lithium-ion conductors have distorted crystalline structures rather than highly symmetric lattices.[330] The ability to uncover complex relationships between structure and conductivity owes much to the robust capabilities of machine learning (ML) to detect hidden patterns through data analysis. However, it is important to be cautious as the results of feature selection can be sensitive to the choice of learning algorithm, selection method and available data, particularly when training data is limited.[331]

Physics-based descriptors are constructed from known physics of properties. For example, the ionic conductivity of most solids follows an Arrhenius equation with respect to temperature: $\sigma_T \propto \exp(-E_a/k_BT)$. This formula allows the conductivity at a given temperature to be quickly estimated from data at other temperatures. Zhu et al.[332] examined the mean square displacements (MSDs) obtained from short simulations at 800 and 1200 K for known superionic conductors. They found that all known lithium-based superionic conductors fall within certain MSD ranges, specifically $\text{MSD}_{800} > 5$ Å^2 and $\text{MSD}_{1200}/\text{MSD}_{800} < 7$. This observation suggests that high temperature data is strongly correlated with room temperature diffusion behavior. In the research by Fujimura et al.,[333] a model for predicting the conductivity of LISICON compounds used four descriptors: diffusion coefficients at 1600 K, transition temperatures, experimental temperature and average volume of disordered structures. The diffusion rate at elevated temperatures proved to be a reliable predictor of conductivity at lower temperatures; materials with high diffusion coefficients at 1600 K tended to have high conductivity at 373 K.

The use of deep learning-based features capitalizes on the inherent ability of deep learning to autonomously acquire features, thereby avoiding potential biases associated with manual craftsmanship. In the study of solid-state electrolytes, it is critical to accurately represent both the compositional information and crystalline structure of potential materials. Deep learning has made significant progress in representing these fundamental material attributes. In terms of compositional representation, deep learning models can extract patterns from

the formation energy of inorganic compounds, encapsulating the atomic properties of each element and correlating them with chemical trends.[334] This approach has the potential to streamline the process of representing chemical elements, reducing the need for manually created representations based on domain knowledge. In addition, crystal graph convolutional neural networks (CGCNN)[335] have emerged as a powerful tool for representing crystalline structures. In CGCNN, atoms are treated as nodes in a graph, while bonds are represented as edges connecting these nodes. This allows any crystal to be represented as a graph, with convolution and pooling layers providing invariance to permutations of atomic indices and unit cell choices. By incorporating global attributes alongside atomic and bond attributes, CGCNN goes beyond traditional neural networks to provide a more versatile graph-based approach.[336] These graph-based deep learning models have demonstrated remarkable ability to predict material properties. In addition, applying learned embeddings from CGCNN or graph networks to larger datasets has significantly improved property prediction performance, especially when data availability is limited.[337] Exploring the application of CGCNN in quantifying the relationship between crystalline structure and ionic conduction is a promising avenue for future research.

In the supervised learning approach (Figure 41), the model is trained to understand the relationship between ionic conductivity and various input features, enabling it to predict ionic conductivity.[327] To address the challenge of limited data availability, a practical solution is to restrict the exploration of the model to a limited space. This is particularly common in battery informatics, where the focus is often on specific families of structures due to the significant influence of crystalline structure prototypes on key properties of battery materials. This strategy is based on the premise that known structural families are more likely to yield desirable functional results. Consequently, exploration is reframed as optimization within this constrained space. By focusing on selected structural families, data is effectively consolidated, facilitating more accurate pattern extraction and reducing the need for extensive data availability to develop a reliable model. In addition, removing structural

variations as variables simplifies the representation of the crystalline lattice, overcoming a technical challenge.

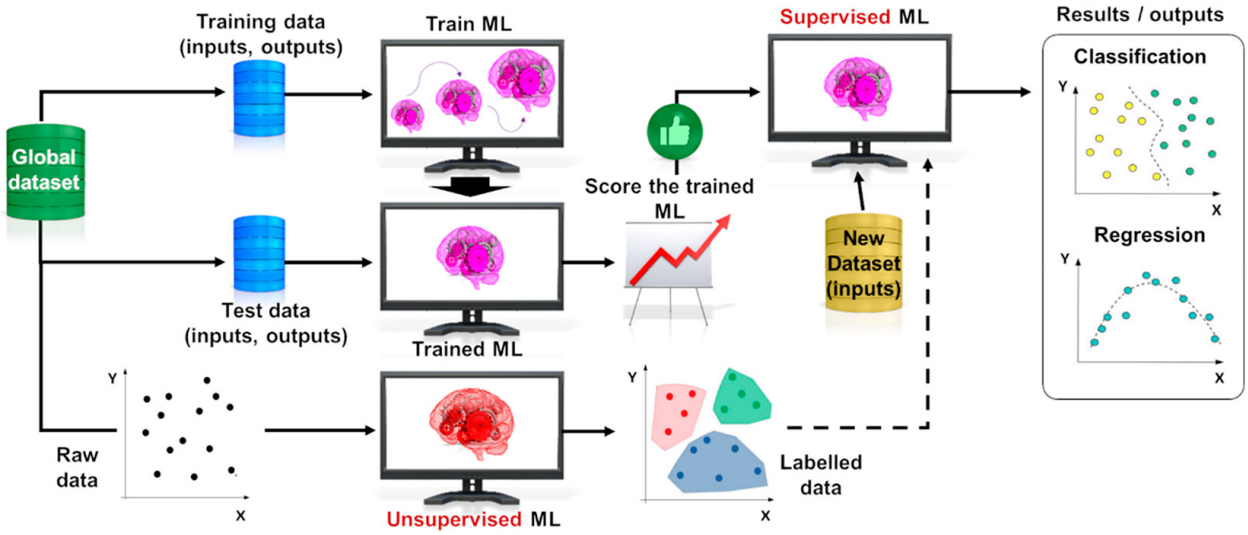

Figure 41: The fundamental operational concepts of a machine learning strategy encompassing supervised and unsupervised learning, as well as classification and regression techniques. In this context, we simplify by portraying classification as the sole application of unsupervised ML, notwithstanding the presence of other applications like dimensionality reduction. Reprinted from Ref.,[291] published under a CC BY license.

Historically, training data sizes in related studies have typically ranged from a few hundred examples derived from Density Functional Theory (DFT) calculations[333] to fewer than 100 from experimental sources.[338] However, a drawback of this limited exploration is the sacrifice of the model's generalizability across multiple structural families. To adapt to different structural families, ML models must be retrained and validated, which often requires independent efforts. A potential strategy to overcome this limitation is to transfer pre-established models from one system to another, as models predicting conductivity for different crystalline families may share common conductivity features.[328]

Another approach to supervised exploration involves assessing the potential of candidates to function as effective conductors, rather than directly estimating their ionic conductivity. Sendek et al.[325] used this method by transforming the regression task into a classification problem, where they used logistic regression to screen over 12,000 lithium-containing compounds across diverse compositional and structural landscapes. Out of 317 compounds

that met criteria such as thermodynamic phase stability, minimal electronic conduction, high electrochemical stability, absence of transition metals, and potentially low material cost with abundant elemental constituents, 21 were identified as likely to achieve conductivity greater than 10^{-4} S cm^{-1}. They then refined their screening process by training a new model based solely on compound compositions as input variables,[339] thereby extending predictions to compounds not initially present in the database. Notable compounds identified as promising ionic conductors included LiN_5P_3O, $Li_3Na_4O_3$, $LiPO_3$, $LiMg_3K_2O_4$, $LiNaMg_3O_5$, $Li_2K_3GaO_4$, $Li_5Na_2O_3$, Li_4NaGaO_4, Li_2MgO_2, $Li_5K_2O_3$ and $Li_5Na_2NO_2$. Furthermore, within the same logistic regression framework, predictions identified $LiAuI_4$ and $Ba_{38}Na_{58}Li_{26}N$ as potential superionic conductors.[340]

Machine learning is a powerful tool for exploring vast uncharted territories, often yielding a list of promising candidates that surpasses what traditional experimentation can achieve through sheer brute force. When it comes to the conductivity of solid electrolytes, the choice of dopant and defect concentrations significantly influences the process of fine-tuning the compositional degrees of freedom, thereby escalating the cost of experimentation. To overcome this hurdle, machine learning-based screening is typically followed by highly accurate simulations to further refine the selection of candidates.

In a study by Sendek et al.,[341] they artificially introduced a lithium vacancy into the supercell and used logistic regression to identify two compounds, $Li_5B_7S_{13}$ and $Li_2B_2S_5$, with remarkably high room-temperature conductivities. To introduce lithium vacancies and excess lithium more precisely, He et al.[342] suggested the use of aliovalent doping of immobile species. They proposed that the appropriate doping strategy should activate the concerted motion of multiple lithium ions by inserting lithium at high energy sites. Using this approach, they found that aliovalent substitution of $LiTaSiO_5$ and $LiAlSiO_4$ to introduce excess lithium improved lithium-ion conductivity at room temperature. This finding was confirmed in experiments where Zr-doped $Li_{1.1}Ta_{0.9}Zr_{0.1}SiO_5$ showed a conductivity approximately two orders of magnitude higher than stoichiometric $LiTaSiO_5$.[343]

The shift in the focus of machine learning (ML) from accurately predicting conductivity values to narrowing down candidates for investigation through costly simulations or experiments is driving the use of unsupervised learning for screening purposes (Figure 41). Zhang et al.[330] used a representation method to correlate the altered periodic lattice structures of lithium-containing compounds with a series of X-ray diffraction patterns at specific 2θ values. Using agglomerative hierarchical and spectral clustering techniques, they found that most of the recognized lithium-ion conductors grouped into two distinct clusters out of a total of seven, each exhibiting unique diffraction patterns. This clustering approach reduced the initial pool of 2,986 compounds to 82 unique candidates for evaluation of ionic conductivity. Subsequently, using atomistic molecular dynamics (AIMD) simulations, they identified 16 additional candidates with room temperature conductivity (σ_{RT}) exceeding 10^{-4} S cm^{-1}. Among these new materials, Li_8N_2Se, Li_6KBiO_6 and $Li_5P_2N_5$ exhibited room temperature conductivities exceeding 10^{-2} S cm^{-1}. Importantly, these newly predicted candidates exhibit novel structures, chemistries, and compositions that are significantly different from established solid-state lithium conductors (SSLCs), highlighting the ability of unsupervised learning to reveal materials beyond conventional chemistries.

15.2 Electrode Materials

In addition to investigating new electrolyte materials, machine learning (ML) has been utilized to explore innovative and more effective electrode materials. These studies have elucidated the intricate relationships between the structure and properties of electrode materials, encompassing various aspects such as voltage, structure, and energy landscapes. For instance, Joshi et al.[344] employed Deep Neural Networks (DNN), Support Vector Regression (SVR), and Kernel Ridge Regression (KRR) to forecast the voltage profile of cathode materials. Application of the ML model for candidate screening led to the identification of approximately 5,000 electrode materials for Sodium (Na) and Potassium (K) ion batteries with voltage characteristics comparable to those of Lithium (Li) ion batteries. Wang et

al.[345] investigated the volume changes occurring during the delithiation process of spinel and layered oxide cathodes. Their findings demonstrated that Partial Least Squares Regression effectively predicted volumetric changes, aligning closely with values calculated through Density Functional Theory (DFT). Shandiz[346] employed various classification algorithms to anticipate the crystalline structure within the compositional space of Li–Si–(Mn, Fe, Co)–O. Notably, the volume of the unit cell and the number of sites emerged as crucial factors influencing the crystalline lattice, alongside other parameters such as formation energies, convex hull energy, and band gap. Zhang et al.[347] utilized machine learning techniques to model the adsorption energy of lithium polysulfide species on layered sulfides. By extrapolating a pre-established model from $MoSe_2$ to predict adsorption on similarly structured WSe_2 surfaces, ML effectively reduced the computational expenses associated with DFT calculations while preserving accuracy, particularly in the context of two-dimensional layered compounds serving as host materials for lithium-sulfur battery cathodes.

The process of lithiation/delithiation in electrode materials often leads to significant disorder in the arrangement of lithium ions and vacancies within the crystal structure. Traditionally, this disorder has been analyzed using the cluster expansion method.[348] This method involves expressing a lattice model Hamiltonian as a combination of orthonormal basis functions representing different configurations of the occupancy variables. Recently, machine learning (ML) has emerged as a promising alternative for studying such disorder. Natarajan and Van der Ven[349] developed a neural network function to overcome the limitations of the linear Hamiltonian used in cluster expansion. In a case study on the spinel Li_xTiS_2, the neural network model showed an error of 36 meV per unit formula, significantly lower than the error of 89 meV per unit formula observed with the linear regression model. Hochins and Visvanathan[350] used a neural network potential to relax the disordered structures obtained from grand canonical Monte Carlo simulations of layered oxide cathodes using the cluster expansion Hamiltonian. Following structural relaxation, thermodynamic properties such as lattice parameters, free energy and entropy were calculated, and the predicted voltage profiles of

Li_xNiO_2 and Li_xCoO_2 were found to be in good agreement with experimental measurements. Moving beyond the cluster expansion framework, Eremin et al.[351] developed a model to describe the energy landscape of topotactic delithiation in $LiNiO_2$ and $LiNi_{0.8}Co_{0.15}Al_{0.05}O_2$ cathodes using structural descriptors that encode information about lithium and dopant occupancy. They concluded that the energetics of the process are primarily influenced by the arrangement of lithium ions within the layers and the relative positioning of lithium ions and dopants, rather than the specific positions of the dopants.

15.3 Sure independence screening and sparsifying operator

One effective approach for analyzing and interpreting large-scale battery informatics data is the Sure-Independence Screening and Sparsifying Operator (SISSO), proposed by Ouyang et al. [352] This method facilitates the extraction of critical descriptors from complex datasets, enhancing our understanding of the processes underlying battery performance and enabling the optimization of them. The SISSO is a compressed sensing technique designed to construct explicit, analytical symbolic regression models, denoted $\hat{f}$, by exploiting algebraic combinations of physical quantities represented by the feature set $X_{\mathbb{R}} = \{X_1, \ldots, X_d\}$. The effectiveness of SISSO extends to handling large datasets with millions or billions of potential feature combinations, unaffected by inter-correlated features.

Sure Independence Screening (SIS)[353] refers to the process by which SISSO efficiently estimates a desired property from a collection of initial or constructed feature combinations. This estimate is highly likely to approach certainty as more feature combinations are evaluated to fit the machine learning model to the dataset samples. Sparsifying involves the use of a sparse solution algorithm, called the sparsifying operator (SO), within SISSO. This algorithm facilitates the construction of a machine learning model, called desc_dim1, of reduced dimensionality. It achieves this reduction by using a component-wise regression or correlation learning technique to explore the feature space and minimize the number of

feature combinations (called descriptors d_i) in the final model,

$$\hat{f}(\mathbf{X}) = \sum_i c_i d_i(\mathbf{X}), \quad d_0 \equiv 1. \tag{56}$$

The coefficients c are obtained from a least squares fit of $\hat{f}(\mathbf{X}_i)$ to the material property Y of interest, with d_i as the i-th descriptors of the "desc_dim"-dimensional model $\hat{f}$. The feature combinations are formed by recursively applying a set of functional/algebraic (unary, binary, etc.) operators.

$$\Phi_k = \mathbf{Y}[\Phi_{k-1}, \ldots, \Phi_0], \quad k = 1, \ldots, \text{rung} \tag{57}$$

$$\mathbf{Y} = \{+, -, \times, /, ||, ^{-1}, ^2, ^3, ^{1/3}, \exp(-), \exp(), \ln, \sqrt{}\} \tag{58}$$

A subset of constructed features, denoted Φ_0, is derived from a set of features $\{X_1, ..., X_d\}$, where represents any combination of constructed features within Φ_{k-1}. By iteratively combining these features, new combinations are generated. Since the number of constructed feature combinations grows exponentially with the recursive feature combinations, the SIS step of SISSO evaluates each candidate feature combination using a standardized metric, such as the correlation coefficient ($\langle \cdot, \cdot \rangle$), which measures the absolute value of the inner product between the residual and the candidate feature combination. Only the top subs_sis feature combinations, denoted S_{nD}, containing no more than a maximum complexity of features from the dataset are retained. In general, larger sets are more likely to contain the optimal descriptor.

SISSO uses an iterative process to identify optimal feature combinations for modeling a given property. It first selects a set of candidate feature combinations, reducing the error between the predicted and actual property values at each step. The error in a n dimensional model is quantified as the difference between the actual property value $\mathbf{Y}$ and the predicted value based on the fitted descriptors $\sum_i^n c_i d_i(\mathbf{X})$, where the coefficients c_i are obtained from the fitting process. In the first iteration, the most influential one-dimensional descriptor is

identified and its fit to the feature of interest is evaluated. This error is then used to select additional features that correlate strongly with it, forming a set of two-dimensional descriptors. Two-dimensional descriptors are then constructed by fitting pairs of features from the combined sets of one- and two-dimensional descriptors. This process can be extended to higher dimensions by iteratively testing larger combinations of features. For each dimension, SISSO selects feature combinations that have the highest correlation with the error of the previous model. The final n-dimensional descriptor is determined by aggregating all previously selected feature subspaces until the error of the generated model reaches a desired level of accuracy that effectively captures the underlying data trend.

As an example, the prediction of the stability of the perovskite structure has long been a challenging task in the quest to discover new functional materials for various applications, including photovoltaics and electrocatalysts. Recently, a precise, interpretable, and one-dimensional tolerance factor[354] has been formulated which accurately predicts whether 92% of compounds in an experimental dataset of 576 ABX_3 materials (where X = O^{2-}, F^-, Cl^-, Br^-, I^-). This prediction is made using a data analytics approach based on SISSO. Additionally, it has been used to identify 23,314 new double perovskites ($A_2BB'X_6$), ranked by their likelihood of being stable as perovskites. This information provides valuable guidance for experimentalists and theorists on which compounds are most likely to be successfully synthesized and showcases a method for descriptor identification that can be applied to various other applications beyond predicting perovskite stability.

16 Discussion

Batteries are complex and dynamic multi-component systems in which many physical processes occur simultaneously during charging and discharging. The complexity of the issues arises primarily from the intricate nature of the interfaces and the limited selection of materials that must remain stable during charge and discharge cycles. Given that electrochemical

energy storage is dependent on processes involving bond formation and breakage, it is evident that quantum chemistry tools are indispensable for a comprehensive theoretical comprehension. Despite the advances in computational power and the development of more efficient methodologies, the complexity of electrochemical storage systems continues to present significant numerical and theoretical challenges. Nevertheless, first-principles electronic structure calculations play a crucial role in enhancing our atomistic understanding of the structures and processes in batteries. In addition to molecular mechanics methods and continuum approaches, these calculations are of great importance for enhancing the efficiency, stability, and safety of batteries.

Advances in computing power and the development of sophisticated computational tools now allow numerical studies to greatly accelerate the discovery of new materials. Using descriptors to establish correlations between material properties and ion mobility present promising examples that facilitate the identification of suitable materials and provide deeper insights into the factors that influence ion mobility in crystalline structures. Despite this progress, fundamental challenges remain with the so-called scaling relationships between conflicting material properties, which hinder the simultaneous optimization of multiple properties. Potential approaches to overcome these scaling relationships include co-intercalation, pillared structures and anionic redox.

Examples of experimental design informed by theoretical frameworks highlights the need for an iterative relationship between theory and experimentation, cycling continuously until the most promising battery materials are identified and refined. This methodology transcends specific battery chemistries and establishes universal principles applicable to the advancement of both monovalent and multivalent battery technologies. With the increasing influence of artificial intelligence, data-driven machine learning techniques are expected to contribute significantly to the design and discovery of battery materials, alongside high-throughput computational and experimental methods. In particular, computational screening and the development of descriptors for energy storage materials are critical to identifying

new materials with improved properties.

17 Conclusion and perspective

The aim of this review is to elucidate the theoretical framework and computational methods that relate the electronic structure and dynamic properties of rechargeable battery components to their macroscopic electrochemical properties. The performance of a rechargeable battery at the engineering level can be effectively described using robust phenomenological theories based on thermodynamic laws and fundamental kinetic principles. For example, understanding and predicting the voltage of a battery and the phase stability of its constituent materials can be achieved by studying the free energies of the phases involved. In addition, the rates at which a battery charges and discharges are determined by kinetic properties which, at a phenomenological level, are encoded in measures of ion mobility and parameters of response functions describing non-equilibrium electrochemical processes at the electrode/electrolyte interfaces. There are also well-established phenomenological theories that explain the phase transformations within an electrode as the concentration of the shuttled ion changes.

Despite their simplicity and effectiveness, phenomenological theories require experimental measurements to determine the material-specific thermodynamic potentials and kinetic coefficients on which they depend. An alternative to experimental methods is to calculate these thermodynamic and kinetic quantities from first principles. Although first-principles electronic structure methods are now fairly precise, the electrochemical processes in rechargeable batteries are typically thermally activated, making temperature and entropy critical variables to consider. Consequently, any first-principles approach that aims to integrate with phenomenological models of batteries must incorporate statistical mechanics

We have detailed rigorous approaches for calculating equilibrium thermodynamic properties and ionic transport coefficients from first principles. These computational methods have

proved to be invaluable complements to a wide range of experimental techniques, providing fundamental insights into the behavior of battery materials. However, the range of properties that can be rigorously calculated from first principles remains limited. For many phenomena there is still no clear link between the electronic structure and the parameters of the macroscopic response functions, and in some cases the accurate and validated phenomenological response functions themselves are still lacking.

We have identified the following key areas where future research could significantly advance our ability to model and design new battery chemistries and concepts:

- Development of Statistical Mechanics Methods: There is a need for advanced statistical mechanics methods to predict the ingredients for phase field models of topotactic phase transformations. This includes determining gradient energy coefficients and ionic mobilities in regions where phases are thermodynamically unstable and prone to spinodal decomposition.

- Electrode-Electrolyte Interface Processes: The complex atomic and electronic processes at the electrode-electrolyte interfaces of rechargeable batteries are the least understood. There is a need for more in situ experiments and multiscale modeling with electronic and atomic-level resolution to characterize the interface structure and determine the kinetic processes occurring during battery charging and discharging. These insights should then be distilled into interface response functions, linking atomistic-level properties to phenomenological coefficients.

- Simulation of Materials with Chemical Accuracy: A critical gap remains in simulating materials with chemical accuracy at the meso-/microscale. This is particularly important for understanding chemical reactions and transport at the electrode-electrolyte interfaces and within the electrodes and electrolytes themselves (e.g., grain boundaries and secondary phases). While recent advancements in machine learning interatomic potentials show promise for simpler chemistries, there is an urgent need for method-

ological developments that enable universal application to complex chemistries and bonding types, particularly those involving electron transfer.

- Data and Machine Learning in Battery Informatics: There is a significant opportunity to leverage data analytics and machine learning techniques to enhance battery performance. Developing robust machine learning models that can predict battery performance, degradation, and failure modes based on large datasets of operational and experimental data is crucial. These models can accelerate the discovery of new materials, optimize battery management systems, and provide insights into complex, multiscale phenomena in battery systems. Additionally, integrating machine learning with experimental and simulation data can help identify key descriptors and mechanisms, enabling more accurate and predictive modeling of battery behaviors across various conditions.

Acknowledgments

Financial support by the German Research Foundation (DFG) through Project ID 390 874 152 (EXC 2154, POLiS Cluster of Excellence) and by the Dr. Barbara Mez-Starck Foundation is gratefully acknowledge. The authors furthermore acknowledge computer time provided by the state of Baden-Württemberg through the bwHPC program and the German Research Foundation (DFG) through Grant no. INST 40/575-1 FUGG (JUSTUS 2 cluster). This work contributes to the research performed at CELEST (Center for Electrochemical Energy Storage Ulm-Karlsruhe).

References

(1) Goodenough, J. B.; Park, K.-S. The Li-Ion Rechargeable Battery: A Perspective. *J. Am. Chem. Soc.* **2013**, *135*, 1167–1176.

(2) Sudiarto, B.; Jufri, F. H.; Angkasa, F. F.; Widyanto, A. N.; Hudaya, C.; Husnayain, F.; Fitri, I. R.; Aryani, D. R.; Kim, J.-S.; Samual, M. G. et al. Battery technology for utility-scale battery energy storage system applications: A comparative review. *J. Energy Storage* **2026**, *149*, 120211.

(3) Olivetti, E. A.; Ceder, G.; Gaustad, G. G.; Fu, X. Lithium-Ion Battery Supply Chain Considerations: Analysis of Potential Bottlenecks in Critical Metals. *Joule* **2017**, *1*, 229–243.

(4) Tarascon, J.-M. Is lithium the new gold? *Nature Chem.* **2010**, *2*, 510–510.

(5) Placke, T.; Kloepsch, R.; Dühnen, S.; Winter, M. Lithium ion, lithium metal, and alternative rechargeable battery technologies: the odyssey for high energy density. *J. Solid State Electrochem.* **2017**, *21*, 1939–1964.

(6) Esser, B.; Ehrenberg, H.; Fichtner, M.; Groß, A.; Janek, J. Post-Lithium Storage—Shaping the Future. *Adv. Energy Mater.* **2025**, *15*, 2402824.

(7) Hwang, J.-Y.; Myung, S.-T.; Sun, Y.-K. Sodium-ion batteries: present and future. *Chem. Soc. Rev.* **2017**, *46*, 3529–3614.

(8) Yabuuchi, N.; Kubota, K.; Dahbi, M.; Komaba, S. Research Development on Sodium-Ion Batteries. *Chem. Rev.* **2014**, *114*, 11636–11682.

(9) Pfeiffer, L. F.; Dillenz, M.; Burgard, N.; Beran, P.; Roscher, D.; Zarrabeitia, M.; Drews, P.; Hervoches, C.; Mikhailova, D.; Omar, A. et al. From structure to electrochemistry: the influence of transition metal ordering on Na^+/vacancy orderings in P2-type Na_xMO_2 cathode materials for sodium-ion batteries. *J. Mater. Chem. A* **2025**, *13*, 540–560.

(10) Gregory, T. D.; Hoffman, R. J.; Winterton, R. C. Nonaqueous Electrochemistry of

Magnesium: Applications to Energy Storage. *J. Electrochem. Soc.* **1990**, *137*, 775–780.

(11) Aurbach, D.; Lu, Z.; Schechter, A.; Gofer, Y.; Gizbar, H.; Turgeman, R.; Cohen, Y.; Moshkovich, M.; Levi, E. Prototype systems for rechargeable magnesium batteries. *Nature* **2000**, *407*, 724–727.

(12) MacLaughlin, C. M. Status and Outlook for Magnesium Battery Technologies: A Conversation with Stan Whittingham and Sarbajit Banerjee. *ACS Energy Lett.* **2019**, *4*, 572–575.

(13) Davidson, R.; Verma, A.; Santos, D.; Hao, F.; Fincher, C. D.; Zhao, D.; Attari, V.; Schofield, P.; Van Buskirk, J.; Fraticelli-Cartagena, A. et al. Mapping mechanisms and growth regimes of magnesium electrodeposition at high current densities. *Mater. Horiz.* **2020**, *7*, 843–854.

(14) Glaser, C.; Dillenz, M.; Sarkar, K.; Sotoudeh, M.; Wei, Z.; Indris, S.; Maile, R.; Rohnke, M.; Müller-Buschbaum, K.; Groß, A. et al. MgB_2Se_4 Spinels (B = Sc, Y, Er, Tm) as Potential Mg-Ion Solid Electrolytes – Partial Ionic Conductivity and the Ion Migration Barrier. *Adv. Energy Mater.* **2024**, *14*, 2402269.

(15) Glaser, C.; Sotoudeh, M.; Dillenz, M.; Sarkar, K.; Bark, J. S.; Singh, S.; Wei, Z.; Indris, S.; Müller, R.; Leopold, K. et al. High Room-Temperature Magnesium Ion Conductivity in Spinel-Type $MgYb_2Se_4$ Solid Electrolyte. *Chem. Mater.* **2025**, *37*, 3353–3362.

(16) Janek, J.; Zeier, W. G. A solid future for battery development. *Nat. Energy* **2016**, *1*, 16141.

(17) Famprikis, T.; Canepa, P.; Dawson, J. A.; Islam, M. S.; Masquelier, C. Fundamentals of inorganic solid-state electrolytes for batteries. *Nat. Mater.* **2019**, *18*, 1278–1291.

(18) Janek, J.; Zeier, W. G. Challenges in speeding up solid-state battery development. *Nat. Energy* **2023**, *8*, 230–240.

(19) Sotoudeh, M.; Baumgart, S.; Dillenz, M.; Döhn, J.; Forster-Tonigold, K.; Helmbrecht, K.; Stottmeister, D.; Groß, A. Ion Mobility in Crystalline Battery Materials. *Adv. Energy Mater.* **2024**, *14*, 2302550.

(20) Cecchini, R.; Pelosi, G. Alessandro Volta and his battery. *IEEE Antennas Propag. Mag.* **1992**, *34*, 30–37.

(21) Lux, S. F.; Terborg, L.; Hachmöller, O.; Placke, T.; Meyer, H.-W.; Passerini, S.; Winter, M.; Nowak, S. LiTFSI Stability in Water and Its Possible Use in Aqueous Lithium-Ion Batteries: pH Dependency, Electrochemical Window and Temperature Stability. *J. Electrochem. Soc.* **2013**, *160*, A1694.

(22) Whittingham, M. S. Electrical Energy Storage and Intercalation Chemistry. *Science* **1976**, *192*, 1126–1127.

(23) Tarascon, J. M.; Armand, M. Issues and challenges facing rechargeable lithium batteries. *Nature* **2001**, *414*, 359–367.

(24) Goodenough, J. B.; Kim, Y. Challenges for Rechargeable Li Batteries. *Chem. Mater.* **2010**, *22*, 587–603.

(25) Goodenough, J. B. How we made the Li-ion rechargeable battery. *Nat. Electron.* **2018**, *1*, 204–204.

(26) Mizushima, K.; Jones, P.; Wiseman, P.; Goodenough, J. Li_xCoO_2 (0¡x¡-1): A new cathode material for batteries of high energy density. *Mater. Res. Bull.* **1980**, *15*, 783–789.

(27) Goodenough, J. B. Metallic oxides. *Prog. Solid State Chem.* **1971**, *5*, 145–399.

(28) Thackeray, M.; David, W.; Bruce, P.; Goodenough, J. Lithium insertion into manganese spinels. *Mater. Res. Bull.* **1983**, *18*, 461–472.

(29) Chebiam, R.; Kannan, A.; Prado, F.; Manthiram, A. Comparison of the chemical stability of the high energy density cathodes of lithium-ion batteries. *Electrochem. Commun.* **2001**, *3*, 624–627.

(30) Liu, X.; Zhong, W.; Liu, K.; Cui, Y.; Zhang, L.; Fu, W.; Liu, L. The toxicity differences of lithium-ion battery cathode materials, lithium iron phosphate (LFP) and lithium cobalt oxide (LCO) to zebrafish(Danio rerio): Mechanisms and environmental impacts. *Environ. Pollut.* **2026**, *396*, 127848.

(31) Li, Y.; Pan, Y.; Guo, J.; Yang, S.; Yang, Y.; Xu, H.; Cai, H.; Liu, T.; Liang, J.; Cao, C. Synergistic lattice–interface stabilization in multi-cation doped $LiMn_2O_4$ for advanced Lithium-ion batteries. *J. Electroanal. Chem.* **2026**, *1009*, 119981.

(32) Padhi, A. K.; Nanjundaswamy, K. S.; Goodenough, J. B. Phospho-olivines as Positive-Electrode Materials for Rechargeable Lithium Batteries. *J. Electrochem. Soc.* **1997**, *144*, 1188.

(33) Lu, W.; Zhou, C.; Zhang, L.; Zhao, Q.; Zhan, Z.; Shi, C.; Qian, W.; Wu, B. Experimental and numerical study on flow and heat transfer characteristics of series parallel flow channel liquid cooling plate for energy storage lithium iron phosphate battery module. *J. Energy Storage* **2026**, *155*, 121430.

(34) Groß, A.; Sakong, S. Modelling the electric double layer at electrode/electrolyte interfaces. *Curr. Opin. Electrochem.* **2019**, *14*, 1–6, Bioelectrochemistry Electrocatalysis.

(35) Liu, N.; Lu, Z.; Zhao, J.; McDowell, M. T.; Lee, H.-W.; Zhao, W.; Cui, Y. A pomegranate-inspired nanoscale design for large-volume-change lithium battery anodes. *Nature Nanotech.* **2014**, *9*, 187–192.

(36) Manthiram, A. A reflection on lithium-ion battery cathode chemistry. *Nat. Commun.* **2020**, *11*, 1550.

(37) Gauckler, C.; Dillenz, M.; Maroni, F.; Pfeiffer, L. F.; Biskupek, J.; Sotoudeh, M.; Fu, Q.; Kaiser, U.; Dsoke, S.; Euchner, H. et al. Detailed Structural and Electrochemical Comparison between High Potential Layered P2-NaMnNi and Doped P2-NaMnNiMg Oxides. *ACS Appl. Energy Mater.* **2022**, *5*, 13735–13750.

(38) Korthauer, R. *Lithium-Ion Batteries: Basics and Applications*; Springer Berlin Heidelberg, 2018.

(39) Zhu, X.; Sun, Z.; Wang, Z.; Wang, H.; Lin, N.; Shan, C. Thermal runaway in commercial lithium-ion cells under overheating condition and the safety assessment method: Effects of SoCs, cathode materials and packaging forms. *J. Energy Storage* **2023**, *68*, 107768.

(40) Yamada, A.; Kudo, Y.; Liu, K.-Y. Reaction Mechanism of the Olivine-Type $Li_x(Mn_{0.6}Fe_{0.4})PO_4$ ($0 \leq x \leq 1$). *J. Electrochem. Soc.* **2001**, *148*, A747.

(41) Deng, Y.; Yang, C.; Zou, K.; Qin, X.; Zhao, Z.; Chen, G. Recent Advances of Mn-Rich $LiFe_{1-y}Mn_yPO_4$ ($0.5 \leq y$ ¡ 1.0) Cathode Materials for High Energy Density Lithium Ion Batteries. *Adv. Energy Mater.* **2017**, *7*, 1601958.

(42) Xu, W.; Wang, J.; Ding, F.; Chen, X.; Nasybulin, E.; Zhang, Y.; Zhang, J.-G. Lithium metal anodes for rechargeable batteries. *Energy Environ. Sci.* **2014**, *7*, 513–537.

(43) Steiger, J.; Richter, G.; Wenk, M.; Kramer, D.; Mönig, R. Comparison of the growth of lithium filaments and dendrites under different conditions. *Electrochem. Commun.* **2015**, *50*, 11–14.

(44) Asenbauer, J.; Eisenmann, T.; Kuenzel, M.; Kazzazi, A.; Chen, Z.; Bresser, D. The success story of graphite as a lithium-ion anode material – fundamentals, remaining

challenges, and recent developments including silicon (oxide) composites. *Sustainable Energy Fuels* **2020**, *4*, 5387–5416.

(45) Xie, L.; Tang, C.; Bi, Z.; Song, M.; Fan, Y.; Yan, C.; Li, X.; Su, F.; Zhang, Q.; Chen, C. Hard Carbon Anodes for Next-Generation Li-Ion Batteries: Review and Perspective. *Adv. Energy Mater.* **2021**, *11*, 2101650.

(46) Azizi, J.; Groß, A.; Euchner, H. Computational Investigation of Carbon Based Anode Materials for Li- and Post-Li- Ion Batteries. *ChemSusChem* **2024**, *17*, e202301493.

(47) Shi, H.; Shi, C.; Jia, Z.; Zhang, L.; Wang, H.; Chen, J. Titanium dioxide-based anode materials for lithium-ion batteries: structure and synthesis. *RSC Adv.* **2022**, *12*, 33641–33652.

(48) Li, S.; Chen, C.; Fu, K.; Xue, L.; Zhao, C.; Zhang, S.; Hu, Y.; Zhou, L.; Zhang, X. Comparison of Si/C, Ge/C and Sn/C composite nanofiber anodes used in advanced lithium-ion batteries. *Solid State Ion.* **2014**, *254*, 17–26.

(49) Xu, K. Nonaqueous Liquid Electrolytes for Lithium-Based Rechargeable Batteries. *Chem. Rev.* **2004**, *104*, 4303–4418.

(50) Shanbedi, M.; Shahali, H.; Polycarpou, A. A.; Amiri, A. Recent developments in elevated-temperature lithium-ion batteries: materials, performance, innovations, and future challenges. *J. Energy Storage* **2026**, *154*, 121122.

(51) Li, Q.; Chen, J.; Fan, L.; Kong, X.; Lu, Y. Progress in electrolytes for rechargeable Li-based batteries and beyond. *Green Energy Environ.* **2016**, *1*, 18–42.

(52) Yang, L.; Ravdel, B.; Lucht, B. L. Electrolyte Reactions with the Surface of High Voltage $LiNi_{0.5}Mn_{1.5}O_4$ Cathodes for Lithium-Ion Batteries. *Electrochem. Solid-State Lett.* **2010**, *13*, A95.

(53) Croy, J. R.; Abouimrane, A.; Zhang, Z. Next-generation lithium-ion batteries: The promise of near-term advancements. *MRS Bull.* **2014**, *39*, 407–415.

(54) Ullah, S.; Song, B.; Gao, W.; Lu, J.; Khan, A.; Wu, Y.; He, J. Molecular Design of Intrinsically Safe and Stable Electrolytes for Lithium-ion batteries. *Coord. Chem. Rev.* **2026**, *558*, 217791.

(55) Zhang, Z.; Hu, L.; Wu, H.; Weng, W.; Koh, M.; Redfern, P. C.; Curtiss, L. A.; Amine, K. Fluorinated electrolytes for 5 V lithium-ion battery chemistry. *Energy Environ. Sci.* **2013**, *6*, 1806–1810.

(56) Neuhaus, J.; Forte, E.; von Harbou, E.; Hasse, H. Electrical conductivity of solutions of lithium bis(fluorosulfonyl)imide in mixed organic solvents and multi-objective solvent optimization for lithium-ion batteries. *J. Power Sources* **2018**, *398*, 215–223.

(57) Jin, Y.; Kneusels, N.-J. H.; Marbella, L. E.; Castillo-Martínez, E.; Magusin, P. C. M. M.; Weatherup, R. S.; Jónsson, E.; Liu, T.; Paul, S.; Grey, C. P. Understanding Fluoroethylene Carbonate and Vinylene Carbonate Based Electrolytes for Si Anodes in Lithium Ion Batteries with NMR Spectroscopy. *J. Am. Chem. Soc.* **2018**, *140*, 9854–9867.

(58) Ouatani, L. E.; Dedryvère, R.; Siret, C.; Biensan, P.; Reynaud, S.; Iratçabal, P.; Gonbeau, D. The Effect of Vinylene Carbonate Additive on Surface Film Formation on Both Electrodes in Li-Ion Batteries. *J. Electrochem. Soc.* **2008**, *156*, A103.

(59) Pieczonka, N. P. W.; Yang, L.; Balogh, M. P.; Powell, B. R.; Chemelewski, K.; Manthiram, A.; Krachkovskiy, S. A.; Goward, G. R.; Liu, M.; Kim, J.-H. Impact of Lithium Bis(oxalate)borate Electrolyte Additive on the Performance of High-Voltage Spinel/Graphite Li-Ion Batteries. *J. Phys. Chem. C* **2013**, *117*, 22603–22612.

(60) Tian, Y.; Zeng, G.; Rutt, A.; Shi, T.; Kim, H.; Wang, J.; Koettgen, J.; Sun, Y.; Ouyang, B.; Chen, T. et al. Promises and Challenges of Next-Generation "Beyond

Li-ion" Batteries for Electric Vehicles and Grid Decarbonization. *Chem. Rev.* **2021**, *121*, 1623–1669.

(61) Nitta, N.; Wu, F.; Lee, J. T.; Yushin, G. Li-ion battery materials: present and future. *Mater. Today* **2015**, *18*, 252–264.

(62) Eng, A. Y. S.; Soni, C. B.; Lum, Y.; Khoo, E.; Yao, Z.; Vineeth, S. K.; Kumar, V.; Lu, J.; Johnson, C. S.; Wolverton, C. et al. Theory-guided experimental design in battery materials research. *Sci. Adv.* **2022**, *8*, eabm2422.

(63) Singh, N.; Arthur, T. S.; Ling, C.; Matsui, M.; Mizuno, F. A high energy-density tin anode for rechargeable magnesium-ion batteries. *Chem. Commun.* **2013**, *49*, 149–151.

(64) Zhao-Karger, Z.; Gil Bardaji, M. E.; Fuhr, O.; Fichtner, M. A new class of non-corrosive, highly efficient electrolytes for rechargeable magnesium batteries. *J. Mater. Chem. A* **2017**, *5*, 10815–10820.

(65) Au, H.; Crespo-Ribadeneyra, M.; Titirici, M.-M. Beyond Li-ion batteries: performance, materials diversification, and sustainability. *One Earth* **2022**, *5*, 207–211.

(66) Jäckle, M.; Helmbrecht, K.; Smits, M.; Stottmeister, D.; Groß, A. Self-diffusion barriers: Possible descriptors for dendrite growth in batteries? *Energy Environ. Sci.* **2018**, *11*, 3400–3407.

(67) Li, J.; Ma, C.; Chi, M.; Liang, C.; Dudney, N. J. Solid Electrolyte: the Key for High-Voltage Lithium Batteries. *Adv. Energy Mater.* **2015**, *5*, 1401408.

(68) Kato, Y.; Hori, S.; Saito, T.; Suzuki, K.; Hirayama, M.; Mitsui, A.; Yonemura, M.; Iba, H.; Kanno, R. High-power all-solid-state batteries using sulfide superionic conductors. *Nat. Energy* **2016**, *1*, 16030.

(69) Bartsch, T.; Strauss, F.; Hatsukade, T.; Schiele, A.; Kim, A.-Y.; Hartmann, P.;

Janek, J.; Brezesinski, T. Gas Evolution in All-Solid-State Battery Cells. *ACS Energy Lett.* **2018**, *3*, 2539–2543.

(70) Walter, M.; Kovalenko, M. V.; Kravchyk, K. V. Challenges and benefits of post-lithium-ion batteries. *New J. Chem.* **2020**, *44*, 1677–1683.

(71) Wan, L. F.; Perdue, B. R.; Apblett, C. A.; Prendergast, D. Mg Desolvation and Intercalation Mechanism at the Mo_6S_8 Chevrel Phase Surface. *Chem. Mater.* **2015**, *27*, 5932–5940.

(72) Okoshi, M.; Yamada, Y.; Yamada, A.; Nakai, H. Theoretical Analysis on De-Solvation of Lithium, Sodium, and Magnesium Cations to Organic Electrolyte Solvents. *J. Electrochem. Soc.* **2013**, *160*, A2160.

(73) Ding, M. S.; Diemant, T.; Behm, R. J.; Passerini, S.; Giffin, G. A. Dendrite Growth in Mg Metal Cells Containing Mg(TFSI)2/Glyme Electrolytes. *J. Electrochem. Soc.* **2018**, *165*, A1983.

(74) Eaves-Rathert, J.; Moyer, K.; Zohair, M.; Pint, C. L. Kinetic- versus Diffusion-Driven Three-Dimensional Growth in Magnesium Metal Battery Anodes. *Joule* **2020**, *4*, 1324–1336.

(75) Porz, L.; Swamy, T.; Sheldon, B. W.; Rettenwander, D.; Frömling, T.; Thaman, H. L.; Berendts, S.; Uecker, R.; Carter, W. C.; Chiang, Y.-M. Mechanism of Lithium Metal Penetration through Inorganic Solid Electrolytes. *Adv. Energy Mater.* **2017**, *7*, 1701003.

(76) Koerver, R.; Zhang, W.; de Biasi, L.; Schweidler, S.; Kondrakov, A. O.; Kolling, S.; Brezesinski, T.; Hartmann, P.; Zeier, W. G.; Janek, J. Chemo-mechanical expansion of lithium electrode materials – on the route to mechanically optimized all-solid-state batteries. *Energy Environ. Sci.* **2018**, *11*, 2142–2158.

(77) Bucci, G.; Talamini, B.; Renuka Balakrishna, A.; Chiang, Y.-M.; Carter, W. C. Mechanical instability of electrode-electrolyte interfaces in solid-state batteries. *Phys. Rev. Mater.* **2018**, *2*, 105407.

(78) Gregory, T. D.; Hoffman, R. J.; Winterton, R. C. Nonaqueous Electrochemistry of Magnesium: Applications to Energy Storage. *J. Electrochem. Soc.* **1990**, *137*, 775.

(79) Levi, E.; Mitelman, A.; Aurbach, D.; Brunelli, M. Structural Mechanism of the Phase Transitions in the Mg-Cu-Mo_6S_8 System Probed by ex Situ Synchrotron X-ray Diffraction. *Chem. Mater.* **2007**, *19*, 5131–5142.

(80) Canepa, P.; Sai Gautam, G.; Hannah, D. C.; Malik, R.; Liu, M.; Gallagher, K. G.; Persson, K. A.; Ceder, G. Odyssey of Multivalent Cathode Materials: Open Questions and Future Challenges. *Chem. Rev.* **2017**, *117*, 4287–4341.

(81) Sun, X.; Bonnick, P.; Duffort, V.; Liu, M.; Rong, Z.; Persson, K. A.; Ceder, G.; Nazar, L. F. A high capacity thiospinel cathode for Mg batteries. *Energy Environ. Sci.* **2016**, *9*, 2273–2277.

(82) Sun, X.; Bonnick, P.; Nazar, L. F. Layered TiS_2 Positive Electrode for Mg Batteries. *ACS Energy Lett.* **2016**, *1*, 297–301.

(83) Liang, Y.; Yoo, H. D.; Li, Y.; Shuai, J.; Calderon, H. A.; Robles Hernandez, F. C.; Grabow, L. C.; Yao, Y. Interlayer-Expanded Molybdenum Disulfide Nanocomposites for Electrochemical Magnesium Storage. *Nano Lett.* **2015**, *15*, 2194–2202.

(84) Gu, Y.; Katsura, Y.; Yoshino, T.; Takagi, H.; Taniguchi, K. Rechargeable magnesium-ion battery based on a $TiSe_2$-cathode with d-p orbital hybridized electronic structure. *Sci. Rep.* **2015**, *5*, 12486.

(85) Liu, B.; Luo, T.; Mu, G.; Wang, X.; Chen, D.; Shen, G. Rechargeable Mg-Ion Batteries Based on WSe_2 Nanowire Cathodes. *ACS Nano* **2013**, *7*, 8051–8058.

(86) Emly, A.; Van der Ven, A. Mg Intercalation in Layered and Spinel Host Crystal Structures for Mg Batteries. *Inorg. Chem.* **2015**, *54*, 4394–4402.

(87) Liu, M.; Jain, A.; Rong, Z.; Qu, X.; Canepa, P.; Malik, R.; Ceder, G.; Persson, K. A. Evaluation of sulfur spinel compounds for multivalent battery cathode applications. *Energy Environ. Sci.* **2016**, *9*, 3201–3209.

(88) Liang, Y.; Feng, R.; Yang, S.; Ma, H.; Liang, J.; Chen, J. Rechargeable Mg Batteries with Graphene-like MoS_2 Cathode and Ultrasmall Mg Nanoparticle Anode. *Adv. Mater.* **2011**, *23*, 640–643.

(89) Rong, Z.; Malik, R.; Canepa, P.; Sai Gautam, G.; Liu, M.; Jain, A.; Persson, K.; Ceder, G. Materials Design Rules for Multivalent Ion Mobility in Intercalation Structures. *Chemistry of Materials* **2015**, *27*, 6016–6021.

(90) Liu, M.; Rong, Z.; Malik, R.; Canepa, P.; Jain, A.; Ceder, G.; Persson, K. A. Spinel compounds as multivalent battery cathodes: a systematic evaluation based on ab initio calculations. *Energy Environ. Sci.* **2015**, *8*, 964–974.

(91) Sai Gautam, G.; Canepa, P.; Abdellahi, A.; Urban, A.; Malik, R.; Ceder, G. The Intercalation Phase Diagram of Mg in V_2O_5 from First-Principles. *Chem. Mater.* **2015**, *27*, 3733–3742.

(92) Ling, C.; Zhang, R.; Arthur, T. S.; Mizuno, F. How General is the Conversion Reaction in Mg Battery Cathode: A Case Study of the Magnesiation of α-MnO_2. *Chem. Mater.* **2015**, *27*, 5799–5807.

(93) Kai, K.; Kobayashi, Y.; Yamada, Y.; Miyazaki, K.; Abe, T.; Uchimoto, Y.; Kageyama, H. Electrochemical characterization of single-layer MnO_2 nanosheets as a high-capacitance pseudocapacitor electrode. *J. Mater. Chem.* **2012**, *22*, 14691–14695.

(94) Yuan, C.; Zhang, Y.; Pan, Y.; Liu, X.; Wang, G.; Cao, D. Investigation of the intercalation of polyvalent cations (Mg^{2+}, Zn^{2+}) into λ-MnO_2 for rechargeable aqueous battery. *Electrochim. Acta* **2014**, *116*, 404–412.

(95) Spahr, M.; Novák, P.; Haas, O.; Nesper, R. Electrochemical insertion of lithium, sodium, and magnesium in molybdenum(VI) oxide. *J. Power Sources* **1995**, *54*, 346–351, Proceedings of the Seventh International Meeting on Lithium Batteries.

(96) Kaveevivitchai, W.; Jacobson, A. J. High Capacity Rechargeable Magnesium-Ion Batteries Based on a Microporous Molybdenum-Vanadium Oxide Cathode. *Chem. Mater.* **2016**, *28*, 4593–4601.

(97) Gershinsky, G.; Yoo, H. D.; Gofer, Y.; Aurbach, D. Electrochemical and Spectroscopic Analysis of Mg^{2+} Intercalation into Thin Film Electrodes of Layered Oxides: V_2O_5 and MoO_3. *Langmuir* **2013**, *29*, 10964–10972.

(98) Nam, K. W.; Kim, S.; Lee, S.; Salama, M.; Shterenberg, I.; Gofer, Y.; Kim, J.-S.; Yang, E.; Park, C. S.; Kim, J.-S. et al. The High Performance of Crystal Water Containing Manganese Birnessite Cathodes for Magnesium Batteries. *Nano Lett.* **2015**, *15*, 4071–4079.

(99) Ling, C.; Mizuno, F. Phase Stability of Post-spinel Compound AMn_2O_4 (A = Li, Na, or Mg) and Its Application as a Rechargeable Battery Cathode. *Chem. Mater.* **2013**, *25*, 3062–3071.

(100) Karol, J.; Ogolla, C. O.; Sotoudeh, M.; Dillenz, M.; Tobis, M.; Vollmer, E.; Malik, Y. T.; Zarrabeitia, M.; Groß, A.; Butz, B. et al. Nanoconfinement Geometry of Pillared V_2O_5 Determines Electrochemical Ion Intercalation Mechanisms, Storage Sites, and Diffusion Pathways. *ACS Nano* **2025**, *19*, 26904–26919.

(101) Guo, H.; Sotoudeh, M.; Rezeki, S.; Hu, Y.; Leiter, R.; Wellmann, J.; Fichtner, M.; Oschatz, M.; Groß, A.; Fleischmann, S. Regulating Solvent Co-Intercalation in Bi-

Layered Vanadium Oxides for Zinc Batteries by Nanoconfinement Chemistry. *Angew. Chem. Int. Ed.* **2026**, *65*, e20990.

(102) Novák, P.; Desilvestro, J. Electrochemical Insertion of Magnesium in Metal Oxides and Sulfides from Aprotic Electrolytes. *J. Electrochem. Soc.* **1993**, *140*, 140.

(103) Novák, P.; Imhof, R.; Haas, O. Magnesium insertion electrodes for rechargeable nonaqueous batteries - a competitive alternative to lithium? *Electrochim. Acta* **1999**, *45*, 351–367.

(104) Sai Gautam, G.; Canepa, P.; Richards, W. D.; Malik, R.; Ceder, G. Role of Structural H_2O in Intercalation Electrodes: The Case of Mg in Nanocrystalline Xerogel-V_2O_5. *Nano Letters* **2016**, *16*, 2426–2431.

(105) Senguttuvan, P.; Han, S.-D.; Kim, S.; Lipson, A. L.; Tepavcevic, S.; Fister, T. T.; Bloom, I. D.; Burrell, A. K.; Johnson, C. S. A High Power Rechargeable Nonaqueous Multivalent Zn/V_2O_5 Battery. *Adv. Energy Mater.* **2016**, *6*, 1600826.

(106) Orikasa, Y.; Masese, T.; Koyama, Y.; Mori, T.; Hattori, M.; Yamamoto, K.; Okado, T.; Huang, Z.-D.; Minato, T.; Tassel, C. et al. High energy density rechargeable magnesium battery using earth-abundant and non-toxic elements. *Scientific Reports* **2014**, *4*, 5622.

(107) Feng, Z.; Yang, J.; NuLi, Y.; Wang, J.; Wang, X.; Wang, Z. Preparation and electrochemical study of a new magnesium intercalation material $Mg_{1.03}Mn_{0.97}SiO_4$. *Electrochem. Commun.* **2008**, *10*, 1291–1294.

(108) Zheng, Y.; NuLi, Y.; Chen, Q.; Wang, Y.; Yang, J.; Wang, J. Magnesium cobalt silicate materials for reversible magnesium ion storage. *Electrochim. Acta* **2012**, *66*, 75–81.

(109) Makino, K.; Katayama, Y.; Miura, T.; Kishi, T. Electrochemical insertion of magnesium to $Mg_{0.5}Ti_2(PO_4)_3$. *J. Power Sources* **2001**, *99*, 66–69.

(110) Huang, Z.-D.; Masese, T.; Orikasa, Y.; Mori, T.; Yamamoto, k. Vanadium phosphate as a promising high-voltage magnesium ion (de)-intercalation cathode host. *RSC Adv.* **2015**, *5*, 8598–8603.

(111) Helmbrecht, K.; Groß, A. Ca Mobility in NASICON Battery Materials Studied from First-Principles. *J. Phys. Chem. C* **2025**, *129*, 5191–5196.

(112) Wu, J.; Gao, G.; Wu, G.; Liu, B.; Yang, H.; Zhou, X.; Wang, J. Tavorite-$FeSO_4F$ as a potential cathode material for Mg ion batteries: a first principles calculation. *Phys. Chem. Chem. Phys.* **2014**, *16*, 22974–22978.

(113) Huang, Z.-D.; Masese, T.; Orikasa, Y.; Mori, T.; Minato, T.; Tassel, C.; Kobayashi, Y.; Kageyama, H.; Uchimoto, Y. $MgFePO_4F$ as a feasible cathode material for magnesium batteries. *J. Mater. Chem. A* **2014**, *2*, 11578–11582.

(114) Bo, S.-H.; Grey, C. P.; Khalifah, P. G. Defect-Tolerant Diffusion Channels for Mg^{2+} Ions in Ribbon-Type Borates: Structural Insights into Potential Battery Cathodes $MgVBO_4$ and $Mg_xFe_{2-x}B_2O_5$. *Chem. Mater.* **2015**, *27*, 4630–4639.

(115) Wang, R. Y.; Wessells, C. D.; Huggins, R. A.; Cui, Y. Highly Reversible Open Framework Nanoscale Electrodes for Divalent Ion Batteries. *Nano Lett.* **2013**, *13*, 5748–5752.

(116) Wang, R. Y.; Shyam, B.; Stone, K. H.; Weker, J. N.; Pasta, M.; Lee, H.-W.; Toney, M. F.; Cui, Y. Reversible Multivalent (Monovalent, Divalent, Trivalent) Ion Insertion in Open Framework Materials. *Adv. Energy Mater.* **2015**, *5*, 1401869.

(117) Baumgart, S.; Sotoudeh, M.; Groß, A. Rhombohedral (R) Prussian White as Cathode Material: An Ab-initio Study. *Batteries & Supercaps* **2023**, *6*, e202300294.

(118) Baumgart, S.; Groß, A.; Sotoudeh, M. Data-Driven Site Occupancy Statistics in Cubic Prussian Blue. *ACS Phys. Chem. Au* **2025**, *5*, 346–355.

(119) Baumgart, S.; Sotoudeh, M.; Castelli, I. E.; Groß, A. Improved calculation framework for Prussian Blue analogues as a battery material. *EES Batteries* **2026**, *2*, 220–237.

(120) Lipson, A. L.; Pan, B.; Lapidus, S. H.; Liao, C.; Vaughey, J. T.; Ingram, B. J. Rechargeable Ca-Ion Batteries: A New Energy Storage System. *Chem. Mater.* **2015**, *27*, 8442–8447.

(121) Yoo, H. D.; Shterenberg, I.; Gofer, Y.; Gershinsky, G.; Pour, N.; Aurbach, D. Mg rechargeable batteries: an on-going challenge. *Energy Environ. Sci.* **2013**, *6*, 2265–2279.

(122) Ponrouch, A.; Frontera, C.; Bardé, F.; Palacín, M. R. Towards a calcium-based rechargeable battery. *Nature Mater.* **2016**, *15*, 169–172.

(123) Larcher, D.; Beattie, S.; Morcrette, M.; Edström, K.; Jumas, J.-C.; Tarascon, J.-M. Recent findings and prospects in the field of pure metals as negative electrodes for Li-ion batteries. *J. Mater. Chem.* **2007**, *17*, 3759–3772.

(124) Besenhard, J. O.; Winter, M. Advances in Battery Technology: Rechargeable Magnesium Batteries and Novel Negative-Electrode Materials for Lithium Ion Batteries. *ChemPhysChem* **2002**, *3*, 155–159.

(125) Lipson, A. L.; Han, S.-D.; Pan, B.; See, K. A.; Gewirth, A. A.; Liao, C.; Vaughey, J. T.; Ingram, B. J. Practical Stability Limits of Magnesium Electrolytes. *Journal of The Electrochemical Society* **2016**, *163*, A2253.

(126) Song, J.; Sahadeo, E.; Noked, M.; Lee, S. B. Mapping the Challenges of Magnesium Battery. *J. Phys. Chem. Lett.* **2016**, *7*, 1736–1749.

(127) Muldoon, J.; Bucur, C. B.; Oliver, A. G.; Sugimoto, T.; Matsui, M.; Kim, H. S.; Allred, G. D.; Zajicek, J.; Kotani, Y. Electrolyte roadblocks to a magnesium rechargeable battery. *Energy Environ. Sci.* **2012**, *5*, 5941–5950.

(128) Lu, Z.; Schechter, A.; Moshkovich, M.; Aurbach, D. On the electrochemical behavior of magnesium electrodes in polar aprotic electrolyte solutions. *J. Electroanal. Chem.* **1999**, *466*, 203–217.

(129) Keyzer, E. N.; Glass, H. F. J.; Liu, Z.; Bayley, P. M.; Dutton, S. E.; Grey, C. P.; Wright, D. S. Mg(PF6)2-Based Electrolyte Systems: Understanding Electrolyte–Electrode Interactions for the Development of Mg-Ion Batteries. *J. Am. Chem. Soc.* **2016**, *138*, 8682–8685.

(130) Aurbach, D.; Gizbar, H.; Schechter, A.; Chusid, O.; Gottlieb, H. E.; Gofer, Y.; Goldberg, I. Electrolyte Solutions for Rechargeable Magnesium Batteries Based on Organomagnesium Chloroaluminate Complexes. *J. Electrochem. Soc.* **2001**, *149*, A115.

(131) Pour, N.; Gofer, Y.; Major, D. T.; Aurbach, D. Structural Analysis of Electrolyte Solutions for Rechargeable Mg Batteries by Stereoscopic Means and DFT Calculations. *J. Am. Chem. Soc.* **2011**, *133*, 6270–6278.

(132) Doe, R. E.; Han, R.; Hwang, J.; Gmitter, A. J.; Shterenberg, I.; Yoo, H. D.; Pour, N.; Aurbach, D. Novel, electrolyte solutions comprising fully inorganic salts with high anodic stability for rechargeable magnesium batteries. *Chem. Commun.* **2014**, *50*, 243–245.

(133) Kim, H. S.; Arthur, T. S.; Allred, G. D.; Zajicek, J.; Newman, J. G.; Rodnyansky, A. E.; Oliver, A. G.; Boggess, W. C.; Muldoon, J. Structure and compatibility of a magnesium electrolyte with a sulphur cathode. *Nat. Commun.* **2011**, *2*, 427.

(134) Shao, Y.; Liu, T.; Li, G.; Gu, M.; Nie, Z.; Engelhard, M.; Xiao, J.; Lv, D.; Wang, C.;

Zhang, J.-G. et al. Coordination Chemistry in magnesium battery electrolytes: how ligands affect their performance. *Sci. Rep.* **2013**, *3*, 3130.

(135) Carter, T. J.; Mohtadi, R.; Arthur, T. S.; Mizuno, F.; Zhang, R.; Shirai, S.; Kampf, J. W. Boron Clusters as Highly Stable Magnesium-Battery Electrolytes. *Angew. Chem. Int. Ed.* **2014**, *53*, 3173–3177.

(136) Tutusaus, O.; Mohtadi, R.; Arthur, T. S.; Mizuno, F.; Nelson, E. G.; Sevryugina, Y. V. An Efficient Halogen-Free Electrolyte for Use in Rechargeable Magnesium Batteries. *Angew. Chem. Int. Ed.* **2015**, *54*, 7900–7904.

(137) Mohtadi, R.; Matsui, M.; Arthur, T. S.; Hwang, S.-J. Magnesium Borohydride: From Hydrogen Storage to Magnesium Battery. *Angew. Chem. Int. Ed.* **2012**, *51*, 9780–9783.

(138) Rajput, N. N.; Qu, X.; Sa, N.; Burrell, A. K.; Persson, K. A. The Coupling between Stability and Ion Pair Formation in Magnesium Electrolytes from First-Principles Quantum Mechanics and Classical Molecular Dynamics. *J. Am. Chem. Soc.* **2015**, *137*, 3411–3420.

(139) Huggins, R. A. *Advanced Batteries: Materials Science Aspects*; Springer New York, NY, 2008.

(140) Cha, E.; Patel, M.; Bhoyate, S.; Prasad, V.; Choi, W. Nanoengineering to achieve high efficiency practical lithium–sulfur batteries. *Nanoscale Horiz.* **2020**, *5*, 808–831.

(141) Van der Ven, A.; Deng, Z.; Banerjee, S.; Ong, S. P. Rechargeable Alkali-Ion Battery Materials: Theory and Computation. *Chem. Rev.* **2020**, *120*, 6977–7019.

(142) Eshetu, G. G.; Zhang, H.; Judez, X.; Adenusi, H.; Armand, M.; Passerini, S.; Figgemeier, E. Production of high-energy Li-ion batteries comprising silicon-containing anodes and insertion-type cathodes. *Nat. Commun.* **2021**, *12*, 5459.

(143) Hoffmann, R. An Extended Hückel Theory. I. Hydrocarbons. *J. Chem. Phys.* **1963**, *39*, 1397–1412.

(144) Mathew, K.; Sundararaman, R.; Letchworth-Weaver, K.; Arias, T. A.; Hennig, R. G. Implicit solvation model for density-functional study of nanocrystal surfaces and reaction pathways. *J. Chem. Phys.* **2014**, *140*, 084106.

(145) Reuter, K.; Scheffler, M. Composition, structure, and stability of RuO_2(110) as a function of oxygen pressure. *Phys. Rev. B* **2001**, *65*, 035406.

(146) Cheng, J.; Sulpizi, M.; Sprik, M. Redox potentials and pKa for benzoquinone from density functional theory based molecular dynamics. *J. Chem. Phys.* **2009**, *131*, 154504.

(147) Nørskov, J. K.; Rossmeisl, J.; Logadottir, A.; Lindqvist, L.; Kitchin, J. R.; Bligaard, T.; Jónsson, H. Origin of the Overpotential for Oxygen Reduction at a Fuel-Cell Cathode. *J. Phys. Chem. B* **2004**, *108*, 17886–17892.

(148) Peterson, A. A.; Abild-Pedersen, F.; Studt, F.; Rossmeisl, J.; Nørskov, J. K. How copper catalyzes the electroreduction of carbon dioxide into hydrocarbon fuels. *Energy Environ. Sci.* **2010**, *3*, 1311–1315.

(149) Hansen, H. A.; Man, I. C.; Studt, F.; Abild-Pedersen, F.; Bligaard, T.; Rossmeisl, J. Electrochemical chlorine evolution at rutile oxide (110) surfaces. *Phys. Chem. Chem. Phys.* **2010**, *12*, 283–290.

(150) Gossenberger, F.; Roman, T.; Groß, A. Hydrogen and halide co-adsorption on Pt(111) in an electrochemical environment: a computational perspective. *Electrochim. Acta* **2016**, *216*, 152–159.

(151) Rossmeisl, J.; Chan, K.; Skúlason, E.; Björketun, M. E.; Tripkovic, V. On the pH dependence of electrochemical proton transfer barriers. *Catal. Today* **2016**, *262*, 36–40, Electrocatalysis.

(152) Hohenberg, P.; Kohn, W. Inhomogeneous Electron Gas. *Phys. Rev.* **1964**, *136*, B864–B871.

(153) Kohn, W.; Sham, L. J. Self-Consistent Equations Including Exchange and Correlation Effects. *Phys. Rev.* **1965**, *140*, A1133–A1138.

(154) Euchner, H.; Groß, A. Atomistic modeling of Li- and post-Li-ion batteries. *Phys. Rev. Mater.* **2022**, *6*, 040302.

(155) Iftimie, R.; Minary, P.; Tuckerman, M. E. ¡i¿Ab initio¡/i¿ molecular dynamics: Concepts, recent developments, and future trends. *Proc. Natl. Acad. Sci.* **2005**, *102*, 6654–6659.

(156) Groß, A.; Sakong, S. Ab Initio Simulations of Water/Metal Interfaces. *Chem. Rev.* **2022**, *122*, 10746–10776.

(157) van Duin, A. C. T.; Strachan, A.; Stewman, S.; Zhang, Q.; Xu, X.; Goddard, W. A. ReaxFF$_{SiO}$ Reactive Force Field for Silicon and Silicon Oxide Systems. *J. Phys. Chem. A* **2003**, *107*, 3803–3811.

(158) Lin, H.; Truhlar, D. G. QM/MM: what have we learned, where are we, and where do we go from here? *Theor. Chem. Acc.* **2007**, *117*, 185–199.

(159) Voth, G. A. *Coarse-graining of condensed phase and biomolecular systems*, 1st ed.; CRC press, 2008.

(160) Kroese, D. P.; Brereton, T.; Taimre, T.; Botev, Z. I. Why the Monte Carlo method is so important today. *WIREs Comput. Stat.* **2014**, *6*, 386–392.

(161) Emmerich, H. *The Diffuse Interface Approach in Materials Science*; Springer Berlin, Heidelberg, 2003.

(162) Logan, D. *A First Course in the Finite Element Method*; Cengage Learning, 2016.

(163) Gschwind, F.; Rodriguez-Garcia, G.; Sandbeck, D.; Gross, A.; Weil, M.; Fichtner, M.; Hörmann, N. Fluoride ion batteries: Theoretical performance, safety, toxicity, and a combinatorial screening of new electrodes. *J. Fluor. Chem.* **2016**, *182*, 76–90.

(164) Döhn, J.; Groß, A. Computational Screening of Oxide Perovskites as Insertion-Type Cathode Material. *Adv. Energy and Sustainability Res.* **2024**, *5*, 2300204.

(165) Schwarz, K. Optimization of the Statistical Exchange Parameter α for the Free Atoms H through Nb. *Phys. Rev. B* **1972**, *5*, 2466–2468.

(166) Ceperley, D. M.; Alder, B. J. Ground State of the Electron Gas by a Stochastic Method. *Phys. Rev. Lett.* **1980**, *45*, 566–569.

(167) MA, S.-k.; BRUECKNER, K. A. Correlation Energy of an Electron Gas with a Slowly Varying High Density. *Phys. Rev.* **1968**, *165*, 18–31.

(168) Langreth, D. C.; Mehl, M. J. Beyond the local-density approximation in calculations of ground-state electronic properties. *Phys. Rev. B* **1983**, *28*, 1809–1834.

(169) Van Voorhis, T.; Scuseria, G. E. A novel form for the exchange-correlation energy functional. *J. Chem. Phys.* **1998**, *109*, 400–410.

(170) Becke, A. D. A new inhomogeneity parameter in density-functional theory. *J. Chem. Phys.* **1998**, *109*, 2092–2098.

(171) Tao, J.; Perdew, J. P.; Staroverov, V. N.; Scuseria, G. E. Climbing the Density Functional Ladder: Nonempirical Meta–Generalized Gradient Approximation Designed for Molecules and Solids. *Phys. Rev. Lett.* **2003**, *91*, 146401.

(172) Sun, J.; Ruzsinszky, A.; Perdew, J. P. Strongly Constrained and Appropriately Normed Semilocal Density Functional. *Phys. Rev. Lett.* **2015**, *115*, 036402.

(173) Becke, A. D. A new mixing of Hartree–Fock and local density-functional theories. *J. Chem. Phys.* **1993**, *98*, 1372–1377.

(174) Becke, A. D. Density-functional thermochemistry. III. The role of exact exchange. *J. Chem. Phys.* **1993**, *98*, 5648–5652.

(175) Harris, J.; Jones, R. O. The surface energy of a bounded electron gas. *J. Phys. F: Met. Phys.* **1974**, *4*, 1170.

(176) Langreth, D.; Perdew, J. The exchange-correlation energy of a metallic surface. *Solid State Commun.* **1975**, *17*, 1425–1429.

(177) Perdew, J. P.; Ernzerhof, M.; Burke, K. Rationale for mixing exact exchange with density functional approximations. *J. Chem. Phys.* **1996**, *105*, 9982–9985.

(178) Heyd, J.; Scuseria, G. E.; Ernzerhof, M. Hybrid functionals based on a screened Coulomb potential. *J. Chem. Phys.* **2003**, *118*, 8207–8215.

(179) Marsman, M.; Paier, J.; Stroppa, A.; Kresse, G. Hybrid functionals applied to extended systems. *J. Phys.: Condens. Matter* **2008**, *20*, 064201.

(180) Anisimov, V. I.; Zaanen, J.; Andersen, O. K. Band theory and Mott insulators: Hubbard U instead of Stoner I. *Phys. Rev. B* **1991**, *44*, 943–954.

(181) Liechtenstein, A. I.; Anisimov, V. I.; Zaanen, J. Density-functional theory and strong interactions: Orbital ordering in Mott-Hubbard insulators. *Phys. Rev. B* **1995**, *52*, R5467–R5470.

(182) Novák, P.; Kuneš, J.; Chaput, L.; Pickett, W. E. Exact exchange for correlated electrons. *phys. stat. sol. (b)* **2006**, *243*, 563–572.

(183) Sotoudeh, M.; Rajpurohit, S.; Blöchl, P.; Mierwaldt, D.; Norpoth, J.; Roddatis, V.; Mildner, S.; Kressdorf, B.; Ifland, B.; Jooss, C. Electronic structure of $Pr_{1-x}Ca_xMnO_3$. *Phys. Rev. B* **2017**, *95*, 235150.

(184) Ebrahimizadeh Abrishami, M.; Mohammadi, M.; Sotoudeh, M. Photocatalytic Dye Decomposition over $CaMnO_{3-\delta}$ and $Pr_{0.5}Ca_{0.5}MnO_3$: A Combined XPS and DFT Study. *Crystals* **2022**, *12*.

(185) Chevrier, V. L.; Ong, S. P.; Armiento, R.; Chan, M. K. Y.; Ceder, G. Hybrid density functional calculations of redox potentials and formation energies of transition metal compounds. *Phys. Rev. B* **2010**, *82*, 075122.

(186) Cococcioni, M.; de Gironcoli, S. Linear response approach to the calculation of the effective interaction parameters in the LDA + U method. *Phys. Rev. B* **2005**, *71*, 035105.

(187) Busch, M.; Sotoudeh, M. The role of exact exchange on the structure of water dimer radical cation: Hydrogen bond vs hemibond. *J. Chem. Phys.* **2023**, *159*, 034303.

(188) Seo, D.-H.; Urban, A.; Ceder, G. Calibrating transition-metal energy levels and oxygen bands in first-principles calculations: Accurate prediction of redox potentials and charge transfer in lithium transition-metal oxides. *Phys. Rev. B* **2015**, *92*, 115118.

(189) Urban, A.; Seo, D.-H.; Ceder, G. Computational understanding of Li-ion batteries. *npj Comput. Mater.* **2016**, *2*, 16002.

(190) Aydinol, M. K.; Kohan, A. F.; Ceder, G.; Cho, K.; Joannopoulos, J. Ab initio study of lithium intercalation in metal oxides and metal dichalcogenides. *Phys. Rev. B* **1997**, *56*, 1354–1365.

(191) Sakong, S.; Groß, A. The Importance of the Electrochemical Environment in the Electro-Oxidation of Methanol on Pt(111). *ACS Catal.* **2016**, *6*, 5575–5586.

(192) Jaynes, E. T. Information Theory and Statistical Mechanics. *Phys. Rev.* **1957**, *106*, 620–630.

(193) Zhou, F.; Maxisch, T.; Ceder, G. Configurational Electronic Entropy and the Phase Diagram of Mixed-Valence Oxides: The Case of Li_xFePO_4. *Phys. Rev. Lett.* **2006**, *97*, 155704.

(194) Bartel, C. J.; Millican, S. L.; Deml, A. M.; Rumptz, J. R.; Tumas, W.; Weimer, A. W.; Lany, S.; Stevanović, V.; Musgrave, C. B.; Holder, A. M. Physical descriptor for the Gibbs energy of inorganic crystalline solids and temperature-dependent materials chemistry. *Nat. Commun.* **2018**, *9*, 4168.

(195) Hautier, G.; Ong, S. P.; Jain, A.; Moore, C. J.; Ceder, G. Accuracy of density functional theory in predicting formation energies of ternary oxides from binary oxides and its implication on phase stability. *Phys. Rev. B* **2012**, *85*, 155208.

(196) Bartel, C. J.; Trewartha, A.; Wang, Q.; Dunn, A.; Jain, A.; Ceder, G. A critical examination of compound stability predictions from machine-learned formation energies. *npj Comput. Mater.* **2020**, *6*, 97.

(197) Ward, L.; Liu, R.; Krishna, A.; Hegde, V. I.; Agrawal, A.; Choudhary, A.; Wolverton, C. Including crystal structure attributes in machine learning models of formation energies via Voronoi tessellations. *Phys. Rev. B* **2017**, *96*, 024104.

(198) Faber, F. A.; Lindmaa, A.; von Lilienfeld, O. A.; Armiento, R. Machine Learning Energies of 2 Million Elpasolite (ABC_2D_6) Crystals. *Phys. Rev. Lett.* **2016**, *117*, 135502.

(199) Jain, A.; Ong, S. P.; Hautier, G.; Chen, W.; Richards, W. D.; Dacek, S.; Cholia, S.; Gunter, D.; Skinner, D.; Ceder, G. et al. Commentary: The Materials Project: A materials genome approach to accelerating materials innovation. *APL Mater.* **2013**, *1*, 011002.

(200) Bartel, C. J.; Weimer, A. W.; Lany, S.; Musgrave, C. B.; Holder, A. M. The role of decomposition reactions in assessing first-principles predictions of solid stability. *npj Comput. Mater.* **2019**, *5*, 4.

(201) Bergerhoff, G.; Hundt, R.; Sievers, R.; Brown, I. D. The inorganic crystal structure data base. *J. Chem. Inf. Comput. Sci.* **1983**, *23*, 66–69.

(202) Belsky, A.; Hellenbrandt, M.; Karen, V. L.; Luksch, P. New developments in the Inorganic Crystal Structure Database (ICSD): accessibility in support of materials research and design. *Acta Cryst.* **2002**, *58*, 364–369.

(203) Karsai, F.; Humer, M.; Flage-Larsen, E.; Blaha, P.; Kresse, G. Effects of electron-phonon coupling on absorption spectrum: K edge of hexagonal boron nitride. *Phys. Rev. B* **2018**, *98*, 235205.

(204) Salpeter, E. E.; Bethe, H. A. A Relativistic Equation for Bound-State Problems. *Phys. Rev.* **1951**, *84*, 1232–1242.

(205) Blöchl, P. E. Projector augmented-wave method. *Phys. Rev. B* **1994**, *50*, 17953–17979.

(206) Roy, A.; Sotoudeh, M.; Dinda, S.; Tang, Y.; Kübel, C.; Groß, A.; Zhao-Karger, Z.; Fichtner, M.; Li, Z. Improving rechargeable magnesium batteries through dual cation co-intercalation strategy. *Nat. Commun.* **2024**, *15*, 492.

(207) Dronskowski, R.; Bloechl, P. E. Crystal orbital Hamilton populations (COHP): energy-resolved visualization of chemical bonding in solids based on density-functional calculations. *J. Phys. Chem.* **1993**, *97*, 8617–8624.

(208) Leach, A. *Molecular Modelling: Principles and Applications*; Prentice Hall, 2001.

(209) Barnett, R. N.; Landman, U. Born-Oppenheimer molecular-dynamics simulations of finite systems: Structure and dynamics of $(H_2O)_2$. *Phys. Rev. B* **1993**, *48*, 2081–2097.

(210) Car, R.; Parrinello, M. Unified Approach for Molecular Dynamics and Density-Functional Theory. *Phys. Rev. Lett.* **1985**, *55*, 2471–2474.

(211) Daw, M. S.; Baskes, M. I. Embedded-atom method: Derivation and application to impurities, surfaces, and other defects in metals. *Phys. Rev. B* **1984**, *29*, 6443–6453.

(212) Behler, J.; Parrinello, M. Generalized Neural-Network Representation of High-Dimensional Potential-Energy Surfaces. *Phys. Rev. Lett.* **2007**, *98*, 146401.

(213) Bartók, A. P.; Payne, M. C.; Kondor, R.; Csányi, G. Gaussian Approximation Potentials: The Accuracy of Quantum Mechanics, without the Electrons. *Phys. Rev. Lett.* **2010**, *104*, 136403.

(214) Thompson, A.; Swiler, L.; Trott, C.; Foiles, S.; Tucker, G. Spectral neighbor analysis method for automated generation of quantum-accurate interatomic potentials. *J. Comput. Phys.* **2015**, *285*, 316–330.

(215) Leung, K. Predicting the voltage dependence of interfacial electrochemical processes at lithium-intercalated graphite edge planes. *Phys. Chem. Chem. Phys.* **2015**, *17*, 1637–1643.

(216) Stottmeister, D.; Wildersinn, L.; Maibach, J.; Hofmann, A.; Jeschull, F.; Groß, A. Unraveling Propylene Oxide Formation in Alkali Metal Batteries. *ChemSusChem* **2024**, *17*, e202300995.

(217) Stottmeister, D.; Groß, A. Toward the Formation of the Solid Electrolyte Interphase on Alkaline Metal Anodes: Ab Initio Simulations. *Batteries & Supercaps* **2023**, *6*, e202300156.

(218) Mishin, Y. In *Diffusion Processes in Advanced Technological Materials*; Gupta, D., Ed.; Springer Berlin Heidelberg: Berlin, Heidelberg, 2005; pp 113–171.

(219) de Blasio, P. V. F.; Jorgensen, P. B.; Garcia Lastra, J. M.; Bhowmik, A. Nanosecond MD of battery cathode materials with electron density description. *Energy Storage Mater.* **2023**, *63*, 103023.

(220) Fogarty, J. C.; Aktulga, H. M.; Grama, A. Y.; van Duin, A. C. T.; Pandit, S. A. A

reactive molecular dynamics simulation of the silica-water interface. *J. Chem. Phys.* **2010**, *132*, 174704.

(221) Borodin, O.; Bedrov, D. Interfacial Structure and Dynamics of the Lithium Alkyl Dicarbonate SEI Components in Contact with the Lithium Battery Electrolyte. *J. Phys. Chem. C* **2014**, *118*, 18362–18371.

(222) Lorenz, S.; Groß, A.; Scheffler, M. Representing high-dimensional potential-energy surfaces for reactions at surfaces by neural networks. *Chem. Phys. Lett.* **2004**, *395*, 210–215.

(223) Natarajan, S. K.; Behler, J. Neural network molecular dynamics simulations of solid–liquid interfaces: water at low-index copper surfaces. *Phys. Chem. Chem. Phys.* **2016**, *18*, 28704–28725.

(224) Nestler, B.; Garcke, H.; Stinner, B. Multicomponent alloy solidification: Phase-field modeling and simulations. *Phys. Rev. E* **2005**, *71*, 041609.

(225) Zhang, T.; Sotoudeh, M.; Groß, A.; McMeeking, R. M.; Kamlah, M. 3D microstructure evolution in NaxFePO4 storage particles for sodium-ion batteries. *J. Power Sources* **2023**, *565*, 232902.

(226) Daubner, S.; Dillenz, M.; Pfeiffer, L. F.; Gauckler, C.; Rosin, M.; Burgard, N.; Martin, J.; Axmann, P.; Sotoudeh, M.; Groß, A. et al. Combined study of phase transitions in the P2-type NaXNi1/3Mn2/3O2 cathode material: experimental, ab-initio and multiphase-field results. *npj Comput. Mater.* **2024**, *10*, 75.

(227) Daubner, S.; Weichel, M.; Schneider, D.; Nestler, B. Modeling intercalation in cathode materials with phase-field methods: Assumptions and implications using the example of LiFePO4. *Electrochim. Acta* **2022**, *421*, 140516.

(228) Choudhury, A.; Nestler, B. Grand-potential formulation for multicomponent phase transformations combined with thin-interface asymptotics of the double-obstacle potential. *Phys. Rev. E* **2012**, *85*, 021602.

(229) Wang, J.; Hao, J.; Duan, C.; Wang, X.; Wang, K.; Ma, C. A Fluoride-Ion-Conducting Solid Electrolyte with Both High Conductivity and Excellent Electrochemical Stability. *Small* **2022**, *18*, 2104508.

(230) Wert, C. A. Diffusion Coefficient of C in α-Iron. *Phys. Rev.* **1950**, *79*, 601–605.

(231) Vineyard, G. H. Frequency factors and isotope effects in solid state rate processes. *J. Phys. Chem. Sol.* **1957**, *3*, 121–127.

(232) Hänggi, P.; Talkner, P.; Borkovec, M. Reaction-rate theory: fifty years after Kramers. *Rev. Mod. Phys.* **1990**, *62*, 251.

(233) Henkelman, G.; Jónsson, H. Improved tangent estimate in the nudged elastic band method for finding minimum energy paths and saddle points. *J. Chem. Phys.* **2000**, *113*, 9978.

(234) Sheppard, D.; Terrell, R.; Henkelman, G. Optimization methods for finding minimum energy paths. *J. Chem. Phys.* **2008**, *128*, 134106.

(235) Canepa, P.; Bo, S.-H.; Sai Gautam, G.; Key, B.; Richards, W. D.; Shi, T.; Tian, Y.; Wang, Y.; Li, J.; Ceder, G. High magnesium mobility in ternary spinel chalcogenides. *Nat. Commun.* **2017**, *8*, 1759.

(236) Rong, Z.; Kitchaev, D.; Canepa, P.; Huang, W.; Ceder, G. An efficient algorithm for finding the minimum energy path for cation migration in ionic materials. *J. Chem. Phys.* **2016**, *145*, 074112.

(237) Adams, S.; Rao, R. P. High power lithium ion battery materials by computational design. *Phys. Status Solidi A* **2011**, *208*, 1746–1753.

(238) Nishitani, Y.; Adams, S.; Ichikawa, K.; Tsujita, T. Evaluation of magnesium ion migration in inorganic oxides by the bond valence site energy method. *Solid State Ion.* **2018**, *315*, 111–115.

(239) Schreiner, M.; Bhowmik, A.; Vegge, T.; Jørgensen, P. B.; Winther, O. NeuralNEB—neural networks can find reaction paths fast. *Mach. Learn.: Sci. Technol.* **2022**, *3*, 045022.

(240) Kahle, L.; Marcolongo, A.; Marzari, N. Modeling lithium-ion solid-state electrolytes with a pinball model. *Phys. Rev. Mater.* **2018**, *2*, 065405.

(241) Islam, M. S.; Fisher, C. A. J. Lithium and sodium battery cathode materials: computational insights into voltage, diffusion and nanostructural properties. *Chem. Soc. Rev.* **2014**, *43*, 185–204.

(242) Sotoudeh, M.; Groß, A. Computational screening and descriptors for the ion mobility in energy storage materials. *Curr. Opin. Electrochem.* **2024**, *46*, 101494.

(243) Brønsted, J. Acid and Basic Catalysis. *Chem. Rev.* **1928**, *5*, 231–338.

(244) Evans, M.; Polanyi, M. Inertia and driving force of chemical reactions. *Trans. Faraday Soc.* **1938**, *34*, 11–24.

(245) Dillenz, M.; Sotoudeh, M.; Glaser, C.; Janek, J.; Groß, A.; Euchner, H. Unravelling Charge Carrier Mobility in d_0-Metal-based Spinels. *Batter. Supercaps* **2022**, *5*, e202200164.

(246) Hannagan, R. T.; Giannakakis, G.; Flytzani-Stephanopoulos, M.; Sykes, E. C. H. Single-Atom Alloy Catalysis. *Chem. Rev.* **2020**, *120*, 12044–12088.

(247) Lucci, F. R.; Marcinkowski, M. D.; Lawton, T. J.; Sykes, E. C. H. H_2 Activation and Spillover on Catalytically Relevant Pt–Cu Single Atom Alloys. *J. Phys. Chem. C* **2015**, *119*.

(248) Dillenz, M.; Sotoudeh, M.; Euchner, H.; Groß, A. Screening of Charge Carrier Migration in the $MgSc_2Se_4$ Spinel Structure. *Front. Energy Res.* **2020**, *8*, 584654.

(249) Zhang, B.; Tan, R.; Yang, L.; Zheng, J.; Zhang, K.; Mo, S.; Lin, Z.; Pan, F. Mechanisms and properties of ion-transport in inorganic solid electrolytes. *Energy Storage Mater.* **2018**, *10*, 139–159.

(250) Fisher, C. A. J.; Hart Prieto, V. M.; Islam, M. S. Lithium Battery Materials $LiMPO_4$ (M = Mn, Fe, Co, and Ni): Insights into Defect Association, Transport Mechanisms, and Doping Behavior. *Chem. Mater.* **2008**, *20*, 5907–5915.

(251) Petkov, V.; Trikalitis, P. N.; Bozin, E. S.; Billinge, S. J. L.; Vogt, T.; Kanatzidis, M. G. Structure of V2O5·nH2O Xerogel Solved by the Atomic Pair Distribution Function Technique. *J. Am. Chem. Soc.* **2002**, *124*, 10157–10162.

(252) Zhang, M.; Kitchaev, D. A.; Lebens-Higgins, Z.; Vinckeviciute, J.; Zuba, M.; Reeves, P. J.; Grey, C. P.; Whittingham, M. S.; Piper, L. F. J.; Van der Ven, A. et al. Pushing the limit of 3d transition metal-based layered oxides that use both cation and anion redox for energy storage. *Nature Reviews Materials* **2022**, *7*, 522–540.

(253) Seo, D.-H.; Lee, J.; Urban, A.; Malik, R.; Kang, S.; Ceder, G. The structural and chemical origin of the oxygen redox activity in layered and cation-disordered Li-excess cathode materials. *Nature Chemistry* **2016**, *8*, 692–697.

(254) Yahia, M. B.; Vergnet, J.; Saubanère, M.; Doublet, M.-L. Author Correction: Unified picture of anionic redox in Li/Na-ion batteries. *Nat. Mater.* **2019**, *18*, 1384–1384.

(255) Xie, Y.; Saubanère, M.; Doublet, M.-L. Requirements for reversible extra-capacity in Li-rich layered oxides for Li-ion batteries. *Energy Environ. Sci.* **2017**, *10*, 266–274.

(256) Hong, J.; Gent, W. E.; Xiao, P.; Lim, K.; Seo, D.-H.; Wu, J.; Csernica, P. M.;

Takacs, C. J.; Nordlund, D.; Sun, C.-J. et al. Metal–oxygen decoordination stabilizes anion redox in Li-rich oxides. *Nat. Mater.* **2019**, *18*, 256–265.

(257) Radin, M. D.; Vinckeviciute, J.; Seshadri, R.; Van der Ven, A. Manganese oxidation as the origin of the anomalous capacity of Mn-containing Li-excess cathode materials. *Nat. Energy* **2019**, *4*, 639–646.

(258) Oishi, M.; Yamanaka, K.; Watanabe, I.; Shimoda, K.; Matsunaga, T.; Arai, H.; Ukyo, Y.; Uchimoto, Y.; Ogumi, Z.; Ohta, T. Direct observation of reversible oxygen anion redox reaction in Li-rich manganese oxide, Li2MnO3, studied by soft X-ray absorption spectroscopy. *J. Mater. Chem. A* **2016**, *4*, 9293–9302.

(259) Kitchaev, D. A.; Vinckeviciute, J.; Van der Ven, A. Delocalized Metal-Oxygen π-Redox Is the Origin of Anomalous Nonhysteretic Capacity in Li-Ion and Na-Ion Cathode Materials. *Journal of the American Chemical Society* **2021**, *143*, 1908–1916.

(260) Sotoudeh, M.; Dillenz, M.; Groß, A. Mechanism of Magnesium Transport in Spinel Chalcogenides. *Adv. Energy Sustainability Res.* **2021**, *2*, 2100113.

(261) Sotoudeh, M.; Groß, A. Descriptor and Scaling Relations for Ion Mobility in Crystalline Solids. *JACS Au* **2022**, *2*, 463–471.

(262) Allred, A. Electronegativity values from thermochemical data. *J. Inorg. Nucl. Chem.* **1961**, *17*, 215 – 221.

(263) Maroni, F.; Dongmo, S.; Gauckler, C.; Marinaro, M.; Wolfahrt-Mehrens, M. Through the Maze of Multivalent-ion Batteries: A Critical Review on the status of the research on cathode materials for Mg^{2+} and Ca^{2+} ions insertion. *Batteries & Supercaps* **2021**,

(264) Liu, M.; Jain, A.; Rong, Z.; Qu, X.; Canepa, P.; Malik, R.; Ceder, G.; Persson, K. A. Evaluation of sulfur spinel compounds for multivalent battery cathode applications. *Energy Environ. Sci.* **2016**, *9*, 3201–3209.

(265) Mao, M.; Ji, X.; Hou, S.; Gao, T.; Wang, F.; Chen, L.; Fan, X.; Chen, J.; Ma, J.; Wang, C. Tuning Anionic Chemistry To Improve Kinetics of Mg Intercalation. *Chem. Mater.* **2019**, *31*, 3183–3191.

(266) Bachman, J. C.; Muy, S.; Grimaud, A.; Chang, H.-H.; Pour, N.; Lux, S. F.; Paschos, O.; Maglia, F.; Lupart, S.; Lamp, P. et al. Inorganic Solid-State Electrolytes for Lithium Batteries: Mechanisms and Properties Governing Ion Conduction. *Chem. Rev.* **2016**, *116*, 140–162.

(267) Sotoudeh, M.; Dillenz, M.; Döhn, J.; Hansen, J.; Dsoke, S.; Groß, A. Oxide Spinels with Superior Mg Conductivity. *Chem. Mater.* **2023**, *35*, 4786–4797.

(268) Muy, S.; Bachman, J. C.; Giordano, L.; Chang, H.-H.; Abernathy, D. L.; Bansal, D.; Delaire, O.; Hori, S.; Kanno, R.; Maglia, F. et al. Tuning mobility and stability of lithium ion conductors based on lattice dynamics. *Energy Environ. Sci.* **2018**, *11*, 850–859.

(269) Bachman, J. C.; Muy, S.; Grimaud, A.; Chang, H.-H.; Pour, N.; Lux, S. F.; Paschos, O.; Maglia, F.; Lupart, S.; Lamp, P. et al. Inorganic Solid-State Electrolytes for Lithium Batteries: Mechanisms and Properties Governing Ion Conduction. *Chem. Rev.* **2016**, *116*, 140–162.

(270) Gordiz, K.; Muy, S.; Zeier, W. G.; Shao-Horn, Y.; Henry, A. Enhancement of ion diffusion by targeted phonon excitation. *Cell Rep.* **2021**, *2*, 100431.

(271) Kraft, M. A.; Culver, S. P.; Calderon, M.; Böcher, F.; Krauskopf, T.; Senyshyn, A.; Dietrich, C.; Zevalkink, A.; Janek, J.; Zeier, W. G. Influence of Lattice Polarizability on the Ionic Conductivity in the Lithium Superionic Argyrodites Li_6PS_5X (X = Cl, Br, I). *J. Am. Chem. Soc.* **2017**, *139*, 10909–10918.

(272) Wang, Y.; Richards, W. D.; Ong, S. P.; Miara, L. J.; Kim, J. C.; Mo, Y.; Ceder, G.

Design principles for solid-state lithium superionic conductors. *Nat. Mater.* **2015**, *14*, 1026.

(273) Jun, K.; Sun, Y.; Xiao, Y.; Zeng, Y.; Kim, R.; Kim, H.; Miara, L. J.; Im, D.; Wang, Y.; Ceder, G. Lithium superionic conductors with corner-sharing frameworks. *Nature Materials* **2022**, *21*, 924–931.

(274) Sotoudeh, M.; Groß, A. Stability of Magnesium Binary and Ternary Compounds for Batteries Determined from First Principles. *J. Phys. Chem. Lett.* **2022**, *13*, 10092–10100.

(275) Kim, K.; Siegel, D. J. Correlating lattice distortions, ion migration barriers, and stability in solid electrolytes. *J. Mater. Chem. A* **2019**, *7*, 3216–3227.

(276) Sun, Y.; Wang, Y.; Liang, X.; Xia, Y.; Peng, L.; Jia, H.; Li, H.; Bai, L.; Feng, J.; Jiang, H. et al. Rotational cluster anion enabling superionic conductivity in sodium-rich antiperovskite Na_3OBH_4. *J. Am. Chem. Soc.* **2019**, *141*, 5640–5644.

(277) Zhang, Z.; Nazar, L. F. Exploiting the paddle-wheel mechanism for the design of fast ion conductors. *Nat. Rev. Mater.* **2022**, *7*, 389–405.

(278) Kim, K.; Siegel, D. J. Machine learning reveals factors that control ion mobility in anti-perovskite solid electrolytes. *J. Mater. Chem. A* **2022**, *10*, 15169–15182.

(279) López, C.; Emperador, A.; Saucedo, E.; Rurali, R.; Cazorla, C. Universal ion-transport descriptors and classes of inorganic solid-state electrolytes. *Mater. Horiz.* **2023**, *10*, 1757–1768.

(280) López, C. M.; Vaughey, J. T.; Dees, D. W. Morphological Transitions on Lithium Metal Anodes. *J. Electrochem. Soc.* **2009**, *156*, A726.

(281) Li, Z.; Huang, J.; Yann Liaw, B.; Metzler, V.; Zhang, J. A review of lithium deposition

in lithium-ion and lithium metal secondary batteries. *J. Power Sources* **2014**, *254*, 168–182.

(282) Chang, H. J.; Ilott, A. J.; Trease, N. M.; Mohammadi, M.; Jerschow, A.; Grey, C. P. Correlating Microstructural Lithium Metal Growth with Electrolyte Salt Depletion in Lithium Batteries Using 7Li MRI. *J. Am. Chem. Soc.* **2015**, *137*, 15209–15216.

(283) Mayers, M. Z.; Kaminski, J. W.; Miller, T. F. I. Suppression of Dendrite Formation via Pulse Charging in Rechargeable Lithium Metal Batteries. *J. Phys. Chem. C* **2012**, *116*, 26214–26221.

(284) Zhao, Q. S.; NuLi, Y. N.; Guo, Y. S.; Yang, J.; Wang, J. L. Reversibility of electrochemical magnesium deposition from tetrahydrofuran solutions containing pyrrolidinyl magnesium halide. *Electrochim. Acta* **2011**, *56*, 6530–6535.

(285) Groß, A. *Theoretical Surface Science*, 2nd ed.; Springer Berlin, Heidelberg, 2009.

(286) Venables, J. A. Nucleation calculations in a pair-binding model. *Phys. Rev. B* **1987**, *36*, 4153–4162.

(287) Richards, W. D.; Miara, L. J.; Wang, Y.; Kim, J. C.; Ceder, G. Interface Stability in Solid-State Batteries. *Chem. Mater.* **2016**, *28*, 266–273.

(288) Chen, T.; Ceder, G.; Sai Gautam, G.; Canepa, P. Evaluation of Mg Compounds as Coating Materials in Mg Batteries. *Front. Chem.* **2019**, *7*, 24.

(289) Ganesan, P.; Soans, M.; Cambaz, M. A.; Zimmermanns, R.; Gond, R.; Fuchs, S.; Hu, Y.; Baumgart, S.; Sotoudeh, M.; Stepien, D. et al. Fluorine-Substituted Halide Solid Electrolytes with Enhanced Stability toward the Lithium Metal. *ACS Appl. Mater. Interfaces* **2023**, *15*, 38391–38402.

(290) Tian, Y.; Sun, Y.; Hannah, D. C.; Xiao, Y.; Liu, H.; Chapman, K. W.; Bo, S.-H.;

Ceder, G. Reactivity-Guided Interface Design in Na Metal Solid-State Batteries. *Joule* **2019**, *3*, 1037–1050.

(291) Lombardo, T.; Duquesnoy, M.; El-Bouysidy, H.; Årén, F.; Gallo-Bueno, A.; Jørgensen, P. B.; Bhowmik, A.; Demortière, A.; Ayerbe, E.; Alcaide, F. et al. Artificial Intelligence Applied to Battery Research: Hype or Reality? *Chemical Reviews* **2022**, *122*, 10899–10969.

(292) Xiao, Y.; Wang, Y.; Bo, S.-H.; Kim, J. C.; Miara, L. J.; Ceder, G. Understanding interface stability in solid-state batteries. *Nat. Rev. Mater.* **2020**, *5*, 105–126.

(293) Chen, X.; Hou, T.; Persson, K. A.; Zhang, Q. Combining theory and experiment in lithium–sulfur batteries: Current progress and future perspectives. *Mater. Today* **2019**, *22*, 142–158.

(294) Bayliss, R. D.; Key, B.; Sai Gautam, G.; Canepa, P.; Kwon, B. J.; Lapidus, S. H.; Dogan, F.; Adil, A. A.; Lipton, A. S.; Baker, P. J. et al. Probing Mg Migration in Spinel Oxides. *Chem. Mater.* **2020**, *32*, 663–670.

(295) Chen, T.; Sai Gautam, G.; Huang, W.; Ceder, G. First-Principles Study of the Voltage Profile and Mobility of Mg Intercalation in a Chromium Oxide Spinel. *Chem. Mater.* **2018**, *30*, 153–162.

(296) Pollice, R.; dos Passos Gomes, G.; Aldeghi, M.; Hickman, R. J.; Krenn, M.; Lavigne, C.; Lindner-D'Addario, M.; Nigam, A.; Ser, C. T.; Yao, Z. et al. Data-Driven Strategies for Accelerated Materials Design. *Acc. Chem. Res.* **2021**, *54*, 849–860.

(297) Scheffler, M.; Aeschlimann, M.; Albrecht, M.; Bereau, T.; Bungartz, H.-J.; Felser, C.; Greiner, M.; Groß, A.; Koch, C. T.; Kremer, K. et al. FAIR data enabling new horizons for materials research. *Nature* **2022**, *604*, 635–642.

(298) Sjølin, B. H.; Jørgensen, P. B.; Fedrigucci, A.; Vegge, T.; Bhowmik, A.; Castelli, I. E. Accelerated Workflow for Antiperovskite-based Solid State Electrolytes. *Batteries Supercaps* **2023**, *6*, e202300041.

(299) Schaarschmidt, J.; Yuan, J.; Strunk, T.; Kondov, I.; Huber, S. P.; Pizzi, G.; Kahle, L.; Bölle, F. T.; Castelli, I. E.; Vegge, T. et al. Workflow Engineering in Materials Design within the BATTERY 2030+ Project. *Adv. Energy Mater.* **2022**, *12*, 2102638.

(300) Bölle, F. T.; Mathiesen, N. R.; Nielsen, A. J.; Vegge, T.; Garcia-Lastra, J. M.; Castelli, I. E. Autonomous Discovery of Materials for Intercalation Electrodes. *Batteries Supercaps* **2020**, *3*, 488–498.

(301) Wang, Y.; Liu, J.; Du, P.-H.; Sun, Z.; Sun, Q. Screening Topological Quantum Cathode Materials for K-Ion Batteries by Graph Neural Network and First-Principles Calculations. *ACS Appl. Energy Mater.* **2023**, *6*, 4503–4510.

(302) Chen, C.; Zuo, Y.; Ye, W.; Li, X.; Deng, Z.; Ong, S. P. A Critical Review of Machine Learning of Energy Materials. *Advanced Energy Materials* **2020**, *10*, 1903242.

(303) Deng, L. The MNIST Database of Handwritten Digit Images for Machine Learning Research [Best of the Web]. *IEEE Signal Proc. Mag.* **2012**, *29*, 141–142.

(304) Barker, J.; Watanabe, S.; Vincent, E.; Trmal, J. The fifth 'CHiME' Speech Separation and Recognition Challenge: Dataset, task and baselines. Interspeech. 2018.

(305) Saal, J. E.; Kirklin, S.; Aykol, M.; Meredig, B.; Wolverton, C. Materials Design and Discovery with High-Throughput Density Functional Theory: The Open Quantum Materials Database (OQMD). *JOM* **2013**, *65*, 1501–1509.

(306) Kirklin, S.; Saal, J. E.; Meredig, B.; Thompson, A.; Doak, J. W.; Aykol, M.; Rühl, S.; Wolverton, C. The Open Quantum Materials Database (OQMD): assessing the accuracy of DFT formation energies. *npj Comput. Mater.* **2015**, *1*, 15010.

(307) Curtarolo, S.; Setyawan, W.; Wang, S.; Xue, J.; Yang, K.; Taylor, R. H.; Nelson, L. J.; Hart, G. L.; Sanvito, S.; Buongiorno-Nardelli, M. et al. AFLOWLIB.ORG: A distributed materials properties repository from high-throughput ab initio calculations. *Comput. Mater. Sci.* **2012**, *58*, 227–235.

(308) Ortiz, C.; Eriksson, O.; Klintenberg, M. Data mining and accelerated electronic structure theory as a tool in the search for new functional materials. *Comput. Mater. Sci.* **2009**, *44*, 1042–1049.

(309) Landis, D. D.; Hummelshøj, J. S.; Nestorov, S.; Greeley, J.; Dułak, M.; Bligaard, T.; Nørskov, J. K.; Jacobsen, K. W. The Computational Materials Repository. *Computing in Science & Engineering* **2012**, *14*, 51–57.

(310) Draxl, C.; Scheffler, M. NOMAD: The FAIR concept for big data-driven materials science. *MRS Bull.* **2018**, *43*, 676–682.

(311) Gražulis, S.; Daškevič, A.; Merkys, A.; Chateigner, D.; Lutterotti, L.; Quirós, M.; Serebryanaya, N. R.; Moeck, P.; Downs, R. T.; Le Bail, A. Crystallography Open Database (COD): an open-access collection of crystal structures and platform for world-wide collaboration. *Nucleic Acids Res.* **2011**, *40*, D420–D427.

(312) Villars, P.; Cenzual, K.; Gladyshevskii, R.; Iwata, S. *Materials Informatics*; John Wiley & Sons, Ltd, 2019; Chapter 3, pp 55–106.

(313) Meredig, B.; Agrawal, A.; Kirklin, S.; Saal, J. E.; Doak, J. W.; Thompson, A.; Zhang, K.; Choudhary, A.; Wolverton, C. Combinatorial screening for new materials in unconstrained composition space with machine learning. *Phys. Rev. B* **2014**, *89*, 094104.

(314) Jain, A.; Hautier, G.; Ong, S. P.; Dacek, S.; Ceder, G. Relating voltage and thermal safety in Li-ion battery cathodes: a high-throughput computational study. *Phys. Chem. Chem. Phys.* **2015**, *17*, 5942–5953.

(315) Nolan, A. M.; Zhu, Y.; He, X.; Bai, Q.; Mo, Y. Computation-Accelerated Design of Materials and Interfaces for All-Solid-State Lithium-Ion Batteries. *Joule* **2018**, *2*, 2016–2046.

(316) Aykol, M.; Kim, S.; Hegde, V. I.; Snydacker, D.; Lu, Z.; Hao, S.; Kirklin, S.; Morgan, D.; Wolverton, C. High-throughput computational design of cathode coatings for Li-ion batteries. *Nat. Commun.* **2016**, *7*, 13779.

(317) Xiao, Y.; Miara, L. J.; Wang, Y.; Ceder, G. Computational Screening of Cathode Coatings for Solid-State Batteries. *Joule* **2019**, *3*, 1252–1275.

(318) Deng, Z.; Zhu, Z.; Chu, I.-H.; Ong, S. P. Data-Driven First-Principles Methods for the Study and Design of Alkali Superionic Conductors. *Chemistry of Materials* **2017**, *29*, 281–288.

(319) Ganesan, P.; Zimmermanns, R.; Liang, J.; Hu, Y.; Cuello, G. J.; Puente Orench, I.; Baumgart, S.; Sotoudeh, M.; Groß, A.; Diemant, T. et al. In-Depth Analysis of the Origin of Enhanced Ionic Conductivity of Halide-Based Solid-State Electrolyte by Anion Site Substitution. *Batteries Supercaps* **2025**, *8*, e202500378.

(320) Ibarra, J.; Várez, A.; León, C.; Santamaria, J.; Torres-Martinez, L.; Sanz, J. Influence of composition on the structure and conductivity of the fast ionic conductors $La_{2/3-x}Li_{3x}TiO_3$ ($0.03 \leq x \leq 0.167$). *Solid State Ion.* **2000**, *134*, 219–228.

(321) Boulineau, S.; Courty, M.; Tarascon, J.-M.; Viallet, V. Mechanochemical synthesis of Li-argyrodite Li_6PS_5X (X=Cl, Br, I) as sulfur-based solid electrolytes for all solid state batteries application. *Solid State Ion.* **2012**, *221*, 1–5.

(322) Kumazaki, S.; Iriyama, Y.; Kim, K.-H.; Murugan, R.; Tanabe, K.; Yamamoto, K.; Hirayama, T.; Ogumi, Z. High lithium ion conductive $Li_7La_3Zr_2O_{12}$ by inclusion of both Al and Si. *Electrochem. Commun.* **2011**, *13*, 509–512.

(323) Aono, H.; Sugimoto, E.; Sadaoka, Y.; Imanaka, N.; ya Adachi, G. Ionic conductivity and sinterability of lithium titanium phosphate system. *Solid State Ion.* **1990**, *40-41*, 38–42.

(324) Kamaya, N.; Homma, K.; Yamakawa, Y.; Hirayama, M.; Kanno, R.; Yonemura, M.; Kamiyama, T.; Kato, Y.; Hama, S.; Kawamoto, K. et al. A lithium superionic conductor. *Nat. Mater.* **2011**, *10*, 682–686.

(325) Sendek, A. D.; Yang, Q.; Cubuk, E. D.; Duerloo, K.-A. N.; Cui, Y.; Reed, E. J. Holistic computational structure screening of more than 12000 candidates for solid lithium-ion conductor materials. *Energy Environ. Sci.* **2017**, *10*, 306–320.

(326) Nakayama, M.; Kanamori, K.; Nakano, K.; Jalem, R.; Takeuchi, I.; Yamasaki, H. Data-Driven Materials Exploration for Li-Ion Conductive Ceramics by Exhaustive and Informatics-Aided Computations. *Chem. Rec.* **2019**, *19*, 771–778.

(327) Jalem, R.; Nakayama, M.; Kasuga, T. An efficient rule-based screening approach for discovering fast lithium ion conductors using density functional theory and artificial neural networks. *J. Mater. Chem. A* **2014**, *2*, 720–734.

(328) Jalem, R.; Kimura, M.; Nakayama, M.; Kasuga, T. Informatics-Aided Density Functional Theory Study on the Li Ion Transport of Tavorite-Type $LiMTO_4F$ (M^{3+}–T^{5+}, M^{2+}–T^{6+}). *J. Chem. Inf. Model.* **2015**, *55*, 1158–1168.

(329) Düvel, A.; Heitjans, P.; Fedorov, P.; Scholz, G.; Cibin, G.; Chadwick, A. V.; Pickup, D. M.; Ramos, S.; Sayle, L. W. L.; Sayle, E. K. L. et al. Is Geometric Frustration-Induced Disorder a Recipe for High Ionic Conductivity? *J. Am. Chem. Soc.* **2017**, *139*, 5842–5848.

(330) Zhang, Y.; He, X.; Chen, Z.; Bai, Q.; Nolan, A. M.; Roberts, C. A.; Banerjee, D.; Matsunaga, T.; Mo, Y.; Ling, C. Unsupervised discovery of solid-state lithium ion conductors. *Nat. Commun.* **2019**, *10*, 5260.

(331) Zhang, Y.; Ling, C. A strategy to apply machine learning to small datasets in materials science. *npj Comput. Mater.* **2018**, *4*, 25.

(332) Zhu, Z.; Chu, I.-H.; Ong, S. P. Li3Y(PS4)2 and Li5PS4Cl2: New Lithium Superionic Conductors Predicted from Silver Thiophosphates using Efficiently Tiered Ab Initio Molecular Dynamics Simulations. *Chem. Mater.* **2017**, *29*, 2474–2484.

(333) Fujimura, K.; Seko, A.; Koyama, Y.; Kuwabara, A.; Kishida, I.; Shitara, K.; Fisher, C. A. J.; Moriwake, H.; Tanaka, I. Accelerated Materials Design of Lithium Superionic Conductors Based on First-Principles Calculations and Machine Learning Algorithms. *Adv. Energy Mater.* **2013**, *3*, 980–985.

(334) Zeng, S.; Zhao, Y.; Li, G.; Wang, R.; Wang, X.; Ni, J. Atom table convolutional neural networks for an accurate prediction of compounds properties. *npj Comput. Mater.* **2019**, *5*, 84.

(335) Xie, T.; Grossman, J. C. Crystal Graph Convolutional Neural Networks for an Accurate and Interpretable Prediction of Material Properties. *Phys. Rev. Lett.* **2018**, *120*, 145301.

(336) Chen, C.; Ye, W.; Zuo, Y.; Zheng, C.; Ong, S. P. Graph Networks as a Universal Machine Learning Framework for Molecules and Crystals. *Chemistry of Materials* **2019**, *31*, 3564–3572.

(337) Lee, J.; Asahi, R. Transfer learning for materials informatics using crystal graph convolutional neural network. *Comput. Mater. Sci.* **2021**, *190*, 110314.

(338) Harada, M.; Takeda, H.; Suzuki, S.; Nakano, K.; Tanibata, N.; Nakayama, M.; Karasuyama, M.; Takeuchi, I. Bayesian-optimization-guided experimental search of NASICON-type solid electrolytes for all-solid-state Li-ion batteries. *J. Mater. Chem. A* **2020**, *8*, 15103–15109.

(339) Cubuk, E. D.; Sendek, A. D.; Reed, E. J. Screening billions of candidates for solid lithium-ion conductors: A transfer learning approach for small data. *J. Chem. Phys.* **2019**, *150*, 214701.

(340) Ahmad, Z.; Xie, T.; Maheshwari, C.; Grossman, J. C.; Viswanathan, V. Machine Learning Enabled Computational Screening of Inorganic Solid Electrolytes for Suppression of Dendrite Formation in Lithium Metal Anodes. *ACS Cent. Sci.* **2018**, *4*, 996–1006.

(341) Sendek, A. D.; Cubuk, E. D.; Antoniuk, E. R.; Cheon, G.; Cui, Y.; Reed, E. J. Machine Learning-Assisted Discovery of Solid Li-Ion Conducting Materials. *Chem. Mater.* **2019**, *31*, 342–352.

(342) He, X.; Bai, Q.; Liu, Y.; Nolan, A. M.; Ling, C.; Mo, Y. Crystal Structural Framework of Lithium Super-Ionic Conductors. *Adv. Energy Mater.* **2019**, *9*, 1902078.

(343) Xiong, S.; He, X.; Han, A.; Liu, Z.; Ren, Z.; McElhenny, B.; Nolan, A. M.; Chen, S.; Mo, Y.; Chen, H. Computation-Guided Design of LiTaSiO5, a New Lithium Ionic Conductor with Sphene Structure. *Adv. Energy Mater.* **2019**, *9*, 1803821.

(344) Joshi, R. P.; Eickholt, J.; Li, L.; Fornari, M.; Barone, V.; Peralta, J. E. Machine Learning the Voltage of Electrode Materials in Metal-Ion Batteries. *ACS Appl. Mater. Interfaces* **2019**, *11*, 18494–18503.

(345) Wang, X.; Xiao, R.; Li, H.; Chen, L. Quantitative structure-property relationship study of cathode volume changes in lithium ion batteries using ab-initio and partial least squares analysis. *J. Materiom.* **2017**, *3*, 178–183, High-throughput Experimental and Modeling Research toward Advanced Batteries.

(346) Attarian Shandiz, M.; Gauvin, R. Application of machine learning methods for the prediction of crystal system of cathode materials in lithium-ion batteries. *Comput. Mater. Sci.* **2016**, *117*, 270–278.

(347) Zhang, H.; Wang, Z.; Ren, J.; Liu, J.; Li, J. Ultra-fast and accurate binding energy prediction of shuttle effect-suppressive sulfur hosts for lithium-sulfur batteries using machine learning. *Energy Storage Mater.* **2021**, *35*, 88–98.

(348) Sanchez, J.; Ducastelle, F.; Gratias, D. Generalized cluster description of multicomponent systems. *Physica A: Statistical Mechanics and its Applications* **1984**, *128*, 334–350.

(349) Natarajan, A. R.; Van der Ven, A. Machine-learning the configurational energy of multicomponent crystalline solids. *npj Computational Materials* **2018**, *4*, 56.

(350) Houchins, G.; Viswanathan, V. An accurate machine-learning calculator for optimization of Li-ion battery cathodes. *J. Chem. Phys.* **2020**, *153*, 054124.

(351) Eremin, R. A.; Zolotarev, P. N.; Ivanshina, O. Y.; Bobrikov, I. A. Li(Ni,Co,Al)O2 Cathode Delithiation: A Combination of Topological Analysis, Density Functional Theory, Neutron Diffraction, and Machine Learning Techniques. *J. Phys. Chem. C* **2017**, *121*, 28293–28305.

(352) Ouyang, R.; Curtarolo, S.; Ahmetcik, E.; Scheffler, M.; Ghiringhelli, L. M. SISSO: A compressed-sensing method for identifying the best low-dimensional descriptor in an immensity of offered candidates. *Phys. Rev. Mater.* **2018**, *2*, 083802.

(353) Fan, J.; Lv, J. Sure Independence Screening for Ultrahigh Dimensional Feature Space. *J. R. Statist. Soc. B* **2008**, *70*, 849–911.

(354) Bartel, C. J.; Sutton, C.; Goldsmith, B. R.; Ouyang, R.; Musgrave, C. B.; Ghiringhelli, L. M.; Scheffler, M. New tolerance factor to predict the stability of perovskite oxides and halides. *Sci. Adv.* **2019**, *5*, eaav0693.